Luz Stefany Murcia Correa

Study of SERS-Active substrates for low-concentration detection

Estudo de substratos SERS-ativos para detecção de baixa concentração

São José dos Campos - SP - Brazil

August 2023

Luz Stefany Murcia Correa

Study of SERS-Active substrates for low-concentration detection

Doctoral Thesis submitted to Postgraduate Program in Physics and Astronomy from Universidade do Vale do Paraíba for the degree of Doctor in Physics and Astronomy.

Universidade do Vale do Paraíba – UNIVAP
Instituto de Pesquisa e Desenvolvimento
Programa de Pós-Graduação em Física e Astronomia

Supervisor Prof. Dr. Leandro José Raniero

São José dos Campos - SP - Brazil
August 2023

FVE Fundação Valeparaibana de Ensino

BIBLIOTECA

TERMO DE AUTORIZAÇÃO DE DIVULGAÇÃO DA OBRA

Ficha catalográfica

Murcia Correa, Luz Stefany
Study of SERS-Active substrates for low-concentration detection / Luz Stefany Murcia Correa; orientador, Prof. Dr. Leandro José Raniero. - São José dos Campos, SP, 2023.
1 CD-ROM, 122 p.

Tese (Doutorado) - Universidade do Vale do Paraíba, São José dos Campos. Programa de Pós-Graduação em Física e Astronomia.

Inclui referências

1. Física e Astronomia. 2. Nanoparticulas. 3. Surface-Enhanced Raman Scattering. 4. Física do estado sólido. I. Raniero, Prof. Dr. Leandro José, orient. II. Universidade do Vale do Paraíba. Programa de Pós-Graduação em Física e Astronomia. III. Título.

Eu, Luz Stefany Murcia Correa, autor(a) da obra acima referenciada:

Autorizo a divulgação total ou parcial da obra impressa, digital ou fixada em outro tipo de mídia, bem como, a sua reprodução total ou parcial, devendo o usuário da reprodução atribuir os créditos ao autor da obra, citando a fonte.

Declaro, para todos os fins e efeitos de direito, que o Trabalho foi elaborado respeitando os princípios da moral e da ética e não violou qualquer direito de propriedade intelectual sob pena de responder civil, criminal, ética e profissionalmente por meus atos.

São José dos Campos, 25 de Agosto de 2023.

Autor(a) da Obra

Data da defesa: 31 / 08 / 2023

Universidade do Vale do Paraíba

Instituto de Pesquisa
e Desenvolvimento

LUZ STEFANY MURCIA CORREA

"STUDY OF SERS-ACTIVE SUBSTRATES FOR LOW-CONCENTRATIONS DETECTION."

Tese aprovada como requisito parcial à obtenção do grau de Doutor, do Programa de Pós-Graduação em Física e Astronomia, do Instituto de Pesquisa e Desenvolvimento da Universidade do Vale do Paraíba, São José dos Campos, SP, pela seguinte banca examinadora:

Prof. Dr. Oli Luiz Dors Junior	
Prof. Dr. Leandro José Raniero	
Prof. Dr. Irapuan Rodrigues de Oliveira Filho	
Prof. Dr. César Aurelio Herreño Fierro	César Aurelio Herreño Fierro
Prof.ª Dr.ª Ana Maria do Espírito Santo	

Prof.ª Dr.ª Lúcia Vieira

Diretora do IP&D – Univap

São José dos Campos, 31 de agosto de 2023.

STATEMENT OF AUTHORSHIP

I hereby declare that the thesis submitted is my work. All direct or indirect sources used are acknowledged as references. I further declare that I have not submitted this thesis at any other institution to obtain a degree.

To my family and friends. I am nothing without them.

Acknowledgements

Agradezco al universo, a Dios y a la vida por permitirme concluir este trabajo de manera satisfactoria. Gracias a mis padres, Gilma y Afranio, a mi hermano Eder, a mi sobrino Benji, y a mi perrito Matías, por todo su amor, apoyo, paciencia, sabiduría, y confianza. Por nunca dudar de mí, y por toda la fortaleza y valentía que me dan. Gracias por sus oraciones, protección y cuidado. Gracias por estar siempre.

Un agradecimiento especial al profesor Leandro. Gracias por su colaboración y orientación en el momento más decisivo de mi doctorado. Agradezco también a Omar por su orientación, persistencia y apoyo en este camino. Agradezco a la Coordenação de Aperfeiçoamento de Pessoal de Nível Superior (CAPES), por el apoyo financiero e institucional en el proceso número 88887.342124/2019-00. Gracias a la Universidade do Vale do Paraíba (UNIVAP), y a los profesores por la oportunidad de realizar mis estudios de doctorado en Física y Astronomía.

Agradezco a los profesores Vladimir Airoldi y Luiz Angelo Berni del Laboratorio Asociado se Sensores y Materiales (LABAS) del Instituto Nacional de Pesquisas Espaciais (INPE), por todo el apoyo y colaboración con los insumos y equipos necesarios para el desarrollo de mi investigación. Así como también a la profesora Lúcia Vieira por el apoyo en el uso del Laboratorio de Nanotecnoplasma del IP&D (UNIVAP). También agradezco a las funcionarias de la central analítica del IP&D, Priscila y Angela por el apoyo en el desarrollo experimental de mi trabajo.

Gracias a todas(os) mis compañeras(os) del Laboratorio de Nanosensores (LNS). Por el apoyo y por recibirme con los brazos abiertos en el momento que más lo necesité.

Agradezco especialmente a cada una de las personas que llegaron a mi vida durante este tiempo, así como también a aquellos que se fueron. En especial agradezco a mis amigas(os): Gissell, Irene, Elena, Luz Angela, Liliam, Daniela, Bruno, Elisa, Viviana y Twix, Fernanda, Júlia, Carlitos, Lenin, Renan, Cirlezi, Virginia, Yusen y Arian, Paulo, Maycom y Gustavo. Por escucharme siempre, por darme la mano cuando lo necesité, por decirme las palabras adecuadas en el momento adecuado, por alentarme, por su energía y apoyo para continuar con resiliencia en esta jornada. Gracias Daniel por todo tu cariño, buena energía, tus enseñanzas, por la literatura y por mostrarme lo fuerte que podía llegar a ser. Gracias Yosef por todo tu cariño, energía y apoyo en la recta final de este proceso. Sin ninguno de ustedes este resultado no habría sido posible.

Gracias al arte, a la danza y a la música, por ser una parte fundamental en mi vida, sin ellas no hubiese tenido tanto coraje para seguir. Gracias por las hermosas personas que pude conocer a través de la danza, en especial a mis grandes maestras: Roseane,

Marie y Gláucia. Gracias por darme la oportunidad de descubrir esa danza que había dentro de mí. Gracias por contagiarme con su pasión por el arte y la vida. También quiero agradecer al profesor Eduardo, por darme la oportunidad de practicar yoga en la medida de mis posibilidades. Este arte me permitió llegar a una mayor espiritualidad, autoconocimiento y a nutrir mi mente por medio de la meditación. A encontrar el conforto dentro del desconforto y a estar cada día más presente. Muchas gracias también a mi fisioterapeuta, Márcio, por ayudarme en todo mi proceso de recuperación física y por motivarme a seguir espiritual y físicamente. Agradezco al Serviço Escola de Psicologia (UNIVAP) por el cuidado y servicio que prestan. A cada uno de mis psicoterapeutas, muchas gracias por escucharme, ayudarme y dar la atención necesaria durante esta trayectoria.

Siempre tuve el deseo de estudiar en Brasil. Gracias hermoso país, por finalmente abrirme tus puertas y permitirme crecer cultural, física, mental y académicamente. Tu encanto, al igual que el de Colombia, está en la diversidad que representas. En otro lugar, ésta experiencia no habría sido lo suficientemente enriquecedora.

Éste trabajo es dedicado a todos ustedes, porque todos dejaron una gran huella en mí. Gracias por estar presentes en mi vida. Por ustedes pude construirme, crecer y evolucionar durante esta jornada llamada doctorado.

Y por último, quiero dar gracias a mí misma, por no permitirme desistir, por caer y tener la fuerza suficiente para volver a levantarme. Por escucharme, por seguir mi intuición y mi corazón en cada decisión, y por mi valentía y resiliciencia. Por cuidarme física, mental y espiritualmente, disfrutando de mi proceso cada día. Gracias a esta jornada pude descubrir y amar lo que realmente soy!

“Nothing in life is to be feared. It is only to be understood. Now is the time to understand more so that we may fear less”.

Marie Curie

Abstract

Surface-enhanced Raman scattering (SERS) is a highly efficient technique due to its ability to detect several analytes at low concentrations, such as proteins, pesticides, heavy metals, environmental monitoring, food safety, biochemical sensing, and others. One of the most critical applications of SERS detection is herbicides. Glyphosate (GLP) is the herbicide with the highest global commercialization, and historical use (NOVOTNY, 2022; MARTINS-GOMES et al., 2022). Even though numerous studies have found the substance harmless, current research demonstrates that GLP might affect human health (RIVAS-GARCIA et al., 2022). For this reason, researchers are concentrating on alternatives for analytical quantification, such as SERS.

In this work, DVD-R@AgNPs and PSi@AgNPs SERS-actives substrates were produced by the Cathodic Cage Plasma Deposition (CCPD) technique, which allowed a thin film layer deposition of silver nanoparticles (AgNPs) on the polycarbonate (PC) grating structure from Digital Video/Versatile Disc Recordable (DVD-R) and on the porous silicon (PSi) structure. Scanning Electron Microscopy with energy-dispersive X-ray spectroscopy was used to characterize the substrates and chemical changes on the surfaces after AgNPs deposition. DVD-R@AgNPs and PSi@AgNPs substrates were used to detect standard crystal violet (CV), standard GLP, and Roundup$^{\text{TM}}$ GLP (GLP-RU) using Raman Spectroscopy measurements. The CV was used as a control dye molecule to calculate the enhancement factors, which value was in the order of $\sim 10^5$ for both substrates. To evaluate the efficiency of the SERS substrates, the analytes limit of detection was calculated. For DVD-R@AgNPs, the lowest concentration detected was $\sim 10^{-10}$ M for CV, 10^{-7} and 10^{-8} M for GLP and 10^{-6} M for GLP-RU. While for PSi@AgNPs, $\sim 10^{-12}$ M for CV and 10^{-2} M for GLP-RU were the lowest concentrations obtained. Despite this value, PSi@AgNPs is a good SERS platform for AgNPs deposition, via CCPD, and it needs to enhance the sensitivity for herbicide traces detection as GLP-RU. Accordingly, the DVD-R@AgNPs SERS sensor is a low-cost and promising substrate that analyzes traces of commercial GLP, demonstrating high SERS sensitivities.

Keywords: SERS, silver nanoparticles, Cathodic cage plasma deposition (CCPD), optical discs, porous silicon, Glyphosate, nanoplasmonics.

Resumo

O espalhamento Raman aprimorado por superfície (SERS) é uma técnica altamente eficiente devido à sua capacidade de detectar diversos analitos em baixas concentrações, como proteínas, pesticidas, íons de metais pesados, monitoramento ambiental, segurança alimentar, sensoriamento bioquímico, entre outros. Uma das aplicações mais críticas de detecção via SERS são os herbicidas. O glifosato (GLP) é o herbicida com maior comercialização global e uso histórico (NOVOTNY, 2022; MARTINS-GOMES et al., 2022). Embora numerosos estudos tenham considerado a substância inofensiva, pesquisas atuais demonstram que o GLP pode afetar a saúde humana (RIVAS-GARCIA et al., 2022), por isso, os pesquisadores estão se concentrando em alternativas de quantificação analítica, como o SERS.

Neste trabalho, substratos SERS-ativos de DVD-R@AgNPs e PSi@AgNPs foram produzidos pela técnica de Deposição de Plasma em Gaiola Catódica (CCPD), que permitiu a deposição de uma fina camada de nanopartículas de prata (AgNPs) na estrutura de grade do policarbonato (PC) de Video Digital/disco versátil gravável (DVD-R) e na estrutura de silício poroso (PSi). A Microscopia Eletrônica de Varredura com espectroscopia de energia dispersiva de raios X foi utilizada para caracterizar os substratos e as mudanças químicas nas superfícies após a deposição de AgNPs. Os substratos DVD-R@AgNPs e PSi@AgNPs foram usados para detectar cristal violeta padrão (CV), GLP padrão e Roundup^{TM} GLP (GLP-RU) por meio da espectroscopia Raman. O CV foi usado como uma molécula de controle para calcular os fatores de melhora dos substratos, que foram da ordem de $\sim 10^5$. Para avaliar a eficiência dos substratos SERS, o limite de detecção dos analitos foi calculado. O substrato DVD-R@AgNPs apresenta valores de $\sim 10^{-10}$ M para CV, 10^{-7} e 10^{-8} M para GLP e 10^{-6} M para GLP-RU. Enquanto o substrato PSi@AgNPs apresenta valores de $\sim 10^{-12}$ M para CV e 10^{-2} M para GLP-RU. Apesar desse valor, PSi@AgNPs é uma boa plataforma SERS para deposição de AgNPs, via CCPD, e precisa melhorar a sensibilidade para detecção de traços de herbicidas como GLP-RU. Assim, o sensor DVD-R@AgNPs SERS é um substrato promissor e de baixo custo que analisa traços de GLP comercial, demonstrando altas sensibilidades SERS.

Palavras-chaves: SERS, nanoparticulas de prata, Deposição de Plasma em Gaiola Catódica (CCPD), discos ópticos, silicio poroso, glifosato, nanoplasmones.

List of Figures

List of Tables

Contents

1 Introduction

Raman scattering is an inelastic scattering effect that originates from an energy shift in laser photons after light-molecule interactions (KERESZTURY, 2006; PROCHÁZKA, 2016; HAN et al., 2022). Raman spectroscopy, a vibrational optical technique, facilitates the identification of molecular structural details. However, Raman scattering is a very weak process and, requires significant quantities of analytes or the application of a high-powered laser to extract molecular signatures. A decisive enhancement in Raman signal intensity can be achieved via surface-enhanced Raman scattering (SERS). This technique effectively overcomes the challenge of intrinsic low Raman signal intensity at low analyte molecule concentrations (SIEBERT; HILDEBRANDT, 2008; BHARATI; SOMA, 2021).

SERS is a highly efficient technique for ultrasensitive detection at the level of single molecules or analyte traces by amplifying the electromagnetic field (EM) in the presence of nanoscale features at the surface. SERS has many applications, including biological sensing, trace analysis, medical diagnostics, forensics, pesticide detection, explosives, and medicines (CRAIG; FRANCA; IRUDAYARAJ, 2013; SINHA et al., 2016; KUMAR; GOEL; SINGH, 2017; FIERRO-MERCADO; HERNÁNDEZ-RIVERA, 2012; HAKONEN et al., 2015; XU et al., 2018).

In fabricating a SERS substrate, the surface plasmons play an essential role (HAN et al., 2022; DING et al., 2016; ITOH et al., 2011; MOSKOVITS, 1978), because SERS intensity can increase by coupling localized surface plasmon resonance of adjacent nanoparticles (NPs) (MCNAY et al., 2011; RU; ETCHEGOIN, 2013). The efficiency of SERS substrates is affected by the location of the analytes, with the enhancement occurring when the analyte's molecule is situated in the "hot spot" regions, where electromagnetic fields are confined. Those hot spots can be found in metal nanostructures (BHARATI et al., 2019; STAROWICZ et al., 2018), and patterns/gratings on solid substrates with NPs presence (WANG et al., 2021; LI et al., 2020). Among the SERS substrates types, CD and DVD nanopatterning may offer a good opportunity due to low production costs, and metallic nanoparticles can be incorporated into substrates for better signal amplification (CIALLA et al., 2012).

One of the first explorations of SERS substrates directly derived from DVDs was reported by Gellini et al. (GELLINI et al., 2008). DVD is a master for nanopatterning of surfaces with a significant Raman enhancement. The most recent research includes Dong et al. (DONG et al., 2021) study, in which AuNPs were prepared by chemical reduction film in the inner Ag grating of DVD for Rhodamine 6G detection. This hybrid

SERS substrate reports a 10^5 enhancement factor (EF) value. The same technique was applied by Nguyen et al. (NGUYEN; NGO et al., 2020), who found that the layer of AuNPs on the DVD template exhibits an average SERS EF of $\sim 10^6$. Avella et al. (AVELLA-OLIVER et al., 2018) use a DVD-R coated with a thin silver film to analyze complex biomolecular targets. Moreover, other methods duplicate the periodic pattern of the DVD on polydimethylsiloxane (PDMS) as SERS substrates with AgNPs deposition (KUMAR et al., 2020; WANG et al., 2021).

On the other hand, achieving precise control of noble metals at the nanoscale is essential for generating significant and stable SERS signals. One efficient approach to achieve this, is by increasing the number of metal nanoparticle nucleation sites (ALWAN; YOUSIF; WALI, 2017; JABBAR; ALWAN; HAIDER, 2018). This can be accomplished by utilizing porous silicon (PSi) as a template for AgNPs in the preparation of PSi@AgNPs SERS active substrates since it enables a controlled PSi morphology and leads to an enhanced density of hot spots (ADAWYIA; ALWAN; ALLAA, 2016). PSi was accidentally discovered by Uhlir et al. at Bell Labs during the electropolishing process of Si and Ge (UHLIR, 1956). Typically, the PSi is prepared by an easy and convenient electrochemical or anodic etching of crystalline Si using an aqueous HF-based electrolyte (UNAGAMI, 1980). This allows significant control over the pore sizes and morphologies, surface modulation, and reactivity (HARRAZ, 2011; HARRAZ, 2013; HARRAZ et al., 2014).

The tailored substrate based on PSi demonstrates remarkable potential for boosting SERS sensitivity and analytical performance, as supported by previous studies (KOSOVIĆ et al., 2015; KHINEVICH et al., 2021; ŠKRABIĆ et al., 2019; GE et al., 2022; MORAM; BYRAM; SOMA, 2023). The most recent research includes Nguyen et al. (NGUYEN et al., 2022) study, in which silver nanoparticles/porous silicon (AgNPs/PSi) hybrid structures were used as SERS substrates to detect Diphenylamine (DPA) with an ultralow concentration of 10^{-9} M. Gold nanoparticles/porous silicon (AuNPs/PSi) was used to detect the antibiotic penicillin G (PG) by Wali et al. (WALI; HASAN; ALWAN, 2019). They obtained at an ultra-low PG concentration of 10^{-9} M, and an EF of 10^7. Due to the versatility of porous silicon substrates, it also has been utilized in the sensing of two important explosive molecules [ammonium nitrate (AN), picric acid (PA)], and a pesticide molecule (thiram) by Vendamani et al. (VENDAMANI et al., 2021). They estimated the substrate sensitivity of 10^4 for explosives and pesticides and evaluated the LOD at 2 μM, 1 μM, and 1 μM, respectively for AN, PA, and thiram. Another important research was reported by Al-Syadi et al. (AL-SYADI et al., 2021) with PSi-plated palladium nanoparticles SERS substrates to detect trace concentrations of imidacloprid pesticide. The active substrate detected a low concentration of 10^{-9} M imidacloprid and an EF of 10^5.

Due to the ability to identify molecules' structural information (KERESZTURY, 2006; PROCHÁZKA, 2016; HAN et al., 2022), SERS represents a singular opportunity to analyze the contamination trace in the food supply chain of the glyphosate molecule (N-(phosphonomethyl)glycine, GLP). Even though numerous studies have found the substance harmless, the International Agency for Research on Cancer (IARC) classified GLP as a “probably carcinogenic substance for humans” (TORRETTA et al., 2018). Indeed, current research demonstrates that GLP impacts hormone production and fertility. Also, GLP accelerates the growth of breast cancer cells in women by preventing the synthesis of amino acids and functioning as an endocrine disruptor (MUÑOZ; BLEAK; CALAF, 2021; INGARAMO et al., 2020; THONGPRAKAISANG et al., 2013; BRUGGEN et al., 2018).

Therefore, agriculture-related products that might contaminate the soil, underground waters, and atmosphere are a primary global concern. As a result, several countries have outlawed various pesticides, though not all adhere to the same rules. In this sense, monitoring lingering contaminants in food products is crucial to promote public policies that can raise living standards.

GLP Raman and SERS spectra have been the topic of numerous experimental and theoretical studies (SHARMA; CARMICHAEL; MCCALL, 2016; XU et al., 2020; XU et al., 2018; COSTA et al., 2012; MIKAC et al., 2022; XU et al., 2017; LÓPEZ-CASTAÑOS et al., 2020; DO et al., 2020; FEIS et al., 2020; HOLANDA et al., 2020), but their interpretation remains ambiguous, and SERS experiment sensitivity is low. In most studies, AgNPs colloidal dispersion or liquid-state detection was used as the SERS method to obtain the vibrational modes of GLP molecules. However, few studies use nanostructured surfaces or solid substrate analysis (solid SERS) to detect low concentrations of GLP. It is also important to highlight that absorption and vibration assignments could be more precise in the literature.

In this thesis, GLPs were detected at a low concentration by DVD-R@AgNPs and PSi@AgNPs, both as SERS-active substrates. These substrates were based on the grating of a commercial DVD-R and porous silicon, coated by a thin-film layer of silver nanoparticles deposited by Cathodic Cage Plasma Deposition (CCPD). This technique uses the hollow cathode effect (SANKARAN; GIAPIS, 2002), which occurs in the holes of the metallic cage, to increase the efficiency of the treatment, thereby eliminating possible defects such as nitriding (SOUSA et al., 2007; SOUSA et al., 2008). As a result, it is possible to obtain different layers on any substrate (metallics or insulators) based on the cage’s material and the gaseous mixture used. This technique produces highly uniform films and permits good roughness and crystallinity control. The fabrication method of DVD-R@AgNPs and PSi@AgNPs allows a uniform and non-chemically modified thin-film deposition, with AgNPs at a high percentage and nanometric size. The suitable NPs size and the grooves on the surface prompted the increase of SERS hot spots. Our experimental results show DVD-R@AgNPs and PSi@AgNPs as promising candidates for a new approach to SERS research for agriculture and pesticide applications.

1.1 Objectives

General

Manufacture sensitive sensors using DVD-R optical disk and porous silicon coated with silver thin film for surface-enhanced Raman spectroscopy (SERS) to detect environmental pollutants, such as herbicides.

Specifics

1. Analyze the periodical surface structures of DVD-R polymer and porous silicon materials as solid SERS-active substrates application.
2. Deposition of the silver thin film through the Cathodic Cage Plasmonic Deposition technique (CCPD).
3. Characterize the structure and morphology of thin films on substrates using the SEM-FEG technique.
4. Determine the detection limit of samples, such as Crystal Violet, standard and commercial Glyphosate, using the solid SERS-active substrate.
5. Estimate the enhancement factor of the solid SERS-active substrates and compare it with the literature.
6. Obtain the relationship between Raman intensity for low-concentrations detections.

2 Literature Review

Over the past few years, solid and liquid material-based surface-enhanced Raman scattering (SERS) detection has emerged as an exciting field in which theoretical and experimental studies of the structure and function of materials have become a focus. The importance of materials' surfaces has begun to be recognized, especially in the fundamental development of SERS sensing detection for several applications. Herein we review the background of the Raman spectroscopy and SERS concept, including its basic theory and sensing mechanism, approaches, and challenges to fabricating solid SERS-active substrates and the standard manufacturing methods. Finally, we focus on SERS sensing applications for herbicides, such as Glyphosate (GLP), extending from its chemical properties and human and environmental effects to the development and performance of low-concentration detection.

2.1 Raman Spectroscopy

Raman spectroscopy (RS) is an optical spectroscopic technique that relies on the inelastic scattering of light by matter (also known as Raman scattering—RS). The polarizability of a molecule that interacts with incident light might change due to a molecular vibration, which causes an RS event. As a result, Raman spectroscopy is a vibrational method, and Raman spectra offer unique information on chemical fingerprints. In 1928, Chandrasekhara Venkata Raman and Kariamanikkam Srinivasa Krishnan discovered the RS effect (RAMAN; KRISHNAN, 1928b; RAMAN; KRISHNAN, 1928a; KRISHNAN; SHANKAR, 1981). For "his work on the dispersion of light and the discovery of the effect called after him," C.V. Raman won the physics Nobel prize in 1930 (SINGH, 2018). Nevertheless, it was in the 1980s that instrumental advancements increased Raman techniques significantly. Some of them were advances in optoelectronics, mainly the development of detectors, compact lasers, efficient optical filters, etc. As a result, despite the inherent weakness of the RS technique, Raman spectroscopy is currently a common practice in many disciplines.

2.1.1 Basic Theory of Raman Spectroscopy

Light may be absorbed, scattered, or not affect the molecule when interacting with an electromagnetic (EM) field. Optical processes discuss here are the simultaneous (instantaneous) absorption of an incident photon and emission of another photon. The emitted photon is known as the *scattered photon*, and such processes are called *scattering processes*. The scattered photon can have an equal or a different wavelength from the incident wave, as shown in figure 1(a). When the wavelength of the elastically scattered photon is equal to the wavelength of the incident photon (λ_{laser}), it is called *Rayleigh scattering*. The *Stokes* and *Anti-Stokes* Raman inelastically scattering is present when λ_{laser} is smaller than the wavelength of the scattered photon and when λ_{laser} is higher than $\lambda_{scatter}$, respectively.

Figure 1 – Basic principle of Raman spectroscopy: (a) Interactions light-molecule. (b) Simplified Jablonski diagram illustrating the Rayleigh, Stokes, and Anti-Stokes Raman scattering processes. (c) Raman shifts explanation and (d) the corresponding Raman spectrum of CCl_4.

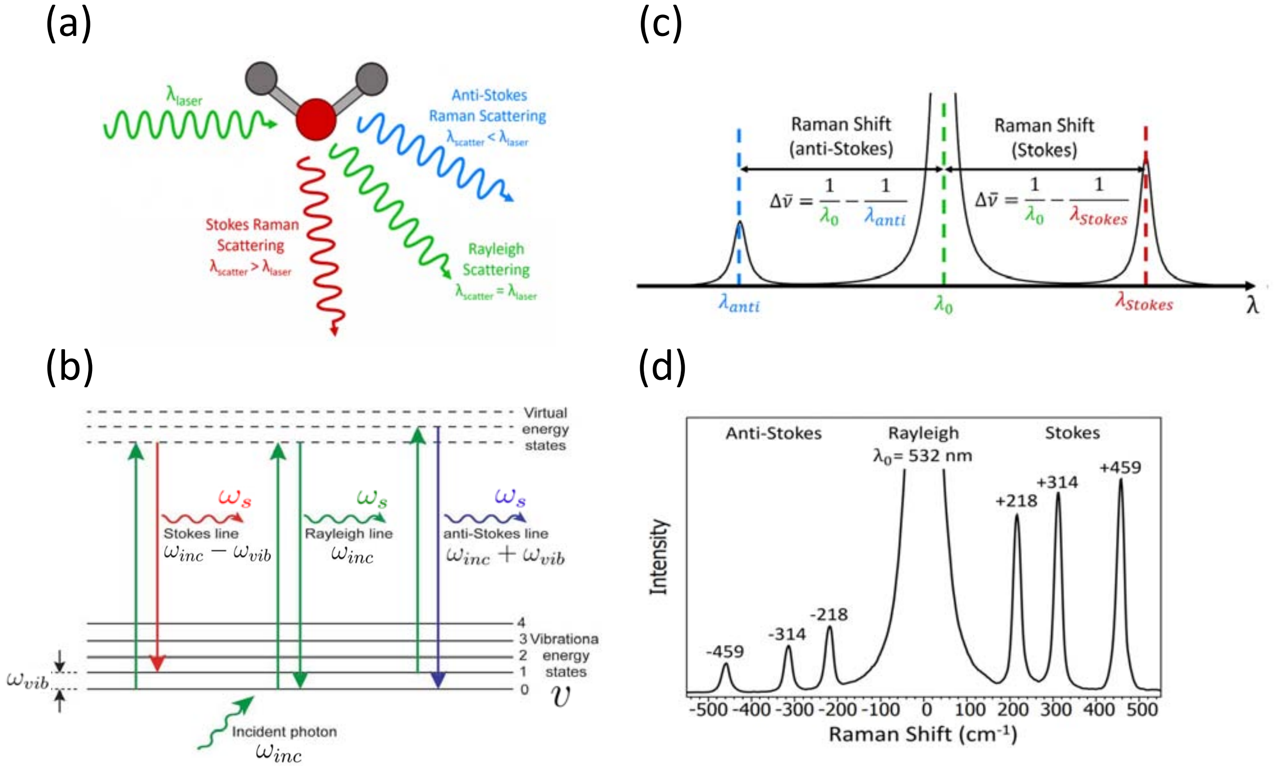

Source: Adapted from (DEY, 2022; PROCHÁZKA, 2016).

Two photons are involved in an emission process: one is absorbed, and the other is emitted after some time equal to the lifetime of the excited state. This process is consistent with the molecule's return to the ground state following its radiative excitation energy (fluorescence) decay. Fluorescence and the Raman scattering process involve an incident photon being "replaced" by a scattered (or fluorescence) photon. The immediate nature of scattering processes, as opposed to the intermediary phase required for fluorescence, is a significant distinction (electronic excitation followed by emission with a finite lifetime). Raman scattering can occur without electronic changes in the molecule at the incoming wavelength and without direct photon absorption, which is necessary for fluorescence. So it is possible to use incident light in the transparency area, which is devoid of fluorescence due to the absence of molecule absorption. In contrast to other optical processes like absorption or fluorescence, scattering processes, under typical conditions, are essentially weak phenomena. (RU; ETCHEGOIN, 2008; PROCHÁZKA, 2016; FASOLATO, 2018; SMITH; DENT, 2019; FERRARO, 2003)

An alternate perspective about quantum mechanics scattering processes is divided into two steps and viewed as the result of the incident photon's absorption and the scattered photon's spontaneous emission (as Rayleigh and Raman scattering in figure 1(b)). First, the molecule should theoretically be stimulated to a higher energy level for absorption. This energy level is portrayed as an intermediary *virtual state* because it might not exist. The virtual state should be viewed in part as a "mathematical construction of perturbation theory" because, as its name implies, it typically has no physical reality (RU; ETCHEGOIN, 2008).

The energy level representations of the Rayleigh and Raman scattering processes are shown in the Jablonski diagram from figure 1(b). In this diagram, ω_{inc} and ω_s are the incident frequencies and scattered photons, respectively. Suppose E_1 is the energy of a ground vibrational level ($v = 0$), and E_2 is that of an excited vibrational level 1 ($v = 1$) of the molecular electronic ground state. Thus, the scattered photon satisfies the following equation:

$$\hbar\omega_s = \hbar\omega_{inc} \pm (E_2 - E_1). \tag{2.1}$$

When the energy of the molecular system is the same before and after the scattering process ($\hbar\omega_s = \hbar\omega_{inc}$)[1], Rayleigh scattering results. According to classical theory, inelastic light scattering can be attributed to the modulation of the incident radiation $E_{loc}(\omega_{inc})$ by a vibrating molecule with frequency ω_{vib}. The Raman frequency can differ from the incoming photon by increments of $\omega_{inc} - \omega_{vib}$ or $\omega_{inc} + \omega_{vib}$. The scattered light is referred to as *Stokes shift* and *Anti-Stokes shift* (see figure 1(c)) when the incident radiation is shifted to a lower frequency (lower energy) and a higher frequency (higher energy), respectively. Both scatterings involve energy transfer to the molecule's vibrational mode, resulting in a higher and lower vibrational energy state (PROCHÁZKA, 2016).

Two Raman lines, spaced symmetrically from the Rayleigh line, are visible in the Raman spectrum. As an illustration, figure 1(d) shows the typical RS spectrum of carbon tetrachloride (CCl_4). Most molecules at ambient temperature are in the ground vibrational state ($v = 0$), while the population of molecules in the first vibrationally excited state ($v = 1$) is substantially less. Therefore, the Stokes lines in the spectrum are more substantial than the anti-Stokes lines because there is a much higher probability (as indicated by the Boltzmann distribution). Mainly the Stokes portion of the spectrum

---

[1] Depending on the type of spectroscopy or users, the symbol for frequency is ω or ν. ω [rad s^{-1}] is an angular frequency, ν [Hz or s^{-1}] is frequency $\nu = \omega/2\pi$. Energy can be then expressed as $E = \hbar\omega$=hν, where h is the Planck constant and $\hbar$ is the reduced Planck constant ($\hbar$=h/2π).

utilizes in Raman spectroscopy. In vibrational spectroscopy, frequencies are measured in wavenumbers, which are reciprocal to wavelength[2] and represent the number of waves in a unit of length. The Raman shift, measured in wavenumbers and written as $\Delta\nu_R$ [cm^{-1}], is the energy that photons lose during scattering events. It corresponds to the vibrational mode's wavenumber, engaged in the scattering event. Unlike luminescence, Raman shifts are not affected by the excitation wavelength. Raman peaks' locations are unique characteristics of the electronic ground state (PROCHÁZKA, 2016).

So far, the most critical optical processes have mainly been described qualitatively. Now, we'll concentrate on how can precisely measure these effects, including how many incident photons are absorbed and how many are scattered (through Rayleigh or Raman processes) for a specific molecule.

Let us consider a monochromatic laser beam that incident a single molecule. The beam's power P_{inc} [W], which it perceives by the experimenter, is proportional to the number of incident photons per unit of time. Typically, this beam concentrates on a region where the molecule is present. From the molecule's perspective, only matters the number of photons that can interact with it in a specific way, such as creating absorption. This quantity is proportional to the power density S_{inc} [W·m^2] at the molecule's position (RU; ETCHEGOIN, 2008).

If the "spot size" (beam diameter at focus) and beam profile are known, the power density can typically be related to the incident power P_{inc}. For instance, the power density at the center of a Gaussian beam (a typical approximation for focused laser beams) with a waist w_0 [m] is (RU et al., 2007):

$$S_{inc} = \frac{2P_{inc}}{\pi w_0^2}. \tag{2.2}$$

The incident beam can approximate a plane wave in many theoretical treatments. Since the wave has an unlimited size, P_{inc} cannot be specified. However, the power density can be related to the amplitude of the electric field E_{inc} [V·m^{-1}] as

$$S_{inc} = \frac{\epsilon_0 c}{2} n_M |E_{inc}|^2, \tag{2.3}$$

where $n_M = \sqrt{\epsilon_M}$ [a.d.] is the medium's refraction index in which the incident wave propagates (n_M=1 for air) (RU; ETCHEGOIN, 2008). For a given linear optical process, the cross-section of a molecule characterizes by the incident power intensity or power P of the signal during the process and by the incident power density S_{inc} at the molecule position as follows:

---

[2] The relation between wavenumbers ν' and angular frequency ω is $\nu' = \omega/2\pi c$, where c is the speed of light.

$$P = \sigma S_{inc}, \tag{2.4}$$

where σ typically depends on the excitation wavelength. Similarly, the cross-section σ_{sca} also relates the incident power density to the power dispersed by the molecule P_{sca} in optical scattering. This scenario, however, needs to correctly depict the scattering process, particularly the radiation profile, which indicates how many photons are dispersed in a specific direction (instead of integrating the signal's overall emission directions). Knowing how many photons scatter in a specified direction is, in fact, far closer to real-world experimental circumstances in which a detector is situated along a given path (RU; ETCHEGOIN, 2008).

Figure 2 – (a) Schematic illustrating of the scattered differential power. (b) Diagram of the collection optics in a typical Raman scattering experiment. Normally, the laser is focused on a narrow spot (usually ~1-10 μm in diameter, depending on the focusing optics).

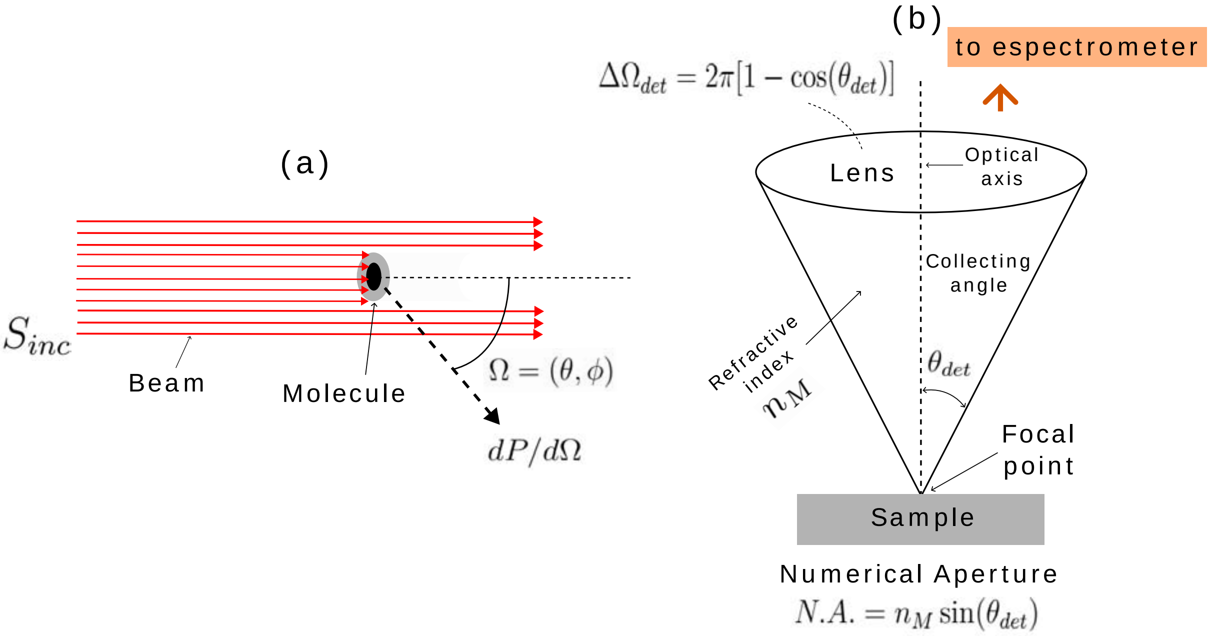

Source: Adapted from (RU; ETCHEGOIN, 2008).

The angular dependence of the scattered power characterizes the radiation profile. Two angles are required to indicate a direction in 3D. They are taken for the direction of the incident beam and joined into a single variable $\Omega \equiv (\theta, \phi)$ (see figure 2(a)). The *scattered differential power*, which is a function of Ω, may therefore be used to explicitly describe the angular dependency of the scattered power as $dP_{sca}/d\Omega$ [W·sr^{-1}]. So, using the above definition as an example, one can define a *differential scattering cross-section*, also a function of Ω, as follows:

$$\frac{dP_{sca}}{d\Omega}(\Omega) = \frac{d\sigma_{sca}}{d\Omega}(\Omega) S_{inc}, \tag{2.5}$$

where $d\sigma_{sca}/d\Omega$ describes the radiation profile of the scattering process, which value for a particular Ω_d characterizes the scattering effectiveness in that specific direction. This description is typically assessed experimentally in most Raman (or scattering) tests. Finally, we have a relationship between the two types of cross-sections in the form of:

$$\sigma_{sca} = \int \frac{d\sigma_{sca}}{d\Omega}(\Omega) d\Omega. \tag{2.6}$$

In order to fully describe the Raman active vibrational modes (Raman spectrum) of a given molecule, the most relevant aspects that must be specified are a cross-section for each vibrational mode, the orientation of the molecule for the incident field polarization, the direction of observation concerning the incident excitation, the energy (or wavelength) of the excitation, and the refractive index of the environment (for example of the solvent for dissolved molecules in liquids). Thus, combining all these factors, *absolute differential Raman cross-section* for a specific vibrational mode of energy $\hbar\omega_{vib}$ of a specific molecule can be defined as follows: Consider an incident field with an angular frequency ω_{inc}, a power of S_{inc}, and a linear polarization (always perpendicular to the incident beam). Then, the differential Stokes Raman scattered power (at frequency $\omega_s = \omega_{inc} - \omega_{vib}$), seen in a direction perpendicular to both the incident beam and the incident polarization (the so-called 90°-scattering configuration), is denoted by $dP_s/d\Omega(90)^\circ$. Thus, the *absolute differential Raman cross-section* $d\sigma_s/d\Omega$ [$\text{m}^2 \cdot \text{sr}^{-1}$] is derived from:

$$\boxed{\frac{dP_s}{d\Omega}(90^\circ) = \frac{d\sigma_s}{d\Omega} S_{inc},} \tag{2.7}$$

where $d\sigma_s/d\Omega$ is frequently called a differential Raman cross-section[3]. According to equation 2.7, $d\sigma_s/d\Omega$ is determined by: the excitation wavelength (or angular frequency ω_{inc}), the medium (environment) in which the molecule is dissolved, and a specific vibrational mode for a specific molecule (and thus its energy $\hbar\omega_{vib}$ or the Stokes angular frequency $\omega_s = \omega_{inc} - \omega_{vib}$).

On the other hand, it is possible to extract more information and characterize the magnitude of Raman scattering for a particular Raman mode using polarized detection. Following the 90°-scattering configuration, for instance, one can divide the scattered differential power into the sum of two contributions, each linked to one of the two possible

---

[3] Two essential considerations about this definition are: obtaining the same result for forward-scattering (detection along the direction of the incident beam) or back-scattering (detection in the direction from where the incident beam originated) is possible. Other detection directions are no longer the case, and the radiation profile must be considered (LONG; LONG, 2002). Second and by definition, absolute differential Raman cross-section pertains to Stokes scattering. Nevertheless, the anti-Stokes absolute differential Raman cross-section can be defined similarly.

polarizations of the scattered radiation's electric field[4]: $dP_s^{\parallel}/d\Omega$ for the field component polarized *parallel* to the incident polarization and $dP_s^{\perp}/d\Omega$ for the field component polarized *perpendicular* to it. They can characterize as differential Raman cross-sections for parallel configurations, $d\sigma_s^{\parallel}/d\Omega$; or perpendicular configurations, $d\sigma_s^{\perp}/d\Omega$, and can be defined in equation 2.7 (for unpolarized detection). The following definition applies to the *Raman depolarization ratio*, or ρ_R [a.d] of Raman mode:

$$\rho_R = \frac{dP_s^{\perp}/d\Omega(90^\circ)}{dP_s^{\parallel}/d\Omega(90^\circ)} = \frac{d\sigma_s^{\perp}/d\Omega}{d\sigma_s^{\parallel}/d\Omega}. \tag{2.8}$$

ρ_R characterizes the radiation profile for an orientation-averaged molecule and contains information about the symmetry of the vibrational mode. A thorough characterization of the experimental circumstances is necessary to measure the absolute differential Raman cross-section accurately (SCHRÖTTER; KLÖCKNER, 1979). Using the relative concentrations and peak intensities of the reference and the sample under the same experimental conditions, the absolute differential Raman cross-section of a sample calculate as follows:

$$\left(\frac{d\sigma_s}{d\Omega}\right)_{Sample} = \left(\frac{d\sigma_s}{d\Omega}\right)_{Ref} \frac{I_{Sample}}{I_{Ref}} \frac{c_{Ref}}{c_{Sample}}, \tag{2.9}$$

I is the measured integrated intensities of the Raman peak under examination, and c is the concentration (unpolarized detection is assumed) (SCHRÖTTER; KLÖCKNER, 1979). For SERS applications, if enhancement factors are measured and quantified, the measurement of the absolute differential Raman cross-section is crucial (i.e., the scaling factor between SERS and Raman cross-sections) (RU; ETCHEGOIN, 2008; RU et al., 2007).

Let us now concentrate on optical processes, beginning with the simplest case of elastic (Rayleigh) scattering, when scattering occurs at the same frequency as the incident light. By analogy with the static situation, the response to the incident radiation can therefore be characterized using the linear response function theory, as briefly sketched below: The radiation emitted by an oscillating electric dipole can use to illustrate electromagnetic radiation processes involving molecules. For example, if the incident field $\tilde{\mathbf{E}}$ (at ω_{inc}) induces an oscillating dipole at the same frequency, the oscillating dipole radiates (at ω_{inc}). The following expression resumes this classical description of Rayleigh-scattered radiation:

$$\boxed{\tilde{\mathbf{P}}_{inc}(\omega) = \hat{\alpha}_{inc}(\omega) \cdot \tilde{\mathbf{E}}(\omega).} \tag{2.10}$$

---

[4] The linear combination of two orthogonal linear polarizations can represent the electric field polarization of a radiation field since it is always perpendicular to the scattering direction.

Where $\tilde{\mathbf{P}}_{inc}(\omega)$ is the complex notation of induce dipole, oscillating at the *same frequency* ω as the applied field $\tilde{\mathbf{E}}(\omega)$ (also in complex notation). The linear optical polarizability tensor $\hat{\alpha}_{inc}(\omega)$, or the Rayleigh polarizability tensor[5], describes the molecule's linear optical response to an applied electric field (RU; ETCHEGOIN, 2008). Equation 2.10 is valid so long as the electric field applied is a small perturbation from the standard electric fields experienced by electrons and atoms in molecules; when this does not happen, additional non-linear effects give rise (RU; ETCHEGOIN, 2008).

Phenomenologically it is possible to generalize the previous argument (equation 2.10) to the situation of inelastic scattering, particularly Raman scattering. In analogy with Rayleigh scattering, the Raman polarizability tensor $\hat{\alpha}_s(\omega_{inc}, \omega_{vib})$ can be defined for a particular vibrational mode. However, this is a proportionality factor (tensor) that does not depend on time. Due to the change in oscillation frequency, $\hat{\alpha}_s(\omega_{inc}, \omega_{vib})$ cannot be considered directly as a linear response function, as was the case of $\hat{\alpha}_{inc}(\omega_{inc})$. Therefore $\hat{\alpha}_s(\omega_{inc}, \omega_{vib})$ is entirely phenomenological and not essential for a basic understanding of the Raman effect (and SERS). While for Rayleigh scattering, $\hat{\alpha}_s(\omega_{inc}, \omega_{vib})$ is specified for a given mode of vibration and excitation frequency ω_{inc}. Then the Raman scattering process can be described classically and entirely as the induction of a Raman dipole whose radiation produces Raman scattering scattered light. Finally, this description is the starting point for most generalizations of the effect on more complex situations, including SERS (RU; ETCHEGOIN, 2008).

We can make one more observation about the distinction between Rayleigh and Raman scattering from the perspective of "classical electromagnetic theory," which has to do with the coherence of the scattering process from an ensemble of molecules. However, it is only conceptually significant because it has little practical impact on Raman or SERS. Since the induced dipole is driven by a constant phase relation concerning the incoming wave, Rayleigh scattering is an inherently coherent process that results in scattered electromagnetic radiation. The polarizability, typically a complex magnitude, can cause a phase difference between the two. However, if we look at a scattering volume much smaller than the wavelength, this phase difference is the same for all molecules. Therefore under the right experimental circumstances, coherent effects may manifest in Rayleigh scattering. Nevertheless, Raman scattering presents a unique set of challenges. First, since it is an inelastic process, the vibration must be present, whose phase is typically different for two separate molecules. So, even if the excitation is in phase for two molecules, the scattered radiation has an arbitrary phase for the incoming wave. So, at the microscopic level, Raman scattering from an ensemble of molecules is a truly incoherent process (RU; ETCHEGOIN, 2008).

---

[5] The Lorentz model is one of the simplest models, which allows the calculation of $\hat{\alpha}_{inc}$ it from a microscopic molecule description (RU; ETCHEGOIN, 2008).

2.1.2 Raman activity and Molecular Vibrations

As molecule vibrations ultimately cause the Raman effect, it is crucial to comprehend how these vibrations alter molecules' optical characteristics. That is why creating a phenomenological Raman polarizability tensor connects it to the molecule's microscopic characteristics. Therefore, we decide to adopt a more straightforward classical approach for this theoretical description[6]. This approach is enough to show the majority of critical concepts, such as vibrational modes, the Raman tensor, and their symmetry [7] (RU; ETCHEGOIN, 2008).

When atoms interact with other atoms in the molecule, restoring forces allow them to vibrate around their equilibrium positions. Small amplitude vibrations will cause the electronic structure to change, which will cause a slight change in $\hat{\alpha}_{inc}(\omega)$. Accordingly, a particular vibrational mode will cause a 'modulation' of the linear optical polarizability at a frequency equal to the internal vibration, which results in Raman scattering. From the classical (and semi-classical) approach here, it should be possible to derive the Raman polarizability from studying the small perturbations of $\hat{\alpha}_{inc}(\omega)$ by the internal vibrations (RU; ETCHEGOIN, 2008).

In terms of atomic motion, a molecule made up of N atoms (N $\geq$2) has 3N internal degrees of freedom or three coordinates (x_i; y_i; z_i) [m] for each atom i. For a whole rigid structure, three of these degrees of freedom can assign to translations (along three independent directions of space), and three additional (or two in the case of linear molecules) degrees of freedom can give to rotations along three (independent) axes of space. The remaining degrees of freedom, $3N-6$ ($3N-5$ in linear molecules), are related to internal deformations of the molecule (LANDAU; M, 2004).

The *normal vibrational modes* $3N-6$ ($3N-5$ for linear molecules) can easily explain these vibrational degrees of freedom. All atoms in a molecule *oscillate at the same frequency* ω_k for a given normal mode k (k=1...3N−6), which corresponds to a specific vibrational pattern (displacements from equilibrium). Since a depth mathematical description, a normal mode is an eigenvector of the dynamic matrix of the molecule around equilibrium, defined by its geometry and the interatomic interactions, with its corresponding eigenvalue ω_k (coming from the electronic structure). The degrees of freedom for translation and rotation can also divide into six additional normal modes. In this case, these modes have zero frequency because there is no restoring force (for rotations, this is only true in the classical treatment.).

The 3N atomic displacements corresponding to the atomic coordinates ((x_i;

---

[6] As before, this also may be discovered using a complete quantum theory, which would also support the justification for describing the phenomenon as a radiating induced Raman dipole.

[7] This method's biggest drawback, however, is that it no longer works when there is resonant Raman scattering (RRS). More detailed descriptions are required (LONG; LONG, 2002).

y_i; z_i) for each of the N atoms) relative to their equilibrium positions (i.e., all ξ_i=0 at equilibrium) can be used to describe the positions of the atoms in a molecule. For example, using $3N$ *reduced-mass coordinates* or *mass-weighted coordinates*, with q_i [kg$^{1/2}$· m] defined as $q_i = \sqrt{m_i}\xi_i$, where m_i is the atom's mass whose displacement described by ξ_i is the more typical in vibrational analysis. Additionally, it is possible to define mass-weighted *normal mode coordinates*, also known as *normal coordinates*, Q_k [kg$^{1/2}$· m], which offer a comparable description of the atomic displacements that is particularly well suited to vibrational analysis. In other words, if a molecule oscillates freely with a pattern exactly matching a given normal mode k (and thus at a given frequency ω_k), then the normal coordinates are Q'_k=0 for all $k' \neq k$, and the motion of all atoms can then describe in terms of a single scalar $Q_k(t)$ oscillating at ω_k. Therefore, the normal coordinates Q_k measure the deformation's amplitude following the pattern of a specific normal mode k.

Figure 3 – Basic types of the normal vibrational modes. *Arrows* show directions of deflections of atoms, *plus* and *minus* signs indicate deflections of atoms above and below the plane.

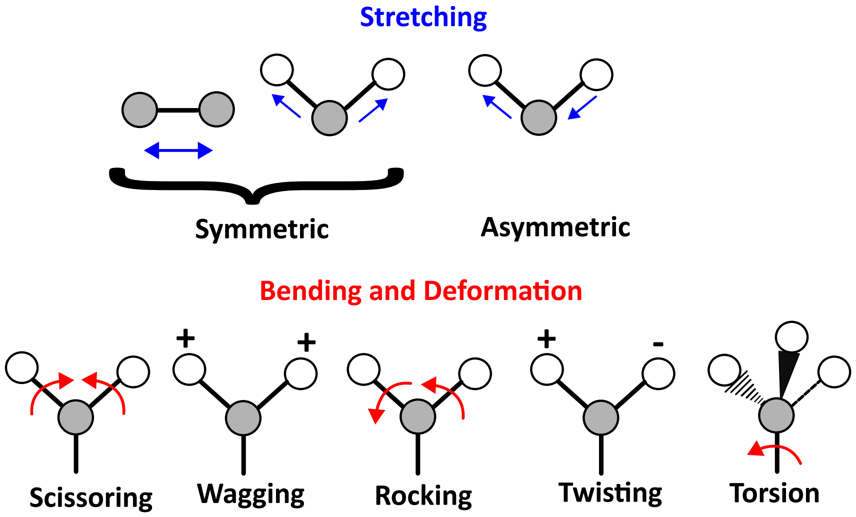

Source: Adapted from (PROCHÁZKA, 2016).

The normal vibrational modes can be divided into three categories (see Figure 3): (1) Valence stretching vibrations (ν) represent an atom-to-atom bond's expansion and contraction without a change in the bonding angle. (2) Vibrations that cause bending or deformation (δ), also known as scissoring, wagging, rocking, and twisting. (3) Bonds can vibrate in torsion by being twisted around their principal axes. The vibrations in systems with more than two atoms might be symmetrical or asymmetrical around the center. Any bond is said to be "in plane" if there is no change in the angle between it and the plane formed by the remaining atoms. Vibrations that are "out of plane" are the opposite situation. Vibrational modes can also divide into parallel and perpendicular types based on the geometric relationship between a given vibrational mode's transition moment and its symmetry axis.

The optical response (induced dipole) of a molecule excited by a laser at angular frequency ω_{inc} characterize by its linear optical polarizability $\hat{\alpha}_{inc}(\omega_{inc})$. This linear optical polarizability changes if the atoms depart from their equilibrium position, which consequently affects the electronic wave functions/density; thus, inc depends on the atomic coordinates (x_i; y_i; z_i); and changes due to the internal vibrations. Therefore, the influence on $\hat{\alpha}_{inc}$ of a particular normal mode k, defined by Q_k and using Taylor expansion, can approximate to:

$$\hat{\alpha}_{inc}(Q_k) = \hat{\alpha}_{inc}(0) + \left(\frac{\partial \hat{\alpha}_{inc}}{\partial Q_k}\right)_{Q_k=0} Q_k + \frac{1}{2}\left(\frac{\partial^2 \hat{\alpha}_{inc}}{\partial Q_k^2}\right)_{Q_k=0} Q_k^2 + \ldots, \tag{2.11}$$

where the following terms (also second-rank tensors) are the first and second-order perturbations brought on by atomic movements that follow the normal mode pattern (which is characterized by the scalar amplitude Q_k), and $\hat{\alpha}_{inc}(0)$ is the unperturbed (at equilibrium) linear optical polarizability.

The polarizability derivative, also known as a *Raman tensor*, $\hat{R}_k(\omega_{inc})$ [$\epsilon_0 \cdot \mathrm{m}^2 \cdot \mathrm{kg}^{-1/2}$], of the normal mode k, can be used to explain the change in polarizability caused by a particular vibrational mode k[8]:

$$\boxed{\hat{R}_k(\omega_{inc}) = \left(\frac{\partial \hat{\alpha}_{inc}(\omega_{inc})}{\partial Q_k}\right)_{Q_k=0}.} \tag{2.12}$$

The effect of the vibration on $\hat{\alpha}_{inc}$, in terms of the Raman tensor for small oscillations and for particular normal mode k, is[9]

$$\hat{\alpha}_{inc}(\omega_{inc}, Q_k) = \hat{\alpha}_{inc}(\omega_{inc}, 0) + Q_k \hat{R}_k(\omega_{inc}). \tag{2.13}$$

The link between the Raman polarizability with the vibrations (molecule's microscopic properties) through the classical treatment is successful and useful because it predicts the existence of Stokes and anti-Stokes scattering, however, it does present a number of limitations: (1) It ignores the spontaneous generation of a vibration, with leads to an inaccurate prediction of the Stokes Raman polarizability's magnitude. (2) Linking quantitatively $\hat{\alpha}_{inc}(\omega_{inc})$ to the microscopic properties of the molecule or to its electronic structure requires additional steps. (3) The validity of the Taylor expansion in Equation 2.11 might not hold in all situations, even when $\hat{\alpha}_{inc}(\omega_{inc})$ is known. This

---

[8] For more Stokes-Raman scattering details see (RU; ETCHEGOIN, 2008).

[9] At this point, it is enticing to formally express Q_k time dependence and take into account its linear polarizability. However, such a strategy runs counter to $\hat{\alpha}_{inc}(\omega_{inc})$ fundamental definition as a response function.

becomes particularly significant in resonant Raman scattering conditions, where a semi-classical approach becomes essential. (4) The Taylor expansion in Equation 2.11 pertains to the normal mode coordinate Q_k, which assumes prior knowledge of the eigenvectors for various vibrations. This information may be accessible for relatively uncomplicated small molecules.

2.2 Surface Enhanced Raman Spectroscopy

The fundamental principle of Surface Enhanced Raman Spectroscopy (SERS) spectroscopy is based on the considerable enhancement of Raman scattering of molecules adsorbed on suitable metallic nanostructures, primarily silver, and gold. The electromagnetic process (EM), based on resonance excitations of the metal's surface plasmons, and the chemical (or molecular) mechanism, which increases the molecule's polarizability, contribute to the total enhancement. Average enhancement factors range from 10^4 to 10^6, while values as high as 10^{11} might be attained in certain circumstances (PROCHÁZKA, 2016; FASOLATO, 2018; RU; ETCHEGOIN, 2008). The fundamentals of SERS theory and various experimental elements of SERS, such as enhanced mechanisms and factors for developing solid SERS substrates, will be briefly covered in this section.

2.2.1 SERS Mechanisms

Figure 4 – When a molecule is adsorbed onto nanostructured particles, enhanced Raman scattering occurs, which produces Stokes and anti-Stokes scattering—radiation that has a lower (red) or higher (blue) frequency than the incident light—respectively.

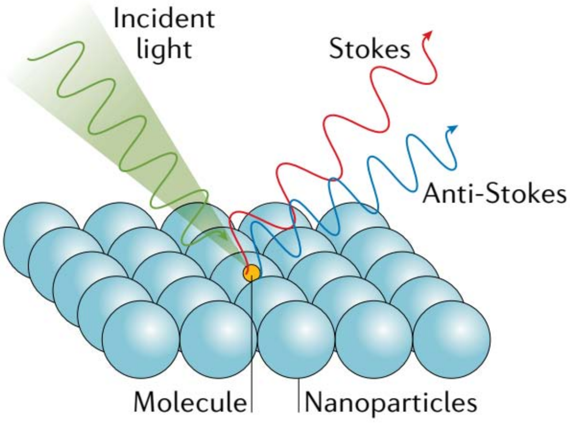

Source: Adapted with permission from (HAN et al., 2022).

The magnitude of the induced dipole moment $\tilde{\mathbf{P}}_{inc}$ that defines the RS effect (see equation 2.10), is given by the relationship between the molecular polarizability of the molecule and the local electric field $\tilde{\mathbf{E}}$ of the frequency ω_{inc}. Consequently, two potential methods help to enhance the RS effect. $\tilde{\mathbf{E}}$ or $\hat{\alpha}_{inc}$ must be improved when the molecule interacts with a rough metal surface. Thus, two primary multiplicative factors contribute to SERS enhancing process: the electromagnetic and the chemical (or molecular) mechanism (PROCHÁZKA, 2016). Figure 4 represents the enhanced Raman scattering of a molecule adsorbed onto nanostructured particles and the Stokes and anti-Stokes scattering. Nowadays, this Raman enhancement can be obtained by popular nanostructured materials such as nanoparticles (NPs), roughened films, or nano-patterned substrates (KNEIPP; OZAKI; TIAN, 2017; HAN et al., 2022).

Electromagnetic Mechanism

The electromagnetic mechanism (EM) is associated with the presence of a metal surface. When a metal nanostructure is irradiated with incoming light (E_{inc}), the conductive electrons undergo delocalization, leading to collective oscillations that generate an electromagnetic (EM) field around the interface formed by the metal nanostructure and the dielectric environment, as depicted in Figure 5(a). The frequency of these electron oscillations depends on factors such as the density of electrons, the effective electron mass, and the shape and size of the charge distribution (KELLY et al., 2003; PÉREZ-JIMÉNEZ et al., 2020).

If the frequency of the incoming radiation (ω_{inc}) resonates with that of the electron oscillation, the excitation process is referred to as surface plasmon resonance (SPR). SPR can either propagate as a longitudinal wave along extended metal surfaces or remain highly localized in specific regions, such as edges, tips, or crevices at the interface between the metallic surface and the dielectric. These localized modes are known as surface plasmon polaritons (SPPs) and localized surface plasmon resonance (LSPR), respectively (RU; ETCHEGOIN, 2013; DING et al., 2016).

The plasmonic nature of metallic nanoparticles leads to the intense absorption and scattering of light. Furthermore, the interaction between electromagnetic radiation and surface plasmons can result in a significant amplification of the optical fields in the vicinity of the metal surface (see Figure 5(a)).

Since nanoparticle sizes are typically much smaller than the wavelength of light in the UV-visible spectral ranges, localized surface plasmons can confine light, which arises from the coupling of photons with electronic excitations inside the nanostructures. The eigenmodes of surface plasmons are solutions to the Helmholtz equation, with their appropriate boundary conditions (FASOLATO, 2018; NOVOTNY; HECHT, 2012):

$$\nabla \times [\nabla \times \mathbf{E}(\mathbf{r}, \omega)] - \frac{\omega^2}{c^2}\epsilon(\mathbf{r}, \omega)\mathbf{E}(\mathbf{r}, \omega) = 0 \tag{2.14}$$

If we assume that nanoparticles' sizes, which sustain the plasmonic excitation, are smaller than the metal's skin depth, denoted by $d = \lambda/(4\pi\sqrt{\epsilon})$, we can adopt the

Figure 5 – Schematic representation of Localized surface plasmon resonance (LSPR) effect: (a) metal conductive electrons are stimulated into collective oscillations, producing a highly localized electromagnetic field at the metal-dielectric interface upon light irradiation. (b) The interaction between nanoparticles and molecules, by the local EM field (depicted by the green arrow), results in the mutual excitation of the Raman polarizability (indicated by the thin red arrow). This interaction leads to the generation of an enhanced Raman signal of the molecule, as indicated by the thick red arrow.

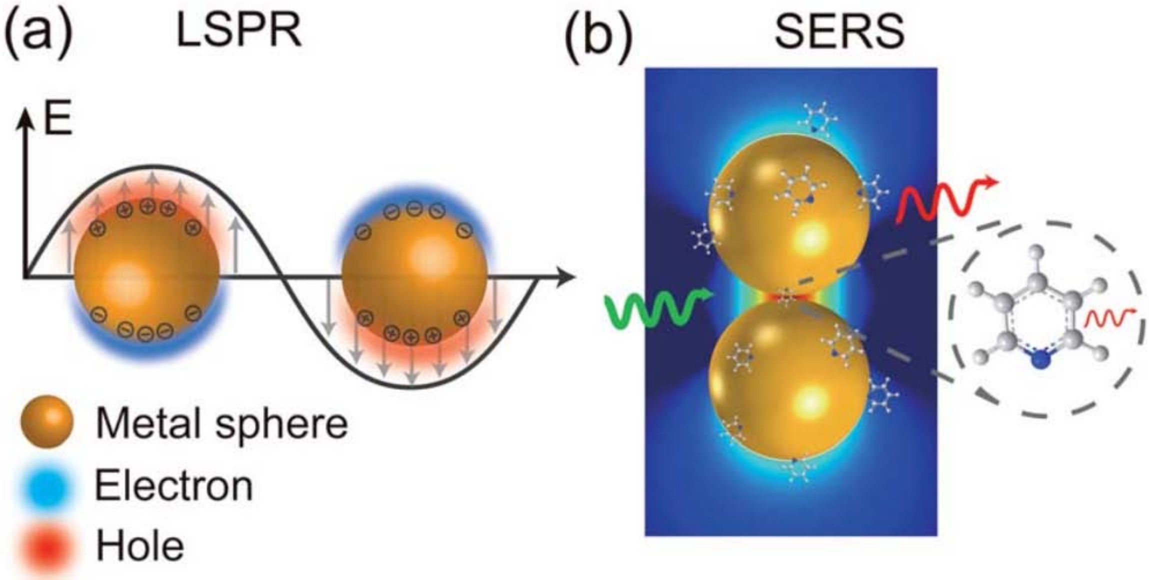

Source: Adapted with permission from (PÉREZ-JIMÉNEZ et al., 2020).

quasi-static approximation (FASOLATO, 2018). Consequently, retardation effects can be neglected, assuming synchronous responses from all nanoparticle points to the external field perturbation. This results in the periodic displacement of the entire free electron gas with respect to the stationary crystal lattice of the particle, as depicted in Figure 5(a).

In the context of the quasi-static approximation, the Helmholtz equation 2.14 simplifies into the Laplace equation, and its solutions describe quasi-static near fields. One such example is the electric field generated by an oscillating dipole, represented as $\mathbf{p}$,

$$\mathbf{E}(r\mathbf{n},t)=\frac{1}{4\pi\epsilon_0}\left[k^2\mathbf{n}\times\mathbf{p}\times\mathbf{n}\frac{e^{ikr}}{r}+[3\mathbf{n}(\mathbf{n}\cdot\mathbf{p})-\mathbf{p}]\left(\frac{1}{r^3}-\frac{ik}{r}\right)e^{ikr}\right]e^{i\omega t} \tag{2.15}$$

can be reduced in the near-field zone $kr \ll 1$ to the following:

$$\mathbf{E}(r\mathbf{n},t)=\frac{1}{4\pi\epsilon_0}[3\mathbf{n}(\mathbf{n}\cdot\mathbf{p})-\mathbf{p}]\frac{e^{i\omega t}}{r^3} \tag{2.16}$$

This represents the electrostatic field of a stationary point dipole oscillating harmonically with a time dependence of $e^{i\omega t}$. In the quasi-static regime, the electric field can be denoted as $\mathbf{E} = -\nabla\Phi$ with the potential Φ satisfying the Laplace equation 2.17, as well as the boundary conditions between the metal and the dielectric material that surrounds the nanoparticle.

$$\nabla^2\Phi = 0. \tag{2.17}$$

These expressions are general and can be solved for various geometries of the system. In the quasi-static approximation, we neglect the generation of electric multipolar modes by the exciting fields (FASOLATO, 2018).

In summary, we must give careful attention to the size of the metallic features to optimize the SERS activity of our system: They need to be small enough compared to the wavelength of the exciting light to prevent the excitation of multipolar plasmonic modes. And they must be large enough for the scattering contribution to outweigh the absorption phenomena. From an experimental point of view, if we consider particles with diameter d much smaller than the wavelength λ of the exciting light ($d \ll \lambda$), each excited nanoparticle will act as an electric dipole. With this kind of system, two types of electromagnetic interactions between particles can be distinguished: near-field and far-field coupling (MAIER et al., 2002; PINCHUK; SCHATZ, 2008).

For very short interparticle spacing Λ, such as nearly touching nanoparticles ($\Lambda \sim d$), the most relevant effect is the near-field coupling (HAO; SCHATZ, 2004; ZHU; ZHU; LIU, 2004), and the interaction of the nanostructures is driven by the electrostatic field. For particle spacings $\Lambda \gg d$ and $\Lambda \sim \lambda$, far-field dipolar interactions become dominant. In such interparticle couplings, interference effects can modify the plasmon resonance profile of each nanostructure (FASOLATO, 2018).

Single, non-interacting nanoparticles contribute almost linearly to the SERS signal. However, the interplay between near- and far-field interparticle coupling effects can remarkably modify the local field distribution, leading to significantly higher signal enhancement (ZHU; ZHU; LIU, 2004). A compelling example is observed in SERS from colloidal systems, where nanoparticle-based substrates exhibit strong near-field enhancements at the interstices between closely packed nanoparticles, commonly referred to as “hot spots”. These “hot spots” play a pivotal role in augmenting the spectroscopic signal (LI; STOCKMAN; BERGMAN, 2003; GUNNARSSON et al., 2001; ALEXANDER et al., 2009). Consequently, nanoparticle aggregation is often induced to enhance the substrate’s performance by maximizing the number of “hot spots” within the structure (FASOLATO et al., 2014). Additionally, one- or two-dimensional arrays of far-field coupled metal nanoparticles can also yield significant SERS signal enhancements (YAN et al., 2009), offering intriguing features linked to their regular geometry (DOMENICI et al., 2016; HAYNES et al., 2003).

In general, the local EM field (E_{loc}) associated with the LSPR is of a higher magnitude than the incident EM field, resulting in the enhancement of the EM field in SERS by a factor of $G_{ex} = [E_{loc}(\omega_{inc})/E_{inc}(\omega_{inc})]^2$.

Similarly, other sources of oscillation, such as dipoles (i.e., modified Raman dipole, P_{inc}), or quadrupoles, also contribute to the excitation of the LSPR. Typically, the Raman polarizability of molecules interacting with metal nanostructures (P_{inc}) is approximately one to three orders of magnitude larger than that of free molecules (PÉREZ-JIMÉNEZ et al., 2020). Therefore, the interaction between molecules and vicinal metal nanostructures results in the mutual excitation of the Raman polarizability by the local EM field, and vice versa (Figure 5(b)). This process leads to an enhancement of the EM field in SERS, quantified by a factor of $G_s = [E_{loc}(\omega_s)/E_{inc}(\omega_s)]^2$. For Raman modes with low vibrational frequency, ω_{inc} can be approximated to ω_s, making the EM field enhancement factors $G_{ex}(\omega_{inc})$ and $G_s(\omega_s)$ comparable. As a result, the overall enhancement of the EM field in SERS (G) scales with the fourth power of the local EM field enhancement (DING et al., 2016), as expressed below[10]:

$$G = \frac{|E_{loc}(\omega_s)|^4}{|E_{inc}(\omega_{inc})|^4} \approx \mathrm{EF}_{\mathrm{EM}} \tag{2.18}$$

Therefore, even a slight change in the local field enhancement can result in a significant variation in SERS enhancement. Additionally, when two nanoparticles are positioned within a 1 nm distance from each other, their plasmons can couple together. As a consequence, the SERS signal of a molecule placed in the $\sim$1 nm^3 volume of the gap between the nanoparticles (hot spot region) can be enhanced by as much as 9 to 12 orders of magnitude, while it may rapidly decay with increasing distance from the hot spot. Consequently, molecules adsorbed inside and outside the hot spot will exhibit vastly different Raman intensities. Presently, achieving precise control over the distance between nanoparticles remains a challenge, which contributes to the low reproducibility observed in SERS measurements (HALAS et al., 2011; ETCHEGOIN; RU, 2008; DING et al., 2017; PÉREZ-JIMÉNEZ et al., 2020).

Chemical Mechanism

The chemical mechanism (CM) involves all phenomena contributing to the increment of the SERS signal through the molecule's interaction with the metal substrate, representing all non-plasmon-related sources of enhancement. Chemical enhancement does not solely occur in the case of metal substrates but is also significant in the SERS signal from molecules located on semiconductor nanostructures (SUN; ZHAO; LOMBARDI, 2007; WANG et al., 2012), or graphene (LING et al., 2015). Within the molecule-metal

---

[10] Equation 2.18 represents the $|E|^4$-approximation for zero Raman shift (RU; ETCHEGOIN, 2013).

system, three sources of enhancement must be considered; the last two aspects originate the chemical effects (FASOLATO, 2018):

- The metal nanostructure provides electromagnetic enhancement, as discussed in Section 2.2.1.
- Vibratory excitations in the molecule can also contribute to the increment of the spectroscopic signal. This is known as a resonant Raman process or Surface Enhanced Resonant Raman Scattering (SERRS).
- The interaction between the metal and the molecule leads to two effects: on one hand, a change in the molecular polarizability, and on the other hand, the emergence of new metal-to-molecule or molecule-to-metal charge transfer resonances.

Molecular resonance enhancement: It is essential to note that large Raman cross-sections do not necessarily imply large enhancement factors concerning the resonant molecular contribution. The enhancement factor is defined as

$$EF = \frac{I_{SERS}}{I_{Raman}} \frac{N_{Raman}}{N_{SERS}}. \tag{2.19}$$

Thus, for a single molecule, $EF = I_{SERS}/I_{Raman}$. As resonant excitation influences the spectroscopic intensity in both Raman and SERS cases, one might assume that will not significantly contribute to the SERS enhancement factor. However, there is an important exception: for strongly fluorescent molecules, the isolated molecule fluorescence process competes with resonant Raman, hindering its observation (RU; SCHROETER; ETCHEGOIN, 2012). When the molecule is in proximity to a metal surface, fluorescence undergoes quenching (CHANCE; PROCK; SILBEY, 1974), favoring the Raman process. This effect strongly contributes to the molecular resonance chemical enhancement factor (EF) (MOSKOVITS, 2013).

Metal-molecule charge-transfer (CT) effects: Various models are employed to describe enhancement mechanisms based on the interaction between the metal and the molecule. The discrimination between non-resonant or resonant effects is now widely accepted (JENSEN; AIKENS; SCHATZ, 2008; KNEIPP, 2016).

The "static charge-transfer" mechanism highlights the formation of a metal-ligand complex, leading to modifications of the molecular polarizability. These changes are not associated with any resonant excitation in the system (JENSEN; AIKENS; SCHATZ, 2008), yet they can significantly increase the Raman cross-section of the molecule (KNEIPP, 2016).

The "resonant charge-transfer" model involves the formation of new intermediate electronic levels in the ligand-metal complex (LOMBARDI et al., 1986). This results in the emergence of novel metal-to-molecule or molecule-to-metal charge transfer excitations, frequently observed in coordination complexes of transition metals (MOSKOVITS, 2013; OTTO, 2005). As the Fermi level (E_f) of metals lies between the energy of the highest occupied and the lowest unoccupied molecular orbitals (HOMO and LUMO as shown in Figure 6), the formation of the ligand-metal complex facilitates new transitions. While the HOMO-LUMO transition typically corresponds to photon energies in the ultraviolet range, these new transition channels become active at lower energies and can be excited with visible photons. This phenomenon occurs upon interaction with noble metals, transition metals, or semiconductors (WANG et al., 2012).

From Figure 6, the incident photon frequency ω_{inc} resonates with the freshly created surface-adsorbate complex's charge-transfer (CT) transition. The electron then returns to the metal. If the electron stays in the molecule long enough, scattered photons ($\omega_s = \omega_{inc} - \omega_{vib}$) will carry information about the molecule's vibrational state (ω_{vib}). In the case of a metallic electrode, the applied voltage or the excitation wavelength can change the energy of the E_f (PROCHÁZKA, 2016).

Figure 6 – Charge-transfer (CT) mechanism to SERS at a metal–molecule or semiconductor–molecule interface. The CT transition (μ_{CT} and arrows (green: metal–molecule; purple: semiconductor–molecule) show the CT directions. Red and white spheres represent molecular orbitals. CB, conduction band; E_F, Fermi level; HOMO, highest occupied molecular orbital; LUMO, lowest unoccupied molecular orbital; VB, valence band

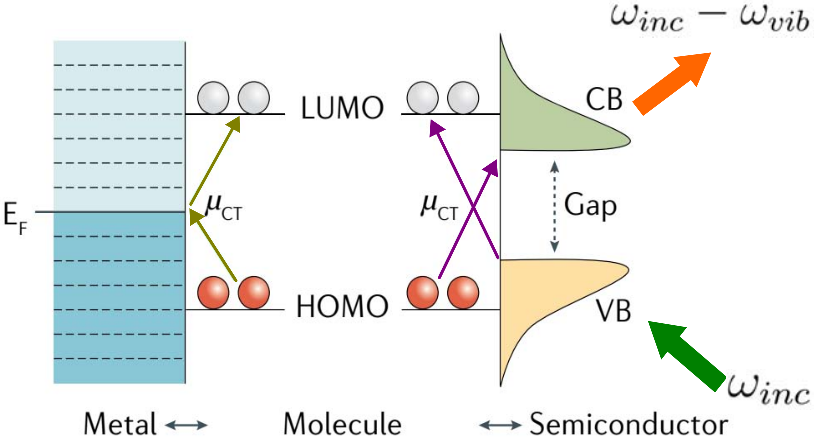

Source: Adapted with permission from (HAN et al., 2022; PROCHÁZKA, 2016).

For semiconductors materials, an energy gap between their full valence band and empty conduction band, the energy levels of which may function in CT processes like the E_f of plasmonic NPs (LOMBARDI; BIRKE, 2014) (see figure 6). The two systems are not mutually exclusive and contribute to overall SERS signals. In a metal-semiconductor heterostructure, the combined effect of plasmons and CT can produce remarkable SERS signals (LIU et al., 2021; TANG et al., 2022; WANG et al., 2012).

The last phenomenon to consider is the "transient charge transfer" (MOSKOVITS, 2013): here the Raman scattering occurs through the temporary transfer of hot electrons or electron-hole pairs from the metal to the adsorbed molecule (OTTO, 2005). These theories propose that the excitation of plasmons in the metal nanostructure generates "ballistic" (hot) electrons (MICHAELS; NIRMAL; BRUS, 1999) or electron-hole pairs (PETTINGER, 1986), which, upon interaction with the adsorbate, contribute to the enhancement of the SERS signal by coupling of the molecular vibrations with the plasmonic transition dipole (FASOLATO, 2018).

The chemical mechanism is often weaker than the electromagnetic mechanism. Both experimental and theoretical estimates suggest an EF of 10^0-10^2 depending on chemical structure, metal contact, and specific vibration (VALLEY et al., 2013). However, it is demonstrated that chemical contributions to SERS are significant for materials exhibiting surface plasmon resonance absorption at wavelengths other than frequently employed laser excitation wavelengths (HAN et al., 2017). Moreover, according to the chemical enhancement theory (CHOWDHURY, 2015), CT contributes to SERS.

The distinction between EM and chemical mechanisms is often difficult; nevertheless, calculations of the charge difference density have been used to provide concrete evidence for the charge-transfer mechanism and to distinguish it from the EM mechanism (XIA et al., 2014). Recently, many studies have combined these mechanics' advantages to improve SERS performance.

2.2.2 Solid SERS-Active Substrates

The SERS substrate plays a critical role in SERS spectroscopic application. Since the discovery of SERS, noble metal nanoparticles such as gold, silver, and copper have been widely used because of their ideal SERS signal amplification and simple production process (ZHANG et al., 2020). However, molecule SERS performance, including stability and sensitivity brought on by metallic colloids, depends mostly on the state of aggregation of metal nanoparticles, requiring a good detection environment and strengthening molecule-metal contacts (HU et al., 2014). As a result, several matrices have been combined with noble metal nanoparticles in SERS analysis to improve the inherent instability of metallic colloids. Those matrices include Au-core silica-shell nanoparticles (SiO_2 or Al_2O_3) (LI et al., 2013), polymers (RENARD et al., 2019), metal-organic frameworks (MOFs) (PHAN-QUANG et al., 2019; CARRILLO-CARRIóN et al., 2019), semiconductors (LIU et al., 2009; QUAN et al., 2019), and carbon materials (CHEN et al., 2016; TANG; AN; ROW, 2020). Modifying the substrate's form can also produce high-quality substrates capable of producing sensitive and stable SERS signals. Because of their excellent sensitivity, high stability, customizable shape, and practical transport, solid SERS substrates have been created in increasing numbers in recent years. Solid

SERS substrates are a type of SERS substrate with solid characteristics as opposed to colloid substrates, mainly by lowering the need for sample pretreatment. General SERS experiments on liquid substrates will be limited by unstable signals, decreased SERS activity, and a short storage period.

The solid SERS substrates have notable characteristics in numerous areas due to the higher density of hot spots per unit area, good repeatability, and reproducibility, providing uniform and stable SERS signals and mainly lowering the need for sample pretreatment. These sturdy platforms have clearly defined features that give the nanostructures support stability and increase or produce coupling of various SPR modes for enhanced Raman signal amplification. In addition, the issue of uncontrolled nanoparticle aggregation is resolved because the SERS active nanostructures are fixed on the surfaces of 1D, 2D, and 3D solid platforms. Additionally, this method enables control of the inter-nanoparticle distances, which are essential for forming hot spots (LIN et al., 2009). The electric field amplification increases noticeably when the adjacent nanoparticles are less than 2 nm apart (SARFO et al., 2019; ZOU; SCHATZ, 2005). Given these advantages designing high-quality solid SERS substrates can significantly increase SERS analytical performance (GE; HU; LI, 2022).

Immobilization procedures such as printing/writing (MARTINS et al., 2021; DUAN et al., 2020; YILMAZ et al., 2019; KUMAR; SANTHANAM, 2019), filtration (GE et al., 2021), self-assembly (LIM et al., 2019; XING et al., 2020; WANG et al., 2020), spin coating (CASTRO-GRIJALBA et al., 2020; ZHAO et al., 2018; PANIKAR et al., 2018), magnetron sputtering (LI et al., 2019; SHI et al., 2018), surface modification (MHLANGA; DOMFE; SKEPU, 2019), deposition (KIM et al., 2020), in-situ generated (ZHANG et al., 2019), and immersion, among others, can be used to manufacture solid SERS substrates. Despite the advantages of surface treatment, issues like the lengthy surface modification process and substrate inhomogeneity still need to be resolved. Finally, the uncommon usage of the other fabrication techniques, including deposition, in-situ growth, and immersion, supported the need for more research and development in solid SERS fabrication (GE; HU; LI, 2022).

Plasmonics must be implemented in low-cost, homogenous functional nanostructured materials that can be produced on a broad scale to fully realize the sensing potential of the technology outside of the research setting. For this, two-dimensional (2D) SERS substrates have increased optical stability, repeatability, and signal acquisition (QIANGTING et al., 2022). One of the 2D-SERS substrates with simple, cost-efficient production and low-cost base on the regular distribution of metallic nanoparticles through periodically structured surfaces (grating pattern surface) from standard recordable disks, such as CD-R, DVD-R, and others, which show noticeable Raman amplification (QIANGTING et al., 2022; DONG et al., 2021; NGUYEN; NGO et al., 2020; BHARATI et al., 2019; AVELLA-OLIVER et al., 2018; RADU et al., 2016; LEORDEAN et al., 2015; GIALLONGO et al., 2011). The nanostructure on the polycarbonate substrate, the silver thickness, and the excitation wavelength all affect how much improvement there is (AVELLA-OLIVER et al., 2018).

For metal grating or metal substrate structures, such as grooves and slits on the metal surface, the surface plasmon polariton (SPP) effect will produce when the external field is incident on the photons of a particular frequency and the free electrons on the surface of the metallic nanostructure resonantly couple. Furthermore, suppose the oscillation frequency of the free electrons on the metal surface and incident light frequency coincides. In that case, the local electromagnetic field around the metal will strengthen, and a local surface plasmon resonance (LSPR) effect will be produced (LONG et al., 2017; BARNES; DEREUX; EBBESEN, 2003; DONG et al., 2015). The electric field amplitude decays exponentially along the vertical direction of the interface, and the electromagnetic mode propagates horizontally together with the interface between the metal substrate's surface and the medium (ZAYATS; SMOLYANINOV; MARADUDIN, 2005; LU et al., 2017).

Metal gratings, which have the highest order, periodicity, and homogeneity among nanostructures with a 1D layout, can increase the accuracy of molecular detection when utilized as the SERS substrate. The energy can concentrate in a metal slit much narrower than the wavelength of the incident light using the metal grating structure. As a result, the TM wave's wavelength performance and transmission properties, when it is perpendicularly incident, are superior to those of other structures. One way to satisfy the SPP effect wave vector and photon matching is to use a metal grating structure. Photons can produce the SPP effect and strengthen the local electromagnetic field on the metal grating surface when the wave vector matching conditions are met (JIANG et al., 2011).

The diffraction effect of the metal grating modifies a portion of the wave vector component when an external field laser stimulates the surface of the metal grating structure, allowing the electromagnetic wave to propagate along with the air-metal interface. The SPP effect's electromagnetic wave will travel through the metal grating's uneven surface, increasing the overall area of the grating structure in the process. As a result, the local electric field strengthens, and the dipole's resonance effect promotes by the SPP wave's increased propagation path on the grating structure's surface. In addition, the SPP phenomenon can be excited at the interface between metal-dielectric when the wave vectors k_x of incident light along the reflecting interface are equivalent to the wave vectors k_{sp} of SPP (SU et al., 2021). Metal gratings are an excellent structure for SERS augmentation because of this (LI et al., 2020).

In general, the continuous metal nano-particle coverage generates the coupling effect of LSPR and SPP, which improves the local electromagnetic field on the surface

Figure 7 – Schematic of the DVD-R grating surface-based SPR sensor regarding 1st order (±1) light diffraction at reflection and transmission mode.

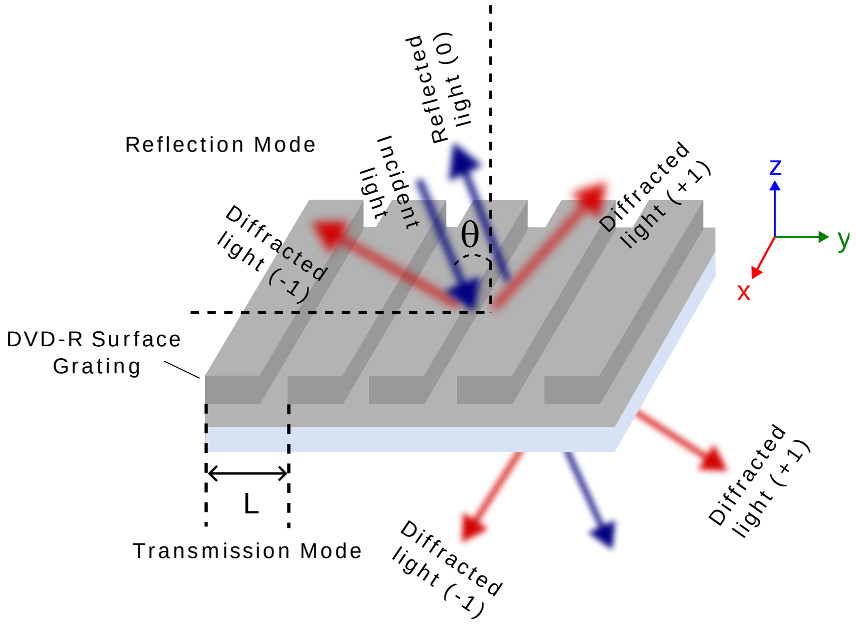

Source: Adapted with permission from (AHMED et al., 2020).

of the DVD-R grating/AgNPs hybrid substrate. The LSPR and SPP coupling effect is responsible for the experiment's increased Raman signal. The substrate's LSPR's dispersion relation is (CHANG; HUANG; LIN, 2020):

$$k_{sp} = \frac{2\pi}{\lambda_{sp}} = \frac{2\pi}{\lambda_0}\sqrt{\frac{\epsilon_m \epsilon_d}{\epsilon_m + \epsilon_d}}, \tag{2.20}$$

where k_{sp} represents the surface plasmon (SP) wave vector, λ_{sp} is the surface plasmon wavelength, and λ_0 is the wavelength of the incident light. ϵ_m is the dielectric constant of the surrounding environment, and ϵ_d is the dielectric constant of the metal. We require a grating structure to introduce additional wave vector difference since the free space wave vector k_x is smaller than the SPP wave vector k_{sp}. Therefore, the diffraction of light on a grating is the basis for the excitation of surface plasmon (see figure 7) (SU et al., 2021). The resonant surface plasmon wavelength for the metal-dielectric interface can be calculated by substituting the corresponding permittivity values into equation 2.20.

The standing SP wave will be generated at the interface when the transverse dimension of the grating and the surface plasmon's wavelength coincide. The resonant SP standing wave across the grating present the following condition:

$$k_{sp} \cdot \frac{L}{2} = m\pi, \tag{2.21}$$

where m is the diffraction order (an integer) and L is the grating period (see figure 7). For DVD-R, the measured grating period is around 750 nm; according to 2.21, the grating period is 782 nm for m=2. Thus, the estimated and experimental grating periods are nearly identical, which could explain the impact of LSPR on the SERS signal (DONG et al., 2021). For the SPP effect, the excitation angle must fulfill the SP dispersion relationship in the following equation for SPP to be excited on the interface surface (CHANG; HUANG; LIN, 2020):

$$k_{sp} = \frac{2\pi}{\lambda_0} \sin\theta \pm m\frac{2\pi}{L}, \tag{2.22}$$

where θ is the incident angle (see figure 7), m refers to diffraction's order (an integer). Equation 2.22 shows that the SPP effect can be formed on the interface surface when the grating period and incidence angle satisfy the corresponding conditions and that the SERS signal strength can subsequently be influenced by coupling with LSPR (DONG et al., 2021).

The DVD serves as a 2D solid platform for SERS detection, attributed to the standard grating structure that we have examined. Nonetheless, various forms of solid template arrays or self-assembled substrates have been extensively researched (HANSKE et al., 2019). These alternatives enable precise manipulation of morphology, lateral spacing, and macroscale homogeneity. The precise control of noble metals at the nanoscale ensures significant and stable SERS signals, exhibiting great potential for SERS analysis. Some chemically stable supports also provide an excellent protective effect for noble metals, significantly extending storage time and expanding the scope of SERS analysis. For example, the fabrication of solid self-assembly substrates based on nanostructure templates such as Porous Silicon (SARFO et al., 2019; FANG et al., 2020; KHINEVICH et al., 2021; ŠKRABIĆ et al., 2019).

Porous silicon (PSi) was accidentally discovered by the Uhlirs at Bell Laboratories in the mid-1950s while attempting to develop an electrochemical method for machining silicon wafers used in microelectronic circuits. To their surprise, the silicon wafer did not dissolve uniformly under the intended electrochemical conditions; instead, it exhibited the formation of fine holes, primarily propagating in the $\langle 100 \rangle$ direction within the wafer.

The considerable interest in porous silicon, particularly in its nanostructure, occurred in the early 1990s. Ulrich Goesele at Duke University identified quantum confinement effects in the absorption spectrum of porous silicon, while simultaneously, Leigh Canham at the Defense Research Agency in England reported efficient and vibrant red-orange photoluminescence from the material (CANHAM, 1990; LEHMANN; GÖSELE, 1991). This revelation of efficient visible light emission from porous silicon triggered research on developing silicon-based optoelectronic switches, displays, and lasers. Simultaneously, the material's unique characteristics, such as its large surface area, controllable pore sizes, convenient surface chemistry, and compatibility with conventional silicon microfabrication technologies, inspired investigations into applications far beyond optoelectronics. Over time, numerous challenges related to chemical stability were overcome as the material's chemistry matured, leading to the emergence of diverse biomedical (SAILOR, 1997; CANARIA et al., 2002; HERINO et al., 1987) sensors, optics, and electronics applications (SAILOR, 1997).

The formation of porous silicon involves intricate reactions among Si–Si, Si–H, Si–O, and Si–F bonds occurring at the surface of the silicon crystal. Although one might assume that the strengths of these bonds solely determine the relative stability of each species on a silicon surface, the elements' electronegativity plays a crucial role (SAILOR, 2012).

Si–H and Si–C species tend to passivate the silicon surface in aqueous solutions, rendering it less reactive. Conversely, the Si–F bond exhibits high reactivity. This can be attributed to the electronegative nature of certain elements. For instance, elements as O and F form more polar Si–X bonds, which make the silicon atom vulnerable to nucleophilic attack (SAILOR, 2012).

Following the preparation of PSi, its surface is initially coated with a passivating layer primarily composed of Si–H bonds, accompanied by minor quantities of Si–F and Si–O species. This arrangement helps maintain the stability and reactivity of the material.

Silicon exhibits thermodynamic instability when exposed to air or water, leading to its spontaneous reaction and the formation of an oxide layer. This oxide layer can have varying degrees of nonstoichiometry and hydration, although its simple empirical formula is silicon dioxide, SiO_2 (see Equation 2.23). SiO_2 is a significant thermodynamic sink within the silicon system.

$$\mathrm{Si} + \mathrm{O_2} \rightarrow \mathrm{SiO_2} \tag{2.23}$$

SiO_2 acts as an electrical insulator, forming passivating films on crystalline silicon. Consequently, when preparing PSi, an additive is required in the solution to dissolve the oxide and enable the continuation of the electrochemical oxidation process. Among the bonds involved, the Si–F bond is the only bond more potent than Si–O, and its bond enthalpy plays a pivotal role in driving the primary chemical dissolution reaction for PSi production. In the presence of aqueous HF, SiO_2 spontaneously dissolves, forming SiF_6^{2-} (see Equation 2.24).

$$\mathrm{SiO_2} + 6\mathrm{F} \rightarrow \mathrm{SiF_6^{2-}} + 2\mathrm{H^+} + 2\mathrm{H_2O} \tag{2.24}$$

The silicon hexafluoride ion (SiF_6^{2-}) is a stable dianion exhibiting high water solubility. Therefore, fluoride is the most crucial additive in preparing PSi, effectively dissolving the insulating oxide layer that would otherwise impede the electrochemical corrosion reaction.

To complete the electrochemical reaction in PSi fabrication, two electrodes are required. One electrode supplies electrons to the solution (the cathode), while the other removes electrons from the solution (the anode). These electrodes are necessary to maintain charge neutrality and complete the electrical circuit. In an electrochemical cell, two reactions co-occur the anode (oxidation) reaction and the cathode (reduction) reaction. The anode is the electrode where oxidation occurs in an electrochemical cell, while the cathode is the electrode where reduction occurs. Electrons flow from the cathode to the anode, and a salt bridge maintains electrical contact and charge neutrality in the half-cells.

In a two-electrode cell, electrochemical reactions co-occur at both electrodes, although our focus is typically on the reaction occurring at just one of them. In PSi formation, the silicon electrode is the crucial site where silicon's chemical oxidation occurs, making it the anode. As for the cathode in PSi etching cells, platinum is commonly employed and is positioned a few millimeters to several centimeters away from the silicon electrode, with an electrolyte solution serving as the separator. At the platinum electrode, the primary electrochemical reaction involves the reduction of protons, producing hydrogen gas (SAILOR, 2012).

In water electrolysis, hydrogen gas is expected to form at the cathode, while oxygen gas should form at the anode. In this case, the platinum counter-electrode (cathode) generates hydrogen bubbles through water electrolysis. Interestingly, during the electrocorrosion of silicon, an unexpected release of hydrogen occurs. This phenomenon can be attributed to silicon's thermodynamically favored spontaneous water reduction. Although the reaction kinetics are sluggish when silicon is in its elemental form (oxidation state 0), the reaction becomes rapid when silicon is in its +2 oxidation state. As a result, water reacts with silicon, generating hydrogen and transforming silicon into its prevalent +4 oxidation state. Equations 2.25 and 2.26 two-step formalism represent the two-electron oxidation process. The oxidizing equivalents are holes in the silicon valence band. The upper character H^+ represents a proton in these equations, and the lower case h^+ represents a valence band hole.

$$\mathrm{Si} + 2\mathrm{F}^- + 2\mathrm{h}^+ \rightarrow [\mathrm{SiF}_2] \quad \text{(Electrochemical step)} \tag{2.25}$$

$$[\mathrm{SiF}_2] + 4\mathrm{F}^- + 2\mathrm{H}^+ \rightarrow \mathrm{SiF}_6^{2-} + \mathrm{H}_2 \quad \text{(Chemical step)} \tag{2.26}$$

$$\mathrm{Si} + 6\mathrm{F}^- + 2\mathrm{h}^+ \rightarrow \mathrm{SiF}_6^{2-} + \mathrm{H}_2 \quad \text{(Net)} \tag{2.27}$$

At lower applied potentials, the two-electron process of equation 2.27 prevails and is the primary half-reaction in creating porous silicon. This regime is represented by the area of the current density-potential plot in figure 8(a). Focusing on the first peak in figure 8(a), the current exhibits exponential growth with increasing potential from Open Circuit Potential (OCP). However, at higher overpotentials, the exponential relationship with potential ceases, giving way to a distinct peak, after which the current stabilizes at a relatively constant value. Upon examining the surface of the samples anodized at various potentials within this range, it becomes evident that porous silicon formation occurs (region I in 8(a)) within the exponential region, but not beyond the potential corresponding to the peak.

The potential corresponding to the maximum slope of the $i - V$ curve represents the upper limit for forming a uniform PSi layer. Within the range of potentials between the maximum slope and the current peak, it is still possible for a porous layer to form, albeit with non-uniform surface coverage. Electropolishing, on the other hand, occurs at potentials beyond the current peak (region III in 8(a)).

Visible hydrogen evolution occurs in the exponential region of the $i - V$ curve. However, as the potential approaches the current peak, the rate of hydrogen evolution significantly decreases until it ceases above the current peak. The dissolution valence transitions from approximately 2 in the exponential region to nearly 4 in the electropolishing region. The valence of 2 in the exponential region is attributed to the chemical reaction responsible for hydrogen evolution.

Figure 8 – (a) Typical anodic current density versus applied potential curve for electrochemical etch of silicon in an HF electrolyte. 2-electron and 4-electron oxidation reactions are illustrated. The data for this curve relate to a moderately doped p-type silicon wafer in 1% HF solution. Adapted with permission from (SAILOR, 2012). (b) formation condition for porous silicon; peak current density in solid line, maximum slope current density in dashed line.

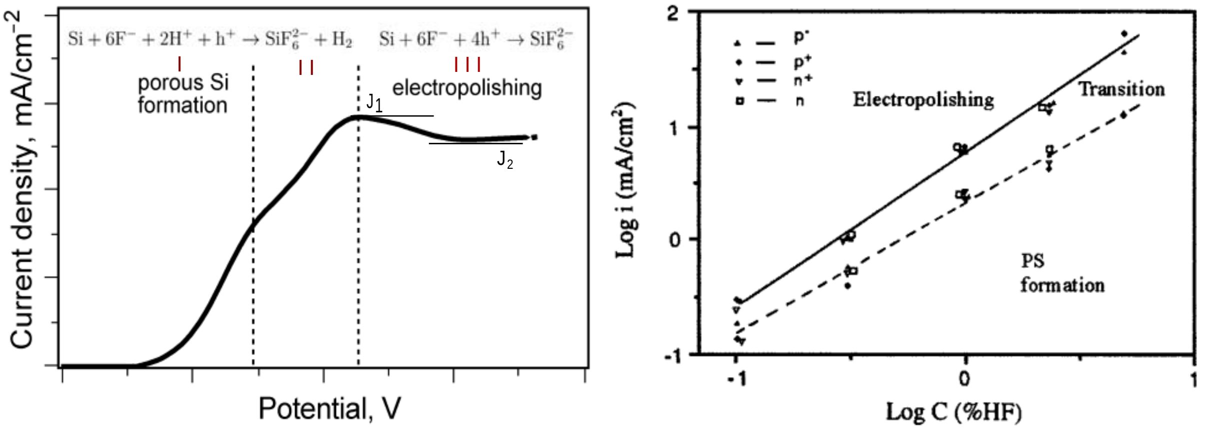

(a) (b)

Source: Taken from (ZHANG, 2003).

As the $i - V$ curve reveals, factors such as HF concentration, doping type, and doping concentration influence the relationship between the anode current and potential. The anodic behavior of both p-type and n-type materials demonstrates similarity when the rate of carrier transfer between the surface and the semiconductor bulk is sufficiently rapid. In cases where the current is not limited by the availability of holes in the semiconductor, the $i - V$ curves for these two materials exhibit significant similarity, except for a shift along the potential axis due to variations in doping levels. Notably, in the case of n-Si, substantial currents can be attained through intense illumination or degenerate doping. Therefore, the reaction processes that remain consistent across all silicon types are primarily governed by the chemical nature of the silicon material and the electrolyte, independent of the electronic properties of silicon. Different doping conditions impact the rate of charge transfer between the surface and the semiconductor, while the chemical nature of the reactions remains unaffected.

The occurrence of PSi production can be determined by examining the current at the maximum slope and the peak current derived from $i - V$ curves, as depicted in Figure 8(b) and Equation 2.28. This illustration serves as a visual representation of the criterion for PSi formation, showcasing the relationship between these current parameters and HF concentration across different types of silicon. Remarkably, the analysis reveals that the three regions characterized by current density and HF concentration remain largely unaffected by the type and concentration of silicon substrate doping. This finding emphasizes that the variations in semiconducting properties among the silicon samples have minimal influence on the likelihood of PSi formation. Ultimately, the propensity for PSi formation emerges as an inherent characteristic intrinsic to the semiconductor/electrolyte interface (ZHANG, 2003).

The current flow can go through five distinct physical phases, each characterized by a unique current conduction mechanism, as depicted in Figure 9(a). These phases include the substratum (Si), space-charge layer (s), Helmholtz layer (H), surface oxide coating (ox), and electrolyte (el). These components together contribute to the overall potential dips experienced along the current path, signifying the complete change in applied potential resulting from variations in current density. Also, silicon material and potential range affect how the applied potential is distributed in these several phases (ZHANG, 2003). The distribution of the applied potential in these phases of the current path depends on the current density (see Figure 9(a)), potential, doping type and concentration, HF concentration, illumination intensity, and direction. In particular, certain phases experience significant shifts in the applied potential, leading to alterations in the current distribution along the pore bottoms. Consequently, these changes in current distribution profoundly influence the morphology of PSi.

$$\Delta V_{app} = \Delta V_{Si} + \Delta V_s + \Delta V_H + \Delta V_{ox} + \Delta V_{el} \tag{2.28}$$

For p-Si and heavily doped n-Si materials, the potential distribution is divided between the Helmholtz layer and/or the space-charge layer. In the case of heavily doped materials, the surface degenerates, making the material behaves like a metal electrode. Consequently, the charge-transfer reaction within the Helmholtz double layer becomes the rate-determining step, resulting in the majority of potential drops occurring in the Helmholtz layer. Figure 9(b) illustrates each of these possible processes: for example, the anodic reaction processes on n-Si in the dark are constrained by the minority hole transport within the bulk of silicon, represented as r_2. On the other hand, for p-Si and illuminated n-Si in fluoride solutions at potentials negative of the first current peak, J_1, the reaction rate is influenced by the charge-transfer process across the electrode/electrolyte interface, indicated as r_4 and r_5. Moving to potentials positive of J_1, the electropolishing region, the rate-determining step shifts to the dissolution of the anodic oxide film, denoted as r_{10} (ZHANG, 2003).

It is worth noting that the dissolution of the oxide film formed at low fluoride concentrations is predominantly kinetically controlled (r_{10}), while at high fluoride concentrations, the process becomes mainly diffusion-controlled ($r_1 1$). Interestingly, a critical concentration exists, contingent upon pH, convection, and potential, where the contributions from kinetic and diffusion processes become equal. This delicate balance governs the overall behavior of the system (ZHANG, 2003).

Figure 9 – (a) Potential drops across a pore when current passes. (b) Schematic diagram of the charge transport in the Si/HF electrolyte interface region. r_1 and r_2 represents the majority and minority carrier transport; r_3 is the transport of holes to the surface; r_4 is the charge-transfer across the Helmhotz layer; r_5 is the electron injection; r_6 is the chemical dissolution; r_7 is the oxide formation; r_8 is the ionic transport in oxide; r_9 is the injection of oxidants; r_{10} is the dissolution of oxide and r_{11} represents the mass transport in electrolyte.

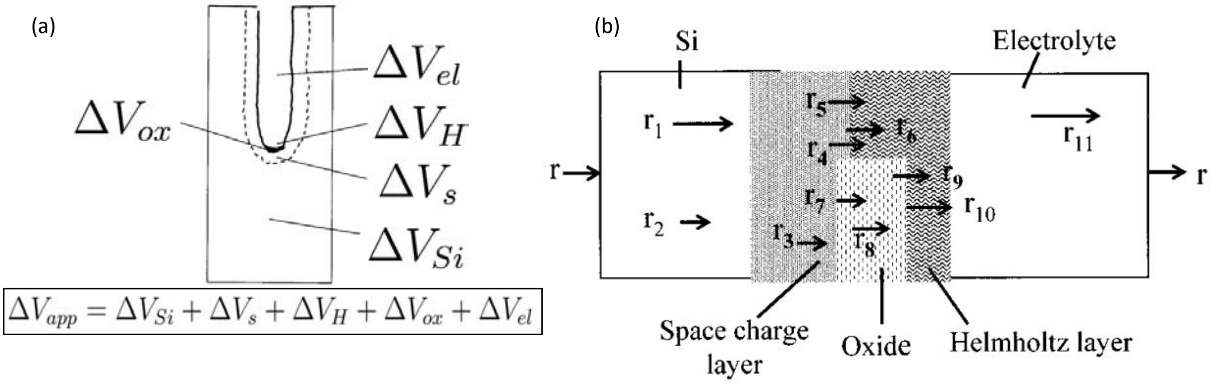

Source: Adapted from (ZHANG, 2003).

A small number of electrons flow when a metal contact is made with a silicon wafer (semiconductor), in order to equilibrate their work functions. If the work functions of the metals align appropriately, a fixed charge accumulates at the interface, creating an interfacial barrier that hinders the transport of additional electrons. This barrier (commonly referred to as a Schottky barrier) exhibits asymmetry due to differences in dielectric constants and density of states between the materials, resulting in the distinctive unidirectional or rectifying electron transport behavior commonly observed in diodes (SAILOR, 2012).

When a silicon electrode is submerged in an electrolyte, a similar phenomenon to Schottky barrier formation arises. The exchange of charges between these two phases gives rise to a barrier that can either obstruct or facilitate current flow, contingent on the direction of the current. To illustrate this effect, the energy band diagrams in Figure 10(a) depict the situation before and after immersing p-type silicon electrodes into the electrolyte. This barrier manifests as a bending of the conduction and valence bands near the interface.

Figure 10 – (a) Charge balancing for a p-type semiconductor at the semiconductor/electrolyte interface. (b) Charge transport processes at the interface of a p-type semiconductor and an electrolyte involve an increase in hole current during forward bias conditions. (c) Under reverse bias conditions for a p-type semiconductor, charge transport across the semiconductor/electrolyte interface is inhibited or blocked.

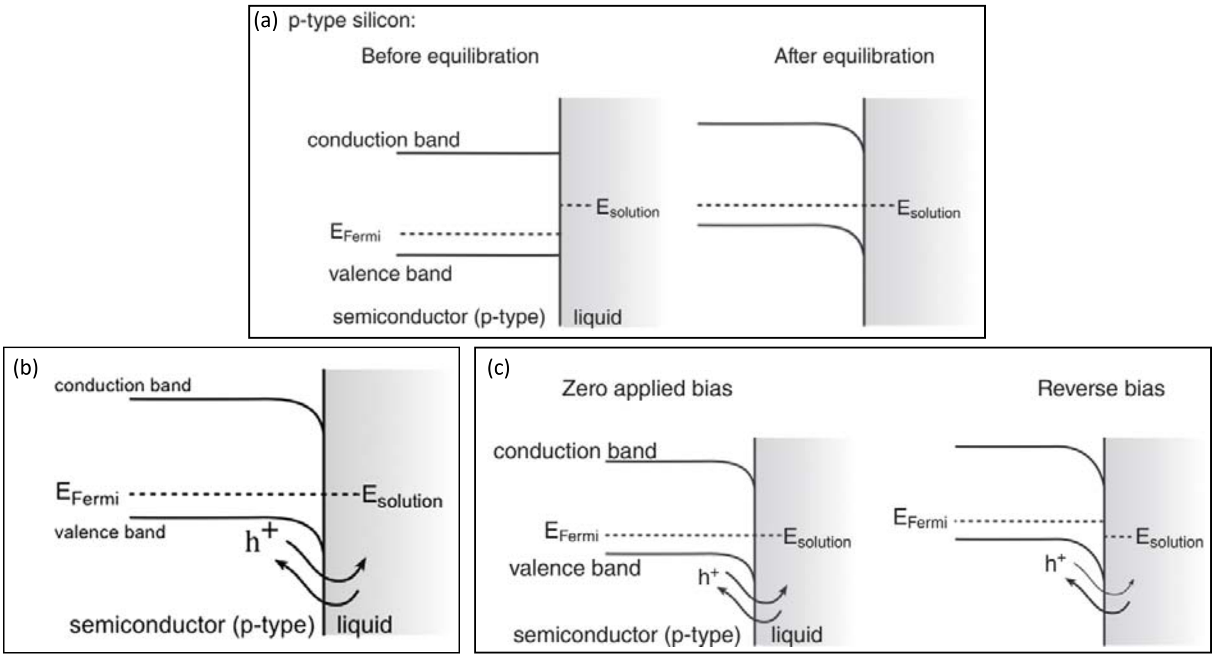

Source: Adapted from (SAILOR, 2012).

In the energy band diagrams, holes exhibit an energetically favorable behavior of moving upwards along the band lines due to their positive charge, while electrons follow similar principles but in opposite directions. The direction of current flow is determined by the interplay of these charge carriers' movement, leading to either a blocked or allowed current path across the electrode-electrolyte interface. These energy band diagrams provide valuable insights into the electrochemical behavior of silicon electrodes in electrolytic environments, which is crucial for designing and optimizing various electrochemical devices and processes (SAILOR, 2012).

Valence band holes play a crucial role as charge carriers that contribute to electrode corrosion. In a p-type silicon sample, these holes represent the majority of carriers. When no external bias is applied, the rate of hole transport in either direction across the interface remains relatively low, as depicted in Figure 10(b). However, when a positive bias is applied to the silicon electrode, the barrier to interfacial charge transport is reduced, leading to the accumulation of valence band holes at the interface. This situation is referred to as the diode being in forward bias. The accumulated holes actively participate in the corrosion reactions described by Equation 2.27, resulting in the formation of porous silicon (SAILOR, 2012).

When the potential of the silicon electrode is adjusted to be negative compared to the solution potential, the diode enters reverse bias mode. This scenario, illustrated in Figure 10(c), gives rise to an increased barrier to hole transport towards the interface, effectively halting the corrosion reaction (SAILOR, 2012).

Various parameters, such as electrolyte composition, dopant type and concentration, applied voltage, temperature, and light intensity, collectively influence the process of PSi formation. In any given experiment, multiple competing mechanisms can be at play, making the overall phenomenon intricate and challenging (SAILOR, 2012). For example, the least quantifiable aspect of a material is morphology, which is determined by the distribution of matter in space. It is thus very difficult to systematically characterize the morphology of PSi, which has extremely rich details with respect to the range of variations in pore size, shape, orientation, branching, interconnection, and distribution. Specifically, the size of pores depends on the doping type and concentration and is governed by a complex interplay of physical and chemical factors (BOMCHIL; HALIMAOUI; HERINO, 1990). Typically, for p-Si, the pore size increases with higher doping concentration, whereas for n-Si, it decreases with increasing doping concentration (ZHANG, 2003).

According to the International Union of Pure and Applied Chemistry (IUPAC) recommendations "Recommendations for the characterization of porous solids" (ROUQUEROL et al., 1994), porous materials contain voids, cavities, channels, or interstices, which are deeper than they are wide and less dense than constituent materials. The level of porosity is given by the ratio of the total pore volume to the apparent volume. Also, we can define three different pore size regimes:

Micropores have widths smaller than 2 nm. **Mesopores** have widths between 2 and 50 nm. **Macropores** have widths larger than 50 nm. In general, macro-, meso- and microporous materials are considered "nanoporous" because the pore sizes are less than 100 nm.

2.3 SERS Applications: Glyphosate

As we studied before, SERS is essentially an agglomeration of two techniques: Raman spectroscopy and nanotechnology. Several scientific research highlights its possible applications due to the potential of SERS as a detection technique. The earliest record of pesticide detection using SERS was performed in 1987 by Alak and Vo-Dinh (ALAK; VO-DINH, 1987). Hence, the first segment covers glyphosate (GLP) chemical and toxical properties, physicochemical characteristics, and action mode in the soil, environment, animals, and humans with their effects. Furthermore, the advantages and limitations of the principal measurement methods for GLP detection will discuss; with the recent advances in substrate development and its several aspects (such as sensitivity, reproducibility, selectivity, and portability), herbicide detection has improved.

Each year, millions of tons of pesticides are generated for use in agricultural (STORCK; KARPOUZAS; MARTIN-LAURENT, 2017). Because of the high demand, there is a toxicological risk that significantly impacts human health (KIM; KABIR; JAHAN, 2017; IARC, 2015; WHO, 2020), and ecosystems (STEINGRÍMSDÓTTIR; PETERSEN; FANTKE, 2018). The most common way to apply pesticides is by spraying them directly onto the plants or the ground. Consequently, they can also enter other environmental compartments like the atmosphere, the surface, and underground waters, where they can be taken up by aquatic and terrestrial biota such as birds, fish, and mammals (RUIZ-SUÁREZ et al., 2015; ERNST et al., 2018) as well as the surface and underground waters (RASMUSSEN et al., 2015; ZHEN et al., 2018). Currently, it is challenging to minimize the use of pesticides and to put mitigation methods in place (STEINGRÍMSDÓTTIR; PETERSEN; FANTKE, 2018; ZHEN et al., 2018; ABDELHAMEED; EL-ZAWAHRY; EMAM, 2018). To ensure adherence to the legal limitations, it is crucial to quickly and continuously monitor pesticides and their metabolites (REYNOSO et al., 2019).

The most extensively used pesticide worldwide is glyphosate (GLP). This nonselective and broad-spectrum herbicide is challenging to detect in the environment due to a lack of public health policies. The use of GLP has rapidly increased since the advent of genetically modified GLP-resistant crops at the turn of the century. Until September 2000, Monsanto™ patented GLP as an herbicide and sold it under the brand name Roundup Original®. Furthermore, since then, the market has seen the release of numerous brand formulations, prompting Monsanto™ to introduce new product versions like Roundup WG®, Roundup ULTRA®, Roundup Transorb R®, and Roundup Original Mais®(LOUWAARS; MINDERHOUD, 2001; LIMA; BOËCHAT; GÜCKER, 2021; VALLE et al., 2019; RICHMOND, 2018).

According to the manufacturer, Roundup's formulation consists of isopropylamine salt and the surfactant polyoxyethylene amine (POEA). The POEA improves efficiency (TSUI; CHU, 2003) and enhances the uptake and translocation of the active ingredient in plants (BENBROOK, 2016). According to WHO (WHO, 1994), GLP is “toxicologically harmless” for humans, other mammals, birds, and the environment, because of its degradability by soil bacteria (ZHANG et al., 2015; NAPOLI et al., 2015). And also, due to the GLP’s buildup in the environment’s water supply, recent research has identified GLP as a potential carcinogen (PEREIRA et al., 2021; BARNOR; CATON; MILJKOVIC, 2023; BERRY, 2020).

2.3.1 Chemical Properties and Toxicity of Glyphosate

Glyphosate, also known as N-(phosphonomethyl) glycine ($C_3H_8NO_5P$), is an amphoteric molecule having a basic 2°-amino group in the center of the molecule with dibasic-phosphonic and monobasic-carboxylic acidic sites at the two ends (GANDHI et al., 2021). It contains a linear carbon chain with a weaker bond, as seen in Figure 11, which probably reduces GLP’s persistence in the environment. As opposed to the other 95% of herbicides, glyphosate (GLP) has no aromatic ring structures (NCBI, 2020).

Figure 11 – Chemical structure of GLP.

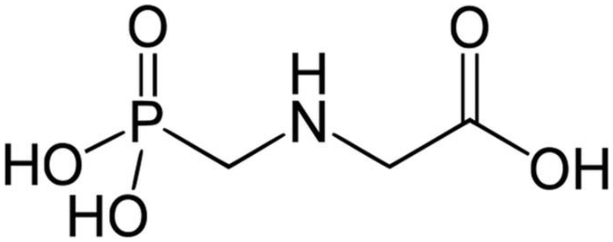

Source: The author.

In commercial uses, herbicides containing GLP are made in granular form using a combination of additives, inert chemicals, and surfactants, as well as salts soluble in liquid solutions. Although these formulations boost the herbicide’s water solubility and plant uptake, they also considerably increase its toxicity. As a result, GLP concentrations in commercial herbicides range from 0.96 to 94 w/w%. For instance, Roundup includes GLP ranging from 0.96 to 71 w/w% (GANDHI et al., 2021).

There are typically two forms of toxicity. When using a chemical spray, the risks of inhalation, skin contact, and oral contact refer to *acute toxicity*. *Chronic toxicity* is the risk brought on by consuming small amounts of substances continuously through diet (WALLACE; LINGENFELTER, 2019). For mammals, the acute toxicity of GLP LD_{50} (Lethal dosage, 50%) is approximately 5037 mg kg^{-1}. According to EPA registration, any herbicide with an LD_{50} greater than 5000 mg kg^{-1} will fall in Category IV, which has the least acute toxicity. Glyphosate’s LD_{50} levels are almost on the cusp of being classified as a Category IV chemical (KNISS, 2017).

The formulations of GLP play a significant role in its toxicity. According to experimental investigations, the toxicity of the POEA is more hazardous when used alone than GLP and its commercial version. Herbicides containing GLP ammonium also exhibit increased toxicity, with the poly[oxyethylene, oxypropylene]glycol block copolymer surfactant being more toxic than the solvent itself (SONG et al., 2012). In addition, when comparing GLP and the commercial mixture, the experiments show that POEA caused more DNA damage (GUILHERME et al., 2012).

2.3.2 Physicochemical interaction of Glyphosate with the environment and its effects

Pesticides are typically the most frequent toxins found in soil, where factors such as climate, physical, biological, and chemical interactions affect how long they last and how quickly they degrade (SARKAR et al., 2020). Depending on their chemical characteristics and how they interact with the environment, pesticides may be leached, decomposed, or volatilized, or they may remain sorbed (MUNIRA et al., 2016) or absorbed in the soil (AL-RAJAB; AMELLAL; SCHIAVON, 2008; ENFIELD; YATES, 1990).

High water solubility and low volatility molecules primarily carry in the soil by leaching processes. These molecules are transported by water flow, either through the soil profile and into the water table or by surface runoff and into the surface waters (BOUCHARD; ENFIELD; PIWONI, 1989). Consequently, there are significant differences in GLP concentrations and temporal dynamics between different water bodies. The volume and frequency of GLP applications to crops, precipitation events that create runoff, and the direction of water flow are all factors that affect GLP contamination (Figure 12) (GERECKE et al., 2002).

For human health, chronic exposure to GLP is linked to several risks, affecting endocrine function disruption, pregnancy problems, cancers, etc. (NOVOTNY, 2022; BERRY, 2020; BRUGGEN et al., 2018; TORRETTA et al., 2018; GASNIER et al., 2009; SAMSEL; SENEFF, 2013; PAGANELLI et al., 2010; CATTANI et al., 2014; THONGPRAKAISANG et al., 2013; GUI et al., 2012; BENACHOUR; SéRALINI, 2009; POLETTA et al., 2009; MARC; MULNER-LORILLON; BELLé, 2004; SLAGER et al., 2010; SHEHATA et al., 2013).

In plants, their leaves can absorb GLP, acting on several enzyme complexes and inhibiting the synthesis of specific amino acids (AMRHEIN; HC et al., 1980). It advises applying 5 l ha^{-1} of commercial formulations such as Roundup Original®, diluted to 44.5% before usage (LIMA; BOËCHAT; GÜCKER, 2021). They include GLP molecule's isopropyl ammonium salt, a polar solid with a high water solubility (12 g L^{-1} at 25 °C). And also present a low solubility in organic solvents and a melting point of 200 °C. Even

Figure 12 – Transportation procedures, movement via aquatic food webs, and GLP contamination of soil.

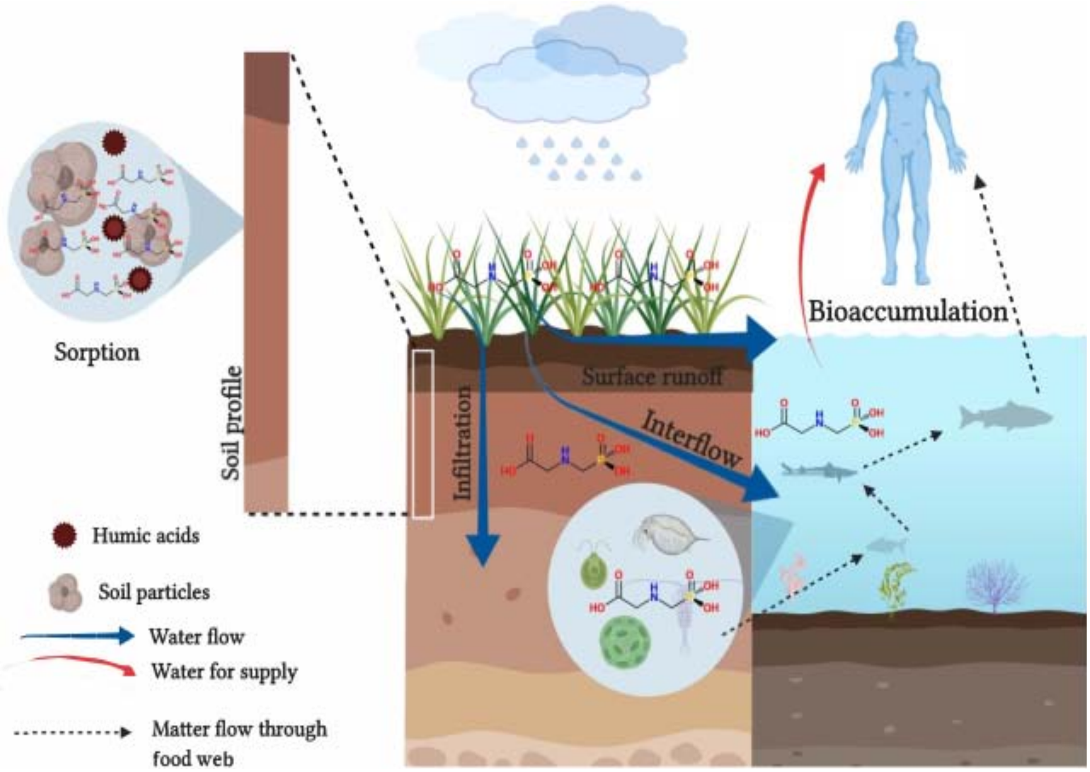

Source: Taken from (LIMA; BOËCHAT; GÜCKER, 2021).

at temperatures exceeding 60 °C, it does not deteriorate in visible light and has a density of 0.5 g cm^{-3} (AMARANTE et al., 2002).

GLP reacts with humic acids and metals when interacting with the soil, sticking to soil particles and remaining there for 4 to 835 days (EBERBACH, 1998; LIMA; BOËCHAT; GÜCKER, 2021). Also, GLP exhibits sorption with soil colloids (HERMANSEN et al., 2020). It can be detected in surface soil up to 10.6 g kg^{-1} (9.48% recovery of the applied dose) after more than four months have passed since GLP application, with much more significant quantities of AMPA (CASTRO, 2012). In addition, due to leaching during rain events that results in high concentrations in rivers (JONGE et al., 2001), it can become a potential source of contamination if it remains in the soil for an extended length of time—the residue-bound GLP molecule leach (COUPE et al., 2012). According to this, poor herbicide management by farmers and rural employees, who frequently inappropriately dispose of packaging and clean spray equipment in nearby bodies of water, results in variable point-source contamination in agricultural areas (GLOZIER et al., 2012; LIMA; BOËCHAT; GÜCKER, 2021).

The physicochemical activity of GLP includes microbial breakdown. It is the primary method of GLP mineralization after entering the environment. The enzyme GLP oxidoreductase is used in the metabolism of GLP by microorganisms from several taxonomic groupings. The primary breakdown products of GLP produced by this enzymatic route are AMPA and glyoxylate, as shown in figure 13 (JACOB et al., 1988). Although some Pseudomonas bacteria can utilize AMPA as a source of phosphorus, AMPA is typically not digested and secreted into the environment, which causes secondary pollution (QUINN; PEDEN; DICK, 1989). Other species may take up AMPA or degrade by the C-P lyase (Figure 13). In addition, this process produces inorganic phosphorus (Pi), which can contribute to eutrophication and volatile methylamine.

Figure 13 – Microbiological breakdown of GLP and AMPA in the environment. The glyphosate oxidoreductase metabolic pathway produces AMPA and glyoxylate (1), and the mineralization of AMPA by C-P lyase generates inorganic phosphorus and volatile methylamine (2).

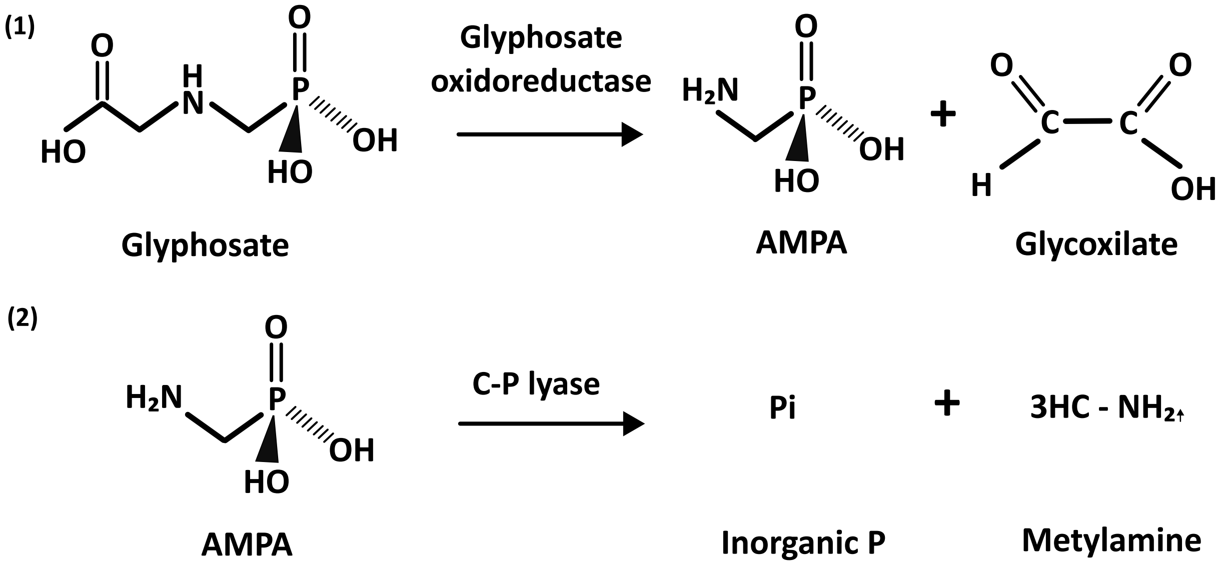

Source: Taken from (LIMA; BOËCHAT; GÜCKER, 2021).

Microbiological activity is necessary for GLP in polluted water and soil degradation. Therefore, it is possible to use microorganisms that can degrade GLP to convert this pesticide and its residues into less hazardous compounds. But experiments conducted in situ and in vitro have not yet achieved a suitable degradation efficiency (ZHAN et al., 2018). Because of this, it is necessary to develop other techniques and methods to detect it. However, GLP detection and quantification are expensive, and time-consuming (VALLE et al., 2019). Consequently, governmental control measures are unsuccessful since GLP cannot be detected by methods examining several types of chemicals and their metabolites in the same test in a unique multi-residue method. Thus, the impact of this information gap on the public economy and health care remains to be discovered. The "Glyphosate paradox" is introduced, which states that despite being the most frequently used agrochemical in the world, GLP is also the most difficult to analyze.

There is no ongoing monitoring of GLP or systematic information concerning environmentally polluted locations worldwide. For example, the European Union (EU) authorities examined 186,852 samples of cereal for pesticide residues in 2009 (POULSEN; CHRISTENSEN; HERRMANN, 2009). However, they only reached 462 sites across five countries, and 42 of those samples had positive results. Since 2010, EU regulators have conducted routine GLP monitoring in cereals. Nevertheless, testing for GLP residues on imported genetically modified soybeans—of which Brazil is one of the world's largest producers and uses GLP indiscriminately—remains challenging. Due to this information gap, it is more difficult to determine how much GLP people expose to daily and how governments could safeguard public health and the environment from its harmful consequences.

At this point, the European Community is more concerned with using the precautionary principle than many other nations. For instance, the maximum residue limit (MRL) for GLP in soybean was set at 20 mg kg^{-1} by the Codex Alimentarius Commission and the US Environmental Protection Agency (EPA) and 10 mg kg^{-1} by the National Health Surveillance Agency (ANVISA) in Brazil as a most preventative measure (BOMBARDI, 2017; MORAES, 2019).

Therefore, it is necessary to test GLP in a range of concentrations, emphasizing how it interacts with soil complexity under various situations, to comprehend and anticipate the movement of GLP in soils. On the other hand, GLP detection in various media was carried out using sophisticated analytical techniques. Some of them include: Liquid chromatography (LC) or high-performance liquid chromatography (HPLC) (PIRES et al., 2020; WINFIELD, 1990; PATSIAS; PAPADOPOULOU; PAPADOPOULOU-MOURKIDOU, 2001; HOGENDOORN et al., 1999; KHROLENKO; WIECZOREK, 2005; MERáS; DíAZ; FRANCO, 2005); Gas chromatography (GC) (HU; CHEN; LI, 2008; KUDZIN et al., 2002; KUDZIN et al., 2003; TSENG et al., 2004; DING et al., 2015; PEI; LAI, 2004; JI-YE et al., 2007); Ion chromatography (IC) (ZELENKOVA; VINOKUROVA, 2008; ZHU et al., 1999); Amperometric sensors (KHENIFI et al., 2009; PRASAD; JAUHARI; TIWARI, 2014),Voltammetric Electronic Tongue (VET) (BATALLER et al., 2012; GIL et al., 2013; PINTADO et al., 2012; HABEKOST, 2015). GLP has been recognized using two different types of the enzyme-linked immunosorbent assay (ELISA) (RUBIO et al., 2003; CLEGG; STEPHENSON; HALL, 2001; SANCHíS et al., 2012; GONZáLEZ-MARTíNEZ et al., 2005; VALLE et al., 2019; NOORI; MORTENSEN; GETO, 2020). Despite the popularity of several electrochemical sensors, their reproducibility and dependability in real-time detection without controlled complex environments are still being determined.

For GLP residue detection, research highlights the spectroscopy measures as the primary instrumental methods (ANSARI; HATAMI; KHAVIDAK, 2019; WAIMAN et al., 2012; DICKSON et al., 1988; CARTIGNY et al., 2004; VALLE et al., 2019). Other spectroscopy techniques includes the SPR (BALCIUNAS et al., 2022; NAFISAH et al., 2019; VRÁBLOVÁ et al., 2022; DO et al., 2020; FREIRE et al., 2019; NAFISAH et al., 2022) and SERS (MA et al., 2021; BUTMEE; SAMPHAO; TUMCHARERN, 2022; EMONDS-ALT et al., 2022; BALAJI et al., 2022; LÓPEZ-CASTAÑOS et al., 2020; VALLE et al., 2019; TORUL; BOYACI; TAMER, 2010).

2.3.3 Development of a SERS substrate for Glyphosate detection

The speed for examining samples is one of the critical benefits of employing SERS over conventional analytical techniques for identifying pesticides in simple matrices (such as water or organic solvents). A microliter sample can apply to a SERS substrate, followed by a split-second laser integration time to produce a SERS signal, which can then compare to a reference spectrum. Sensitivity, repeatability, selectivity, and portability are further crucial factors. These elements have improved over time and are influenced mainly by the creation of SERS substrates.

Sensitivity

Perhaps the most extensively researched feature of a SERS study for the sensitive detection of pesticides is the limit of detection (LOD). The reported LODs of SERS for pesticide detection in simple matrices (such as organic solvents or water) are influenced mainly by the molecular makeup of the pesticide and the type of substrate. Another crucial point to keep in mind is that the maximum residue levels (MRLs) permitted in agricultural produce and the environment, which regulatory organizations like the EPA set, cannot be directly compared to the LODs for pesticide detection, which typically reported in the parts-per-million (ppm) or parts-per-billion (ppb) level. Often, the LOD for a pesticide is based on the concentration of that pesticide in its solvent, whereas the MRL for a particular pesticide is based on the sample matrix it is present. Therefore, it is imperative to carefully transition between the units and describe how the LOD of the analytical method and the legal criterion for pesticide detection relate to one another (PANG; YANG; HE, 2016).

From the viewpoint of the substrate, the differences in “hot spots” on substrates can be significantly responsible for the variance in sensitivity of SERS detection (ZHAO et al., 2008). Through the logical design of the SERS substrate and the experiment, the LOD of SERS methods can reach a single-molecule detection level (KNEIPP et al., 1997; LIU et al., 2011; ZRIMSEK; WONG; DUYNE, 2016; RU; ETCHEGOIN, 2012).

From the perspective of the pesticide, each pesticide’s SERS sensitivity varies, primarily due to the distinctive, intrinsic vibration of the molecules, the interaction between the molecules of the pesticide and the substrate, and the compatibility of the pesticides when complex with the substrate. Molecules with a conjugated double bond system and symmetric vibrational modes are more active than others for intrinsic vibration. Consequently, certain pesticides, like malachite green and crystal violet, are more frequently used as pesticide targets for assessing a SERS substrate (LEE et al., 2007; PAN et al., 2015). Additionally, pesticides with specific functional groups (e.g., thiol, amine) that have a great affinity for Au and Ag substrates make excellent targets (ZHENG et al., 2013; GUO et al., 2015; KIM; BARCELO; LI, 2014; NGUYEN et al., 2014; MUJAWAR et al., 2014). These two characteristics are inherent to many pesticides, making them attractive targets for sensitive SERS investigation.

Reproducibility

One of the significant issues in SERS research is data reproducibility, especially concerning peak intensities, despite SERS being an ultrasensitive detection method. Thus, quantitative investigations continue to be challenging in SERS, not just in pesticide detection but also in other SERS applications. The substrates and sample preparation that create and regulate the hot spots are the primary causes of the variation. In addition, the aggregation of the typical colloid SERS substrates significantly impacts the hot spots.

Despite widespread commercial availability and relative affordability, they frequently struggle to regulate aggregation, leading to more significant signal variance than well-ordered nanostructures. As a result, partial blindness cannot be used in selecting the detection sites. Instead, we can choose certain substrate regions to minimize variation using a Raman microscope. For example, as their hot spots are not influenced by aggregation, core-shell-based colloid nanoparticles have greatly enhanced the signal variation of SERS (LI et al., 2010). Incorporating colloids into a sol-gel (KEATING et al., 2012; LEE; DAI; YOUNG, 1997) and integrating with a microfluidic device (LEE et al., 2007; LEE et al., 2006) are other research that has demonstrated how to manage the homogeneity of nanoparticles into dependable patterns.

Selectivity and Portability

The selectivity of SERS to concurrently detect each of the individual pesticides in a mixture is a significant difficulty, even if the matrix is only water or an organic solvent. SERS experiments, however, have only been able to consistently detect fewer than five pesticides at once (HOU; PANG; HE, 2015; PANG; LABUZA; HE, 2014). That detection is probably because several analytes compete for adsorption to the SERS substrates. So, the target compound concentration ratios in the sample matrix would not be proportionate to the SERS peak intensities produced. It is because the target compounds with higher binding affinity to the substrate will have more surface coverage adsorption on the substrates.

Due to the existence of another substance with a molecule with several orders of magnitude more affinity to the substrate, the pesticides may occasionally not even produce a meaningful peak. This issue can be resolved by pre-separating individual pesticides or pre-treating a smaller number of pesticides for a single SERS test. However, doing so would unavoidably lengthen the analytical process and add complexity (YAO et al., 2013; PANG; YANG; HE, 2016).

Compared to GC/LC-MS approaches, one of the most well-liked elements of SERS development is its strong chance of becoming a field detection technique. Field detection is crucial in pesticide applications for quick screening and monitoring of pesticides in the environment, agricultural production, and industrial processes. Therefore, a portable detecting system must be quick, light, simple, and compact. The development of handheld Raman spectrometers has led to miniaturization and commercialization, which has made portable SERS detection possible. However, creating appropriate substrates is equally as important as the instrument. Traditional colloidal-based substrates may need to perform better for portable applications due to the different processes required to deposit the nanoparticles on a solid surface and to concentrate/aggregate the substrate. Therefore, solid SERS substrates are more suited for detection that demands portability (GE; HU; LI, 2022; PANG; YANG; HE, 2016).

Another strategy is to create SERS sensors based on the paper (WEI; WHITE, 2013; LEE; TIAN; SINGAMANENI, 2010; QU et al., 2012), or fiber (STODDART; WHITE, 2009; YAP et al., 2012). One study, for instance, screen printed SERS active nanoparticles onto filter paper, allowing for the screening of several samples employing portable high throughput technology (QU et al., 2012). These substrates were not only reasonably priced, but they also demonstrated repeatable results with less than 10% spot-to-spot fluctuation. Another study created ordered arrays of homogenous clusters of AuNPs on an optical fiber using a template to guide self-assembly (YAP et al., 2012). These SERS-enabled optical fibers displayed excellent SERS performance, as shown by crystal violet testing. This batch technique strategy might open the door to affordable, effective SERS substrates. More investigation will be required to assess the substrates' stability and to apply it to a more extensive range of target analytes (PANG; YANG; HE, 2016).

3 DVD-R as a solid SERS-active platform

Since our interest is the fabrication of stable, low-cost, and reproducible SERS active substrates, this chapter will describe the materials, methods, results, and discussion of the manufacturing DVD-R as a solid SERS-active platform for Glyphosate (GLP) detection. Information about morphology, chemical and spectroscopy measurements, and the Cathodic Cage Plasma Deposition technique (CCPD) will be presented—additionally, three important parameter definitions for performance analysis of solid SERS-substrates.

3.1 Materials

To study the substrates SERS activities, we use the following probe molecules: Crystal Violet (CV) 1% ($C_{25}H_{30}N_3C_l$), a commercial non-selective herbicide GLP Roundup^{TM} (GLP-RU) 480 g/L (with GLP as the active ingredient) and the Standard GLP 100 mg/L ($C_3H_8NO_5P$), obtained by SpecSol Quimlab (Brazilian industry). In addition, DVD-R single-layer (4.7 GB) was obtained from commercially available fresh optical discs. All solutions were prepared with ultrapure water (18.2 MΩcm) produced by Sartorius Arium®Comfort Ultrapure Water Systems.

3.2 SERS substrate fabrication

Figure 14 depicts the DVD-R@AgNPs manufacturing process. As shown in Figure 14a, the standard DVD-R consists of two polycarbonate (PC) plates with a spiral distribution of rectangular-shaped grooves to fit in a sandwich way, with a photosensitive dye between them.

After immersing the DVD-R in boiling water for 3 minutes, the metallic reflective and PC layers separate with a tweezer. To remove the photosensitive dye from the surface of the PC layer with nanogrooves (see Figure 14b), wash down twice with isopropyl alcohol for 1 minute each time, then rinse three times with ultrapure water. The grating structure on the dried and clean PC surface has a holographic thin film appearance—the layer cutting into 1 cm^2 square pieces.

3.3 Cathodic Cage Plasma Deposition technique

In the late 1990s, active screen plasma nitriding (ASPN) was created based on post-discharge plasma theory and glow discharge (DC) plasma technology (LI; GEORGES; LI, 2002; LI, 2010; GEORGES, 2001). The cathodic potential in an active screen

Figure 14 – Schematic representation of the SERS substrate fabrication process: (a) structure of a standard DVD-R, (b) PC sheet with nanogrooves, (c) AgNPs deposited by CCPD method over the PC nanogrooves, and (d) direct Raman measurements.

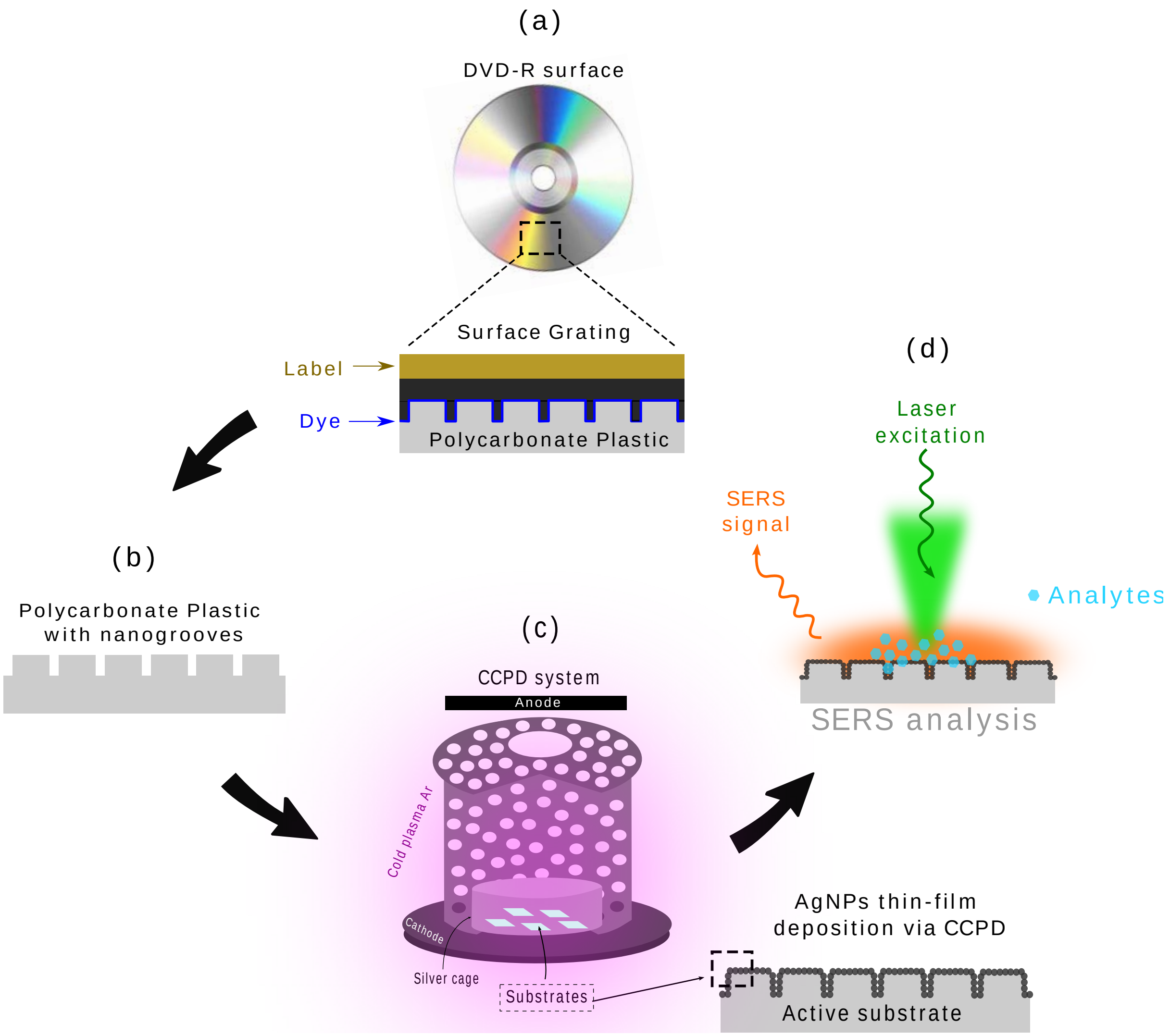

Source: The author.

(AS) plasma system applies to a metal screen that encloses the workload. The treated component is either in a floating potential or exposed to a shallow cathodic bias power. This electrical setup allows plasma to form on the metal screen surface rather than the component surface. The plasma heats the screen, and this heats the components to the proper temperature. Moreover, various ions, electrons, and other active species are present in the plasma for the nitriding process (LI, 2010).

Studies have demonstrated the remarkable capacity of ASPN to address a large of limitations present in conventional DC Plasma Nitriding (DCPN) (LI, 2010; GALLO; DONG, 2009; BELL; LI, 2007). Unlike DCPN, which demands fully electrically conductive parts, ASPN proves versatile and can treat a wider range of materials. Additionally, ASPN mitigates risks associated with arcing, surface damage, uneven nitriding caused by edge effects and temperature variations, and the hazard of overheating due to hollow cathode effects. Furthermore, ASPN offers a compelling solution to the challenges involved in treating substantial material quantities. As a result, the ASPN method shows great promise in fully harnessing the environmentally friendly plasma technology of thermochemical surface engineering (BELL; LI, 2007).

About 20 years ago, another technique was created from the ASPN to reduce the edge effect completely, called Cathodic Cage Plasma Nitriding (CCPN) (LI; GEORGES; LI, 2002; ALVES et al., 2006). It involves placing samples on either a floating or a cathodic potential and enclosing them in a metal/active screen (as in figure 15) at the cathodic potential (LI; BELL; DONG, 2002). After being set up on an isolant substrate and left in a floating potential, the samples are processed post-discharge. Since the plasma was produced on the cage rather than directly onto the samples in this technique, the edge effect was removed entirely. Radiation from the heated cage provides the heat required to maintain the treatment temperature. This technique's advantage is that it transforms the cathodic cage material on the sample into a compound once it reacts with the processing gasses. Due to its distinctiveness, this method is frequently employed for thermochemical diffusion, and alloying samples with cathodic cage material (NAEEM et al., 2017; NAEEM et al., 2020).

Figure 15 – Schematic representation of CCPD systems during a deposition process, where thermochemical diffusion and a glow-discharge plasma at a low temperature occurs.

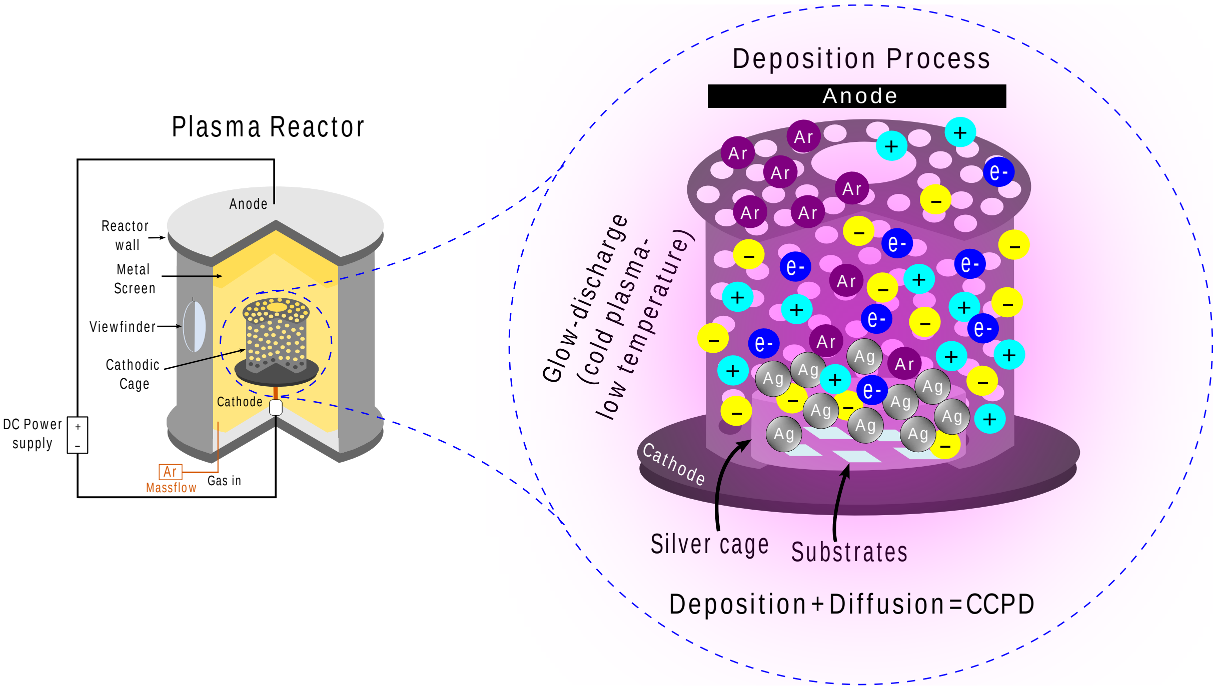

Source: The author.

Figure 16 – Three different angular pictures of PC substrate from DVD-R before the sputtering deposition.

Source: The author.

During the glow-discharge plasma, ions directly bombard the cathodic cage, and its material is sputtered and deposited on the sample's surface, as is shown in figure 15. As a result, any nitride can be deposited on materials, and this process is known as Cathodic Cage Plasma Deposition (CCPD) because of this (ABREU et al., 2022). Alves et al. introduce CCPD as a new innovative method for producing thin films to the scientific community (ALVES et al., 2006). The development and success of this technique are due to the provision of all the benefits of thin film growth obtained by conventional plasma. Compared to conventional plasma film growth, CCPD allows no risk of component damage due to arc opening, better penetration of compounds into inaccessible areas, and no edge effects. Furthermore, due to the simultaneous deposition and diffusion in CCPD, it expects good coating adherence over the substrate. Use is further encouraged by CCPD's high deposition efficiency, and low processing cost (LIBÓRIO et al., 2020).

A CCPD technique uses a fixed-diameter steel cylindrical cage for the SERS-active substrate manufacture. The cage and the sample holder were first polished by sandblasting for 30 minutes, then washed and dried with a drier. Next, a silver ring-shaped sputtering target with a diameter of 10.1 mm (99.9% purity) was put inside the cathodic cage. Figure 16 shows the PC substrates inside the target and cage before deposition. The employed reactor has a DC voltage source and a cylindrical vacuum chamber where the plasma generates in the cage (cathode) and the anode (chamber). The CCPD system has gas cylinders and mechanical and vacuum pumps as external components. These connect to sensors and process parameters controllers, such as voltage, gas input, and evacuation.

The experimental setup used in the deposition process was: (1) the samples were positioned on a steel sample holder. Then the cathodic cage and the silver ring target were placed outside the PC substrate above the sample holder. (2) Vacuum pump was turned on for one hour until it reached a stable pressure of $\sim 10^{-3}$ Torr. (3) A constant

Figure 17 – (a) The argon gas plasma during the deposition process and (b) PC substrate from DVD-R after the sputtering deposition.

Source: The author.

argon gas flow of 10 sccm is getting into the reactor. Finally, (4) sputtering deposition is performed over four hours at 80°C, a DC voltage of 600 V, an electric current of 0.05 A, and a working pressure of 2.70 mTorr.

During the CCPD process, the plasma forms on the cage surrounding its entire external surface, indicating that the atoms' sputtering occurs on the cage, which prevents the nanometric surface of the substrates from being damaged. In the single cathode process, due to the gas flow and the partial pressure difference between the chamber and the cathode cavity, the particles sprayed at the cathode are directed into the PC sample inside the silver target. As a result, the silver atoms extracted from the target can combine with the reactive gas in the plasma atmosphere, forming the aggregated AgNPs that settle on the sample's surface (see representative Figure 14(c)). Figure 17 shows the PC substrates with AgNPs thin film after deposition. These substrates are the SERS-active substrates called DVD-R@AgNPs.

The use of CCPD provided a layer with a high degree of uniformity. Improved compound penetration into inaccessible areas, with no edge effects or discontinuities, (LOPES et al., 2018; SOUSA et al., 2023; SOUSA et al., 2015b; SOUSA et al., 2015a; ALVES et al., 2006), inducing more porosity and roughness to the films, a helpful parameter for applying SERS.

All the SERS-active substrates are fabricated under the same conditions. Figure 14(d) shows the DVD-R@AgNPs used as SERS-active substrates to detect low-concentrations of the samples: CV, GLP, and GLP-RU. The samples were analyzed using the Raman spectroscopy technique. In this process, stock solutions of CV and GLPs were prepared in ultra-pure water.

3.4 Morphological and Chemical Characterization

Field Emission Gun Scanning Electron Microscopy (FEG-SEM) was used to examine the changes in the morphology of the substrate nanogrooves after nanoparticle deposition. In addition, the atomic composition of the DVD-R@AgNPs surface investigates using SEM with energy-dispersive X-ray spectroscopy (SEM-EDS). MIRA3 TESCAN field emission instrument from the Laboratório Associado de Sensores e Materiais (LABAS) of the Instituto Nacional de Pesquisas Espaciais (INPE) was used for FEG-SEM analysis with secondary electrons and accelerating voltages of 10 kV. Carl ZEISS MA 10 + EDX INCA instrument was used for SEM-EDS analysis, with secondary electrons and accelerating voltages of 20 kV.

3.5 Optical Measurements and quantitative analysis

A drop of 5 μL of each analyte solution was put on the DVD-R@AgNPs surface. The Raman signal of the DVD-R@AgNPs substrate is measured with Raman HORIBA LabRam HR Evolution Spectrometer with a 514.15 nm excitation laser and CCD camera, from the LABAS-INPE laboratory. The laser power of 2 mW was focused using a 20× objective lens with a numerical aperture (NA) of 0.40, typical for SERS measurements. The Raman spectra were collected between 400 and 1,800 cm^{-1}, with a 60-second exposure time and three accumulation numbers.

The SERS parameters, such as the limit of detection (LOD), the limit of quantification (LOQ), and the enhancement factor (EF), were calculated to evaluate the performance of the substrate DVD-R@AgNPs with all analytes. Following the International Union of Pure and Applied Chemistry (IUPAC) recommendation, LOD and LOQ were calculated by the following equation (CHEN et al., 2022),

$$LOD = \frac{3\sigma}{S}, \quad \text{and} \tag{3.1}$$

$$LOQ = \frac{10\sigma}{S}, \tag{3.2}$$

In this case, σ represents the standard deviation of the blank signal, and S denotes the sensitivity of the calibration curve slope, which is determined by $\frac{\Delta intensity}{\Delta concentration}$.

The EF was calculated by comparing the analyte's Raman spectra for the DVD-R@AgNPs active substrate with standard silicon (100) substrate. Using Crystal Violet (CV) as the reference powder sample, the conventional Raman spectrum obtained by silicon was performed under the same experimental conditions. EF was calculated through the following equation (RU et al., 2007; KOCHYLAS et al., 2021):

$$EF = \frac{I_{SERS}}{I_{RAMAN}} \times \frac{N_{RAMAN}}{N_{SERS}}, \tag{3.3}$$

where I_{SERS} is the intensity of a peak in the SERS spectrum and I_{RAMAN} is the same peak in the conventional Raman spectrum. N_{SERS} is the number of excited molecules within the area covered by the laser spot (ITOH et al., 2011), S_{spot}, during SERS measurements. N_{RAMAN} is the number of molecules contained in the volume V of the cylinder defined by the area S_{spot} and h is the depth of field penetration of laser into the CV sample. Thus, following reference (KOCHYLAS et al., 2021), the ratio N_{RAMAN}/N_{SERS} is reduced to 3.4.

$$\frac{N_{RAMAN}}{N_{SERS}} = \frac{\rho \cdot S_{film} \cdot h}{C \cdot V \cdot M_{CV}}, \tag{3.4}$$

where C is the molarity of the CV aqueous solution used in the SERS measurements, $V = 10\mu L$ is the volume of the drop cast on the SERS substrates, S_{film} =0.2 cm^2 is the area of the SERS substrates. M_{CV}=393.958 g/mol and ρ=1.19 g/cm^3 are CV's molar mass and density, respectively. The h was calculated through equation following the equation (N'GOM et al., 2008):

$$h = n\frac{\lambda}{(N.A.)^2}, \tag{3.5}$$

where n is the refractive index of the CV in powdered form, which is 1.60 (estimated) (GREEN, 1990) at 514.15 nm, $N.A.$=0.40 is the numerical aperture of the 20× objective lens used in the experiments, and λ=514.15 nm is the laser wavelength, giving the value of h=4.69 cm.

3.6 Results and Discussion

This section will focus on the results and discussions of Field Emission Gun Scanning Electron Microscopy (SEM-FEG) imaging and spectroscopy characterization. First, the grating pattern of DVD-R and the nanometric structure of the AgNPs will be shown. Next, the probe molecules' principal peak positions and SERS vibrational assignments will be described. Finally, for quantitative analysis of the SERS substrate, the low-concentrations detection of Crystal Violet (CV), standard (GLP), and Roundup^{TM} Glyphosate (GLP-RU), and the enhancement factor calculation for solid SERS-active substrate will be presented.

3.6.1 SEM characterization

Figure 18(a) displays SEM images of the uncoated polycarbonate (PC) grating structure. The gratings have regular periodic structures with broad lines of around 750 nm separated by grooves of about 200 nm. On the contrary, the pattern structure surface of PC with uniform coverage of the thin film layer AgNPs is in Figure 18(b). After the AgNPs CCPD process, the periodic PC structure remained unchanged, as shown in Figure 18(b). Furthermore, we can see in Figure 18(b) that the deposition expanded the width of the walls between the grooves by around 100 nm. As a result, the grooves' width shrunk, indicating that AgNPs had entered them. Additionally, the narrowing of the groove allows the local surface plasma's coupling strength and charge density to rise on its sidewalls (WANG et al., 2021; BOHREN; HUFFMAN; KAM, 1983; XU; KÄLL, 2006; LOMBARDI, 2017).

Figure 18 – SEM-FEG imaging of grating DVD-R: (a) without and (b) with the Ag thin film.

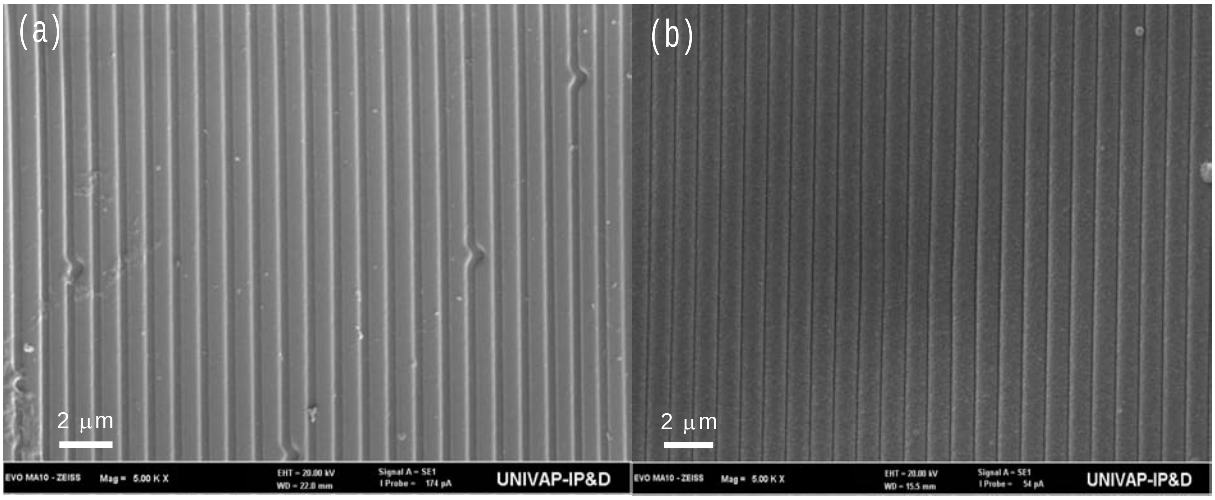

Source: The author.

The high-magnification SEM picture in Figure 19(a) reveals the region's regular distribution of the sphere forms. These aggregated AgNPs still have surface roughness on the substrate and a diameter between 52 and 68 nm. Because of the relationship between the size and wavelength of the incident radiation, the geometry of the AgNPs affects the plasmon band's absorption wavelength. Furthermore, the proximity of aggregated AgNPs found in the grooves and sidewalls allows the local surface plasma coupling strength and charge density to increase, which is crucial for SERS (WANG et al., 2021; LOMBARDI, 2017; GELLINI et al., 2008; KAPLAN et al., 2009; KAHL; VOGES, 2000).

The elemental EDS spectra of the DVD-R@AgNPs substrate are in Figure 19(b). Components that make up the DVD-R matrix, carbon, and oxygen, have peaks in the EDS spectra at 0.27 and 0.52, respectively. On the other hand, the silver nanoparticles on the matrix surface correlate with the peak at 3.00 keV. The thin gold film is associated with the peak at 2.15 keV and is required only for SEM measurement. The same scanned area's EDS semi-quantitative analysis verified that ∼16.03 ± 0.1 wt% of the substrate's composition relates to silver. Because silver is one of the metals most commonly employed for the "correct" optical qualities to sustain "excellent" resonances in the visible/near-infrared spectrum, the manufactured DVD-R-based sample comprises AgNPs that is intriguing from the perspective of SERS (RU; ETCHEGOIN, 2008; STAROWICZ et al., 2018; MAHMOUD; EL-SAYED, 2013; GOEL; SINGH; SINGH, 2014).

Figure 19 – SEM-FEG imaging of grating DVD-R coated by a silver thin film: (a) 125 kx magnification. (b) Energy dispersive analysis of the Ag thin film on PC surface region. The inset image shows the scanned size of the substrate.

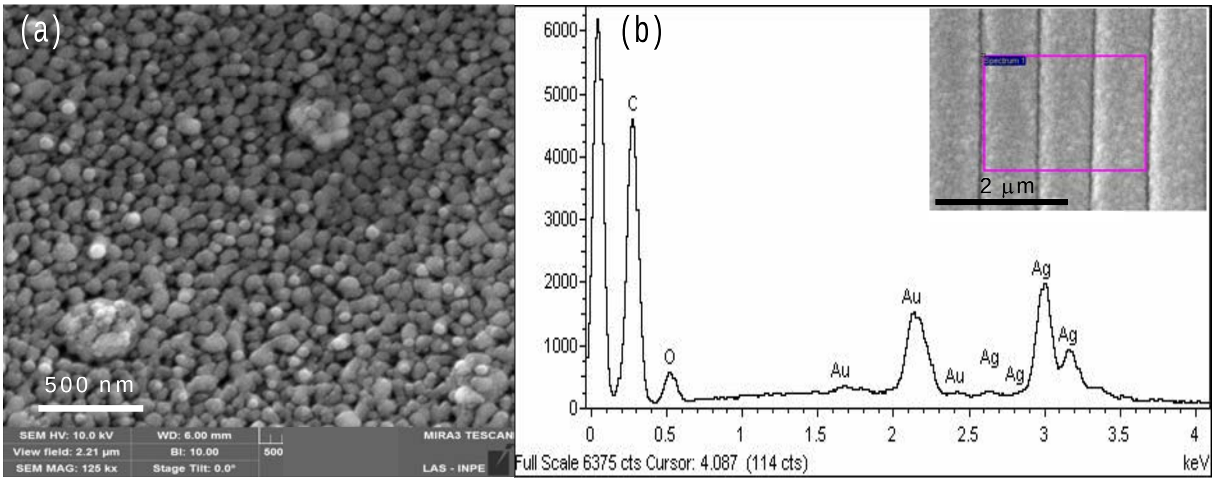

Source: The author.

3.6.2 Raman and SERS analysis

SERS activity of the DVD-R@AgNPs substrate is investigated through Raman signal detection. Figure 20(a) displays the DVD-R@AgNPs spectrum without any analytes. The typical SERS spectra of 0.1 mg/ml (100 ppm) GLP, 2.5 mg/ml (2,500 ppm) GLP-RU, and 1×10^{-4} mg/ml (0.1 ppm) CV revealed on the DVD-R@AgNP substrates are shown in Figures 20(b), 20(c), and 20(d), respectively. All spectra are subject to background adjustment and smooth lines. Generally, we can see that every recognized peak has a significantly increased intensity, revealing a Raman enhancement effect on the DVD-R@AgNPs surface.

The band at 1,589 cm^{-1} for CV (Figure 20(d)), 1,584 cm^{-1} for GLP-RU (Figure 20(c)), and 1,595 cm^{-1} for GLP (Figure 20(b)) can be associated with the peak at 1,595 cm^{-1} in Figure 20(a). This band is present in all the SERS analytes probe spectra. Thus we can think that it belongs to the substrate (blank).

The Raman signal enhancement, via DVD-R@AgNPs, occurs between the charge transfer (CT) and the resonance of the laser with surface plasmon resonance SPR (referred to as electromagnetic enhancement). Also, AgNPs enable a stronger electric-field concentration, and a better SERS signal improvement (ITOH et al., 2011; STAROWICZ et al., 2018; MAHMOUD; EL-SAYED, 2013).

The interaction of the analyte with the surface of metal nanoparticles and the substrate grating causes the Raman signals of specific modes to be significantly enhanced in SERS. As a result, complicated formation occurs between the metal framework and the analyte. The DVD-R@AgNPs substrate spectra still contain six distinct markers for the regular Raman bands of CV at 430 cm^{-1}, 806 cm^{-1}, 914 cm^{-1}, 1,179 cm^{-1}, 1,371 cm^{-1}, and 1,618 cm^{-1}, as shown in Figure 20(d). The literature (COLNIȚĂ et al., 2022) agrees with the other SERS peak positions of CV discovery, which are at $\sim$520 cm^{-1}, $\sim$576 cm^{-1}, $\sim$730 cm^{-1}, $\sim$761 cm^{-1}, $\sim$989 cm^{-1}, and $\sim$1,054 cm^{-1}.

Due to the molecular structure and propeller-like configuration (MOROVVATI; MALEKFAR, 2019), the Raman spectrum of CV-organic dye exhibits three distinct vibrational modes (FATEIXA; NOGUEIRA; TRINDADE, 2018), which include a core carbonium ion and three symmetric benzene rings. One vibrational mode is associated with the central carbon atom C^{+}-phenyl vibrations at wavenumbers up to 450 cm^{-1}. Another group is the nitrogen atoms N-phenyl stretching vibrations at wavenumbers between 1,350 and 1,400 cm^{-1}. And also, the skeletal ring/C-H deformations/ring stretching modes at wavenumbers 400-1,300 cm^{-1} and above 1,400 cm^{-1} (FATEIXA; NOGUEIRA; TRINDADE, 2018). Cañamares and Liu (CANAMARES et al., 2008; LIU et al., 2009) published the typical Raman spectra of CV molecules in a plastic substrate without any patterns or metallic coatings. Their spectra show strong bands at 1,372 cm^{-1} for the phenyl-N stretching and 1,615 cm^{-1} for the benzene stretch (FATEIXA; NOGUEIRA; TRINDADE, 2018).

Additionally, the Raman bands contributions for the C^{+}-phenyl bending at 437 cm^{-1} and the out-of-plane ring C–H bending mode at 800 cm^{-1}. The contributions from the CV and PC layers are at 911 cm^{-1}, the benzene ring is deformed/symmetric and

Figure 20 – SERS spectra of active substrate DVD-R@AgNPs (a) blank without analyte, (b) with 0.1 mg/mL GLP, (c) with 2.5 mg/mL GLP-RU, and (d) with 1×10^{-4} mg/mL CV.

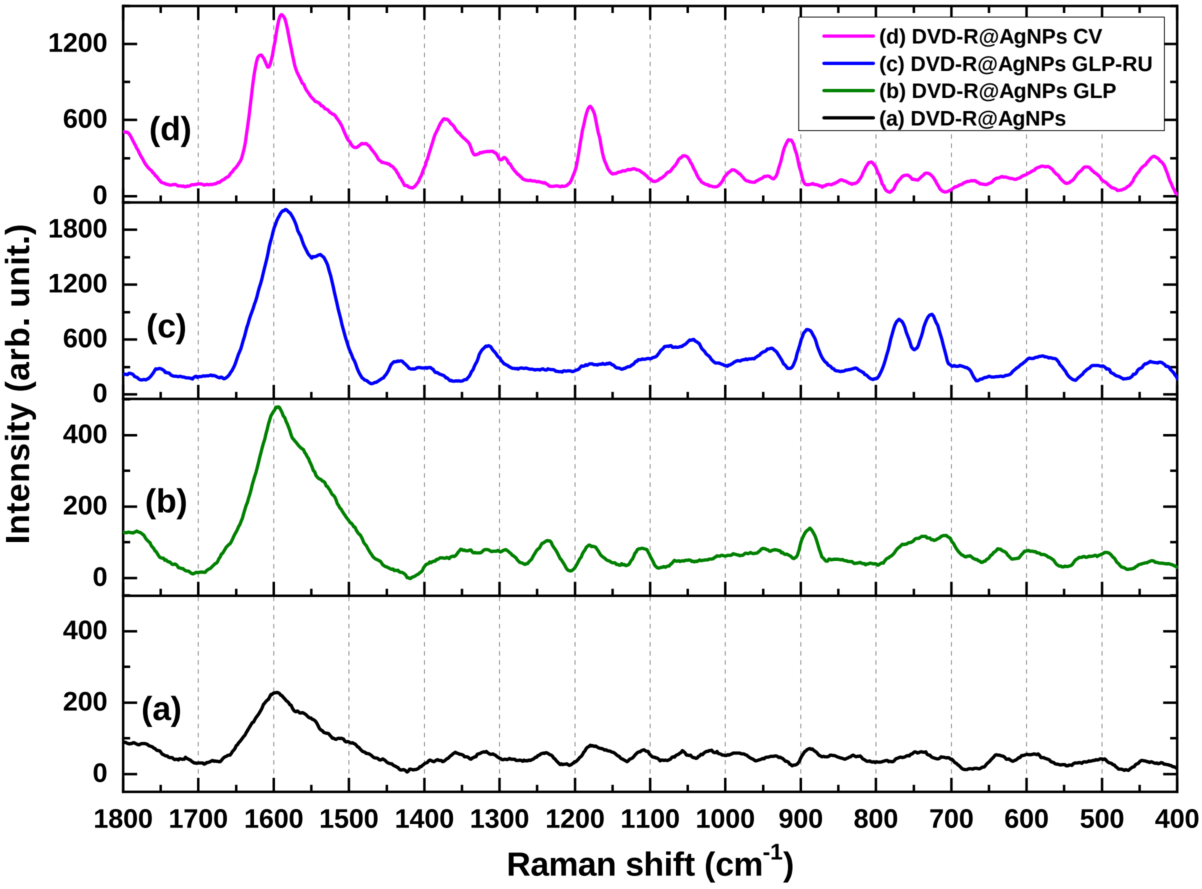

Source: The author.

stretched/breathing at 1,170 cm^{-1}, the stretching ring vibration C-C is at 1,531 cm^{-1} and 1,620 cm^{-1}, and the benzene ring deforms at 1,578 cm^{-1} (COLNIȚĂ et al., 2022; LIU et al., 2009). The CV spectra demonstrate that the PC substrate has significant spectral contributions below 0.02 ppm. As a result, the CV's distinctive fingerprint is no longer discernible.

One of the potential applications for SERS activity is the study of species that are important to the ecosystem. This method is sensitive enough to identify or analyze molecules or residues of herbicides with an organophosphorus structure such as GLP. GLP is the most popular active component for crop protection globally (VALLE et al., 2019; BAYLIS, 2000). GLP is present in food when it is applied right before harvest. The hazards of GLP are now the subject of research (BRUGGEN et al., 2018; CORBERA et al., 2005).

It is essential to compare the Raman spectra of compounds in the solid state with those of the same molecules adsorbed on AgNPs nanopatterned surfaces to understand and characterize SERS spectra. In addition, theoretical simulations and vibrational modes assignments can also help compare. The GLP and GLP-RU SERS spectra are shown in Figures 20(b) and 20(c), respectively. Under GLP-RU commercial information, there are "other ingredients" in the composition that we do not know. Despite this, the Raman signal is detected with the DVD-R@AgNP substrate.

SERS vibrational assignment of GLP achieves by comparing the Density Functional Theory (DFT) simulated Raman spectra when molecules are isolated or attached to a silver atom. For example, using the 2-^{13}C-glyphosate molecule, phosphono-methylglycine (PMG), and the primary GLP metabolite called Aminomethylphosphonic acid (AMPA) (KNEIPP; MOSKOVITS; KNEIPP, 2006; RADZIUK; MOEHWALD, 2015; CRAIG; FRANCA; IRUDAYARAJ, 2013; MAIER et al., 2007). The peak positions and their tentative assignment (from literature) of the Raman and SERS bands from the GLP molecules shows in Table 1. From the literature (CORBERA et al., 2005), not all Raman bands of GLP appear in the SERS spectra. With 514.15 nm excitation and DVD-R@AgNPs substrate, the GLP-RU´s most intense bands at 727 cm^{-1}, 769 cm^{-1}, 890 cm^{-1}, 1,043 cm^{-1}, 1,316 cm^{-1}, and 1,537 cm^{-1}. The bands at 727 cm^{-1}, 890 cm^{-1}, and 1,043 cm^{-1} were some more intense in the SERS GLP-RU spectra (see Figure 20(c), and the band at 890 cm^{-1} also appears for GLP spectra (see Figure 20(b)), showing that intensity decreases with decreasing concentration.

Table 1 – Experimental GLP peak positions (cm^{-1}) observed in Raman and SERS (**DVD-R@AgNPs** substrate) spectra.

Raman GLP from (MIKAC et al., 2022)	**SERS GLP-RU**	**SERS GLP**	**Tentative Assignment from** (MIKAC et al., 2022; COSTA et al., 2012; YAEL et al., 2014)
455	433		$\delta(PO_3)+\delta(NCCO)$ or $\rho(CH_2)+\delta(OH)$
485			$\delta(HOPO)+\rho(PCN)+\delta(NCC)+\delta(HOCO)+\rho(CH_2)$ or $\delta(OH)+\rho(CH_2)+(PO_2)$
509	506		$\delta(HOPO)+\delta(CNC)+\delta(HOCO)+\rho(CH_2)$ or $\delta(OH)+\delta(CH)$
576	579		$\delta\rho(PO_3)+$skel$(NCCOO)$ or $\delta(OH)+\delta(HO\text{-}C{=}O)$
646			$\nu(PC)+\delta(NCC)+\delta(COO)$
	727		$\nu(PC)$ or $\delta(NH)+\rho(CH_2)+\nu(P\text{-}OH)$
773	769		$\nu(PC)$ or $\delta(NH)+\rho(CH_2)+\nu(P\text{-}OH)$
798			$\nu(PC)+\rho(CH_2)+\rho(NH_2)+\nu(CCOO)$
864			$\nu(C\text{-}C)$ or $\rho(CH_2)+\delta(NH)+\nu(C\text{-}C)$
	890	887	$\rho(CH_2)$
917			CNCC $skel$
933	940		$\nu_s(PO_3)+\nu(PC)$
979 (XU et al., 2020)			$\rho(C_2H_2)$
992			$\nu_s(PO_3)+\tau(CH_2)+\rho(NH_2)+$CNCC $skel.$ or $\rho(CH_2)+\delta(OH)$
1036	1043		$\nu(C\text{-}N)/$CNCC $skel.+\nu_a(HOPO_2)/\nu_a(POO)$ or $\nu_s(PO_2)+\delta(OH)$
1081	1077		$\nu_a(PO_3)+\nu(C\text{-}N)$ or $\nu(C\text{-}N)+\nu(C\text{-}OH)$
1136		1111	$\nu_a(POH)$
1160			$\delta(CH_2+NH_2+CH_2)+\nu(COH)$
1196		1181	$\delta(CH_2+NH_2+CH_2)+\nu(COH)+\nu(CN)$ or $\tau(CH_2)+\delta(OH)$
1238		1235	$\nu(POH)+\tau(CH_2)+\nu(COH)+\delta(CNC)$ or $\tau(CH_2)$
1255			$\nu(PC)+\nu(POH)+\omega(CH_2)$ or $\omega(CH_2)$
1281			$\omega(CH_2)+\omega\tau(CH_2)+\delta(COH)+\nu(PC)$
1340	1316		$\omega\tau(CH_2)+\delta(COH)+\delta(CNC)/\nu(POH)$ or $\omega(CH_2)+\nu(C\text{-}C)$
1400			$\delta(CH_2)+\nu(CCOH)$
1427			$\delta[C(2)H_2]+\delta(POH)$ or $\delta(CH_2)$
1431 (shoulder)	1433		$\delta[C(4)H_2]+\delta(POH)$ or $\delta(CH_2)$

1466				ν(CC)+δ(CNH)/τ(NH_2)
1483				ω(NH_2)+δ(POH)
1566		1537		δ(NH_2)
		1584	1595	
1714				ν(C=O)
1728		1753		ν(C=O)

s: symmetric; as: asymmetric; ν: stretching; δ: bending; ρ: rocking; ω: wagging; τ for twisting; $skel$: skeleton vibration.

Source: The author.

3.6.3 Quantitative analysis of SERS substrate

To study the performance of the DVD-R@AgNPs substrate, we measure the Raman spectra at lower concentrations using CV, GLP, and GLP-RU. These analytes were diluted in ultrapure water to achieve CV solutions ranging from 0.02 to 0.09 ppm, GLP solutions prepared from 1 to 50 ppm, and GLP-RU solutions ranging from 20 to 1,000 ppm. The spectra of each analyte measured with DVD-R@AgNPs substrate showed characteristic bands as depicted in Figures: 21 for CV, 22 for GLP, and 23 for GLP-RU. All the SERS-active substrates fabricate under the same conditions.

Figure 21(a) shows the Raman bands for each CV concentration measurement. As we can see, the Raman intensity increases with the CV concentration. To detail the relationship between the Raman intensity and several concentrations' CV, we choose three SERS characteristics peaks at 422 cm^{-1}, 733 cm^{-1}, and 1,368 cm^{-1}, as is shown in the figure 21(b). In this plot, the error bars indicate the standard deviations of three measurements, and the correlation coefficient (R^2) indicated optimum fitting results as follows: R^2 values of 0.88 for 422 cm^{-1} band, 0.80 for 733 cm^{-1}, and 0.95 for 1,368 cm^{-1}. As a result, the Raman intensity as a function of the concentration showed a linear relation.

Figure 21 – (a) CV spectra for five differents concentrations using DVD-R@AgNPs substrate. (b) The linear relationship establishes for CV solutions.

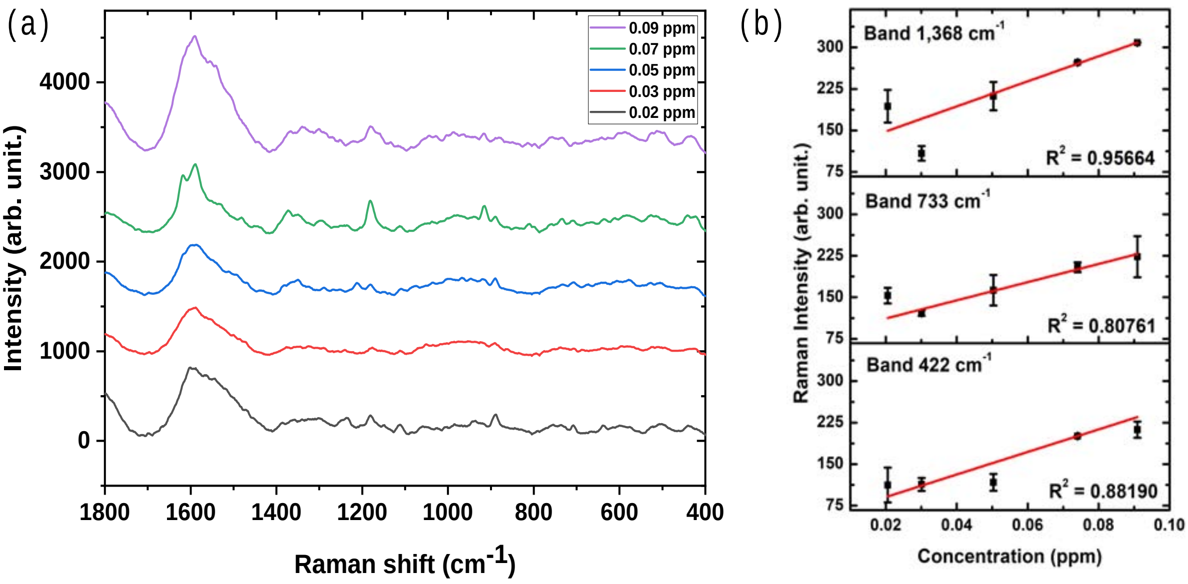

Source: The author.

Figures 22(a) and 23(a) shows the Raman bands for GLP and GLP-RU concentration measurement, respectively. As we can see, the Raman intensity increase with the increase of the GLPs concentration. To detail the relationship between the Raman intensity and several concentrations' GLPs, we choose three SERS characteristics peaks at 767 cm^{-1}, 933 cm^{-1}, and 1,043 cm^{-1}, as is showed in the figures 22(b) and 23(b).

Figure 22 – (a) GLP spectra for four differents concentrations using DVD-R@AgNPs substrate. (b) The linear relationship establishes GLP solutions.

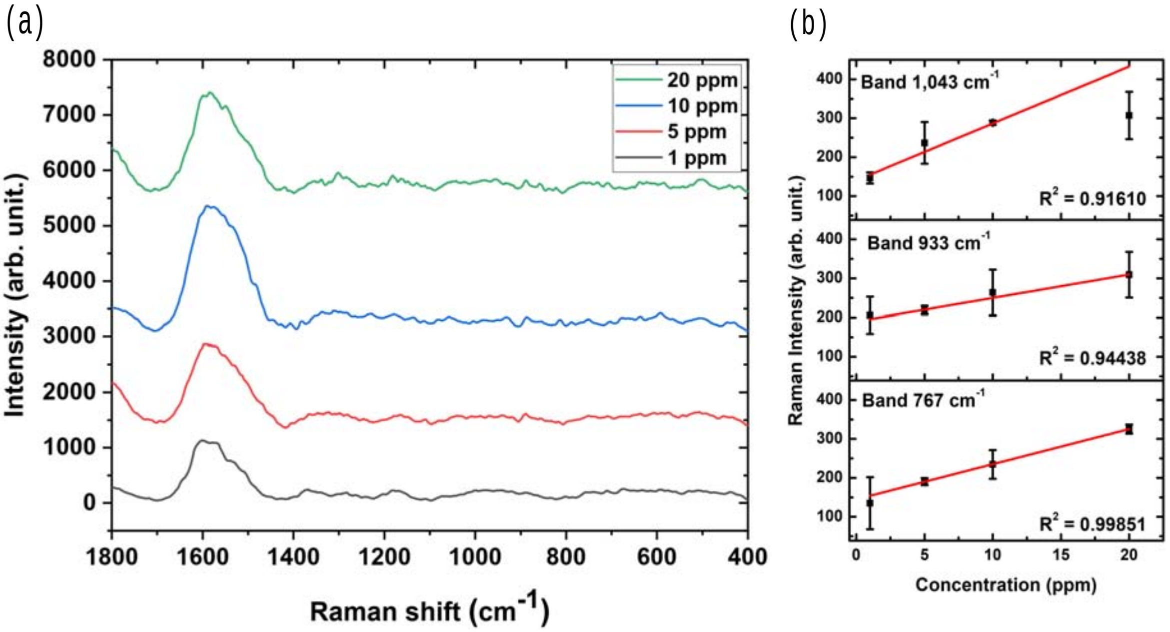

Source: The author.

In these plots, the error bars indicate the standard deviations of three measurements, and the correlation coefficient (R^2) indicates optimum fitting results. For GLP we have R^2 values of 0.99 for 767 cm^{-1} band, 0.94 for 933 cm^{-1}, and 0.91 for 1,043 cm^{-1}. For GLP-RU we have R^2 values of 0.86 for 767 cm^{-1} band, 0.98 for 933 cm^{-1}, and 0.96 for 1,043 cm^{-1}. As we expected, a reasonable linear response is found between the Raman intensity and concentration for both kinds of glyphosate.

Figure 23 – (a) GLP-RU spectra for seven differents concentrations using DVD-R@AgNPs substrate. (b) The linear relationship establishes for GLP-RU solutions.

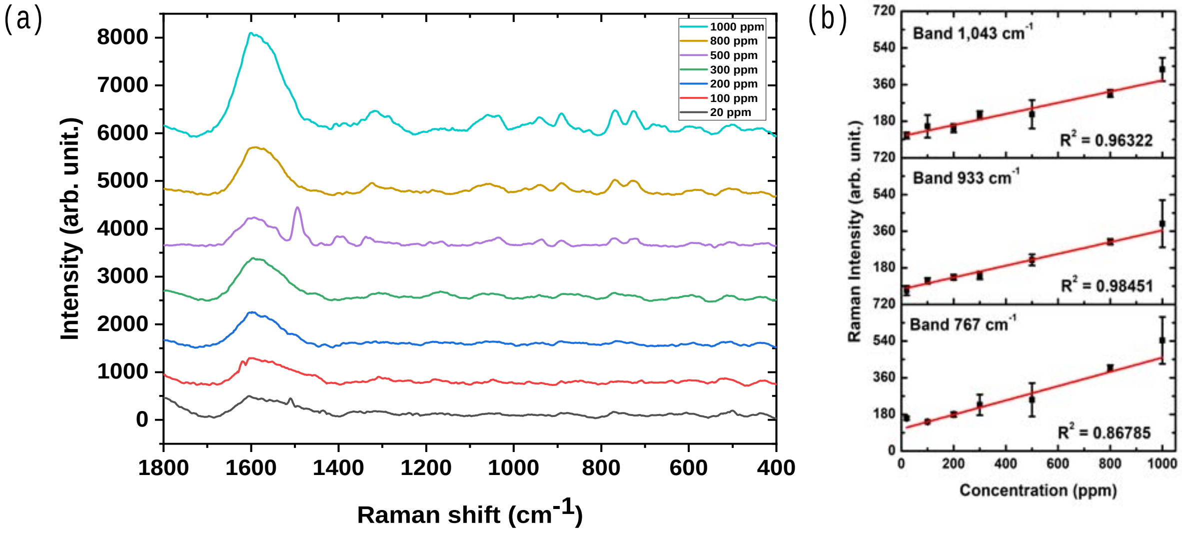

Source: The author.

The SERS signal's uniformity also plays a vital role. The uniformity of the silver nanoparticles was typically evaluated by RSD of Raman band intensity (LI et al., 2020). Then, we calculated RSD from the relation of the average between measurement and the standard deviation for all the concentrations of CV, GLP, and GLP-RU. Without standards for SERS architectures concerning reproducibility and stability, we assume an RSD of less than 20% as a quality SERS-active substrate result following Natan et al. (NATAN, 2006).

Table 2 shows the values of relative standard deviation (RSD), LOD and LOQ. The RSD calculations were less than 20% for all analytes bands, which is related to the quality of SERS-active substrate produced (MIKAC et al., 2022). In addition, these results indicate good silver nanoarrays uniformity (BHARATI et al., 2019) since RSD calculations connect the average measurement to the standard deviation.

The LOD and LOQ are obtained from σ=3% as standard deviations of the blank sample, i.e., DVD-R@AgNPs without analytes. The order magnitude of LOD and LOQ values was significantly different among CV, GLP, and GLP-RU samples, which were $\sim10^{-10}$ mol/L, $\sim10^{-7}$ and 10^{-8} mol/L, and $\sim10^{-6}$ mol/L, respectively. The CV was used as a reference sample for SERS measurements, allowing linear detection at very low concentrations. To compare CV results, Ag nanorods/AgNPs over a glass (SANCI; VOLKAN, 2009) or mesoporous silicon reports values of LOD around 10^{-10} mol/L (HARRAZ et al., 2015). The GLP is a standard sample, while GLP-RU is a commercial product used in agriculture that is a mixture of other substances. Thus, the difference in Raman intensity was expected, and the values of CV and GLP are in agreement with the literature (XU et al., 2020; XU et al., 2018).

Table 2 – LOD, LOQ and RSD calculations for CV, GLP and GLP-RU.

Analyte	**Bands (cm^{-1})**	**LOD (mol/L)**	**LOQ (mol/L)**	**RSD (%)**
CV	422	1.12×10^{-10}	5.50×10^{-10}	12.40
	733	1.39×10^{-10}	8.46×10^{-10}	8.64
	1,368	1.00×10^{-10}	4.46×10^{-10}	6.15
GLP	767	5.90×10^{-8}	1.96×10^{-7}	13.70
	933	8.88×10^{-8}	2.96×10^{-7}	17.93
	1,043	3.64×10^{-8}	1.21×10^{-7}	18.58
GLP-RU	767	1.52×10^{-6}	5.06×10^{-6}	6.31
	933	1.83×10^{-6}	6.11×10^{-6}	13.31
	1,043	1.93×10^{-6}	6.46×10^{-6}	9.74

Source: The author.

The LOQ values are in the same order of magnitude as LOD, except for GLP. This difference could be explained by the higher values of RSD, reflecting the standard deviation values. Apart from that, the most important result is the detection of commercial GLP-RU, being the highest level of global commercialization and historical use. In addition, the advantages of DVD-R@AgNPs are easy, practical, low-cost (around USD $0.22) and cheap manufacture with a good Raman enhanced due to nanogrooves at its surface.

According to the literature (COLNIȚĂ et al., 2022), the sensitivity in CV detection is about LOD $\sim 10^{-6}$ mol/L for both 25 and 10 nm Ag film thickness in a plastic substrate without periodic pattern and LOD between 10^{-12} and 10^{-10} mol/L with periodic nanotrenches imprinted. We obtained a LOD and LOQ of 10^{-10} mol/L in our work, which is lower than AgNPs over porous polymers found in the literature (LIU et al., 2014).

3.6.4 Enhancement factors calculations

The SERS enhancement factor calculates using the ratio of the SERS signal and the conventional Raman signal for both the same sample and experimental setup. The sample is the CV at 1 ppm concentration solution. The solid substrates used were: DVD-R@AgNPs for SERS and a regular silicon (100) wafer for traditional Raman. The EF estimated for the SERS substrate is shown in Table 3.

Table 3 – EF calculations for three CV Raman bands.

	CV Raman Bands (cm^{-1})		
	914	**1,178**	**1,589**
EF	3.26×10^{5}	5.27×10^{5}	8.56×10^{5}

Source: The author.

According to Table 3, the sensitivity of the substrate continues to be at a fairly steady order of magnitude based on the observed measurements. These results are in the same order of magnitude as those reported in the literature, 10^{3} to 10^{7} when the CV is used as a probe (ZHANG et al., 2015; SENAPATI et al., 2014) and higher than those obtained for silver-based substrates (FATEIXA; NOGUEIRA; TRINDADE, 2018; BARBOSA et al., 2021; LÓPEZ-CASTAÑOS et al., 2020; WEI; HUANG, 2018; SANTANA et al., 2006; WEI; HUANG, 2017). These results agree with SEM analysis; since two or more nanoparticles are near one another, the EF increases significantly, amplifying the Raman signal of the molecule. Thus, the AgNPs aggregation conduces to a considerable field enhancement, leading to more hot spot (multiple hot spots) generation in the DVD-R grating (DING et al., 2016; BHARATI et al., 2019).

4 Porous Silicon as a solid SERS-active platform

The solid substrate morphology control at the nanoscale ensures excellent and stable SERS signals. This chapter will describe the materials, methods, results, and discussion of the Porous Silicon (PSi) fabrication process as a solid SERS-active platform for Crystal Violet (CV) and Glyphosate (GLP) detection. Information about morphology, chemical, and spectroscopy measurements will be presented—additionally, enhancement parameters for performance analysis of solid SERS-substrates.

4.1 Porous silicon fabrication

Figure 24 – Schematic of electrochemical etching used to create a PSi substrate.

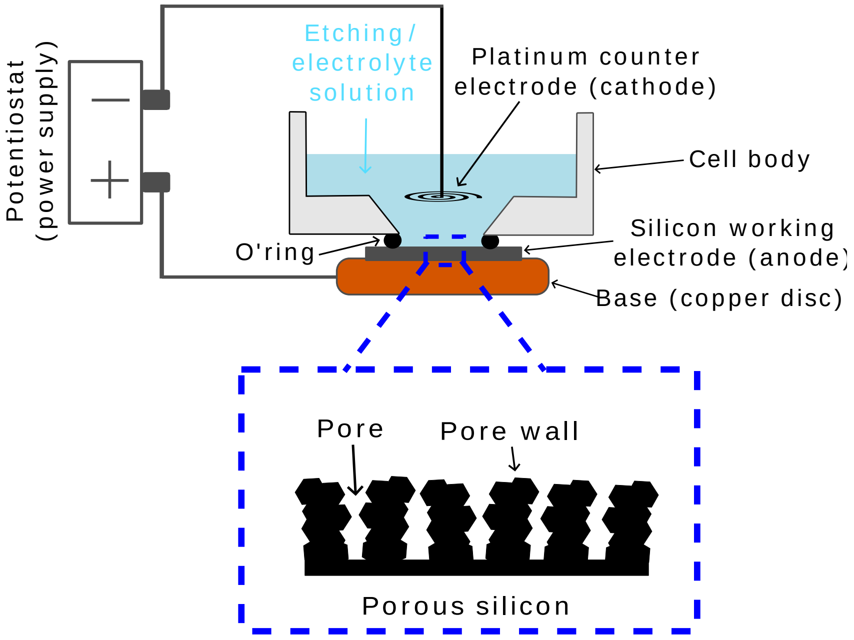

Source: The author.

A p-type, B-doped, one-side-polished Si wafer with low resistivity of 0.01 Ω/cm and a thickness of 500 μm, oriented in the $\langle 100 \rangle$ direction was used for monolayer porous silicon fabrication. P-type Si square (4 cm^2 of area) samples were put into lab-made Teflon cells, with a copper foil as the back working electrode-WE (see Figure 24). The metallic contact allows a better current conduction (figure 25(a)). A small O-ring adhered the PSi samples to the cells (Figure 24). The etching/electrolyte solution was composed of hydrofluoric acid (HF 40%) and ethanol (99.5%) in the volume proportion 1:1. Ethanol was used as a solvent to reduce the electrolyte's surface tension, allowing the solution to penetrate the pores as they were formed. A porous silicon monolayer is formed using 12 ml of HF:ethanol solution, which was applied to an area of roughly 0.90 cm^2, and a constant current density of 50, 100, and 200 mA/cm^2 was applied from 120 to 600 seconds. A Pt disk (2.27 cm^2) was immersed in the solution as a counter electrode as in figure 25(b). For monolayer PSi fabrication we use the manufacturing process described by (SILVA; BERNI, 2021; PAES et al., 2016).

Figure 25 – Fabricated cell for forming monolayer PSi: (a) cell parts. (b) Experimental setup of the PSi manufacture.

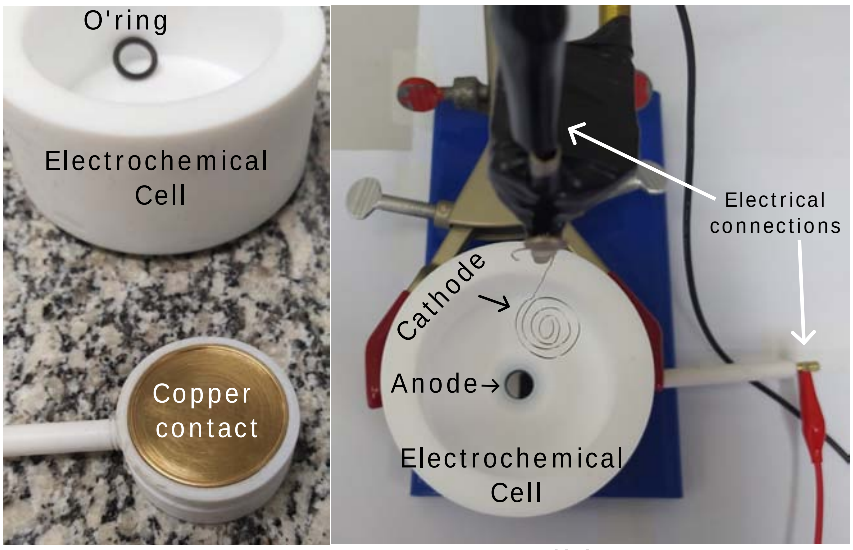

(a) (b)

Source: The author.

Notably, all samples were previously cleaned by electrochemical etching with a current density of 200 mA/cm^2, a period of 30 s, the identical HF solution (40%), and ethanol. This sacrificial porous layer is removed using an aqueous solution of sodium hydroxide (NaOH) in the proportion of 1 mol with 10%, by volume, of absolute ethanol, for 5 minutes in the cell. After etching, no other chemical or heat treatment was applied. The cells and samples were then rinsed with ethanol and dried in a vacuum.

The electrochemical etching of silicon to obtain PSi generally uses a power supply configured in a current operation controlled as a function of attack time. In the process of anodizing the silicon wafers to fabricate the PSi samples, Metrohm AutoLab potentiostat (PGSTAT128N) was used and controlled by a computer in the galvanostatic operating mode - controlled current of up to 1 A. Higher currents result in relatively large pores, high porosity, and the possibility of electropolishing and delaminating the samples. The parameter for forming PSi is the current density (J), not the applied current. Current density is related to the effective area of the anodized silicon, given in terms of mA/cm^2. This relationship maintains the proportion of the applied current in different effective regions.

The V-t curve of the HF (electrolyte) semiconductor junction depends on the nature of the semiconductor substrate as well as the ionic and molecular species present in the electrolyte. The application of an electrical current to the silicon bathed in a solution of HF (see Figure 26) induces a measurable potential circulating through the system. Figure 26(b) shows that the applied current (I=45 mA) does not cause fluctuations and high values in the measured potential during the electrochemical etching. At the silicon/electrolyte interface, the electronic charge carriers in the silicon of ionic form pass into the solution. The value of the applied current, the low potential measured, and the reaction taking place at the interface influence the formation of porous silicon.

Figure 26 – Anodization process: (a) measured potential (V) as a function of time (t) for the sacrificial porous layer, with a current density of 200 mA/cm^2 during 30 s. (b) measured potential (V) as a function of time (t) during the electrochemical etching, with a current density of 50 mA/cm^2 for 120 s.

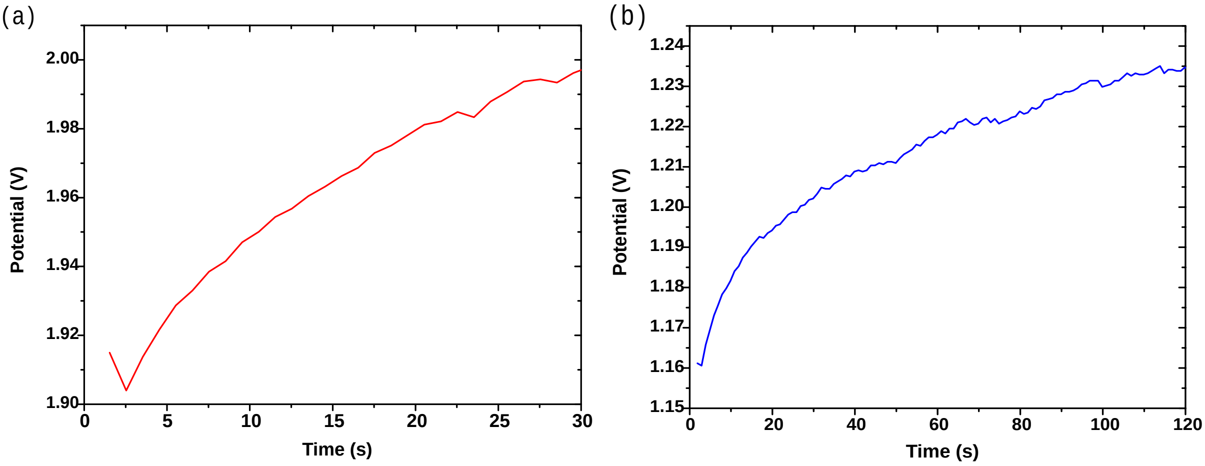

Source: The author.

4.2 Materials

Crystal Violet (CV) 1% ($C_{25}H_{30}N_3C_l$), a commercial non-selective herbicide GLP Roundup^{TM} (GLP-RU) 480 g/L (with GLP as the active ingredient) and the Standard GLP 100 mg/L ($C_3H_8NO_5P$), obtained by SpecSol Quimlab (Brazilian industry) are the probe molecules to study the PSi as solid SERS-active activities. All solutions were prepared with ultrapure water (18.2 MΩcm) produced by Sartorius Arium®Comfort Ultrapure Water Systems.

4.3 SERS substrate fabrication

Figure 27 depicts the PSi@AgNPs substrates manufacturing process. After the porous silicon formation (Figure 24), the substrates are put on the CCPD system for AgNPs deposition. The same experimental setup and CCPD's characteristic system described in section 3.3 were used.

Figure 27 – Schematic representation of the SERS substrate fabrication process for PSi: (a) AgNPs deposited by CCPD method over the porous silicon structure, and (b) direct Raman measurements.

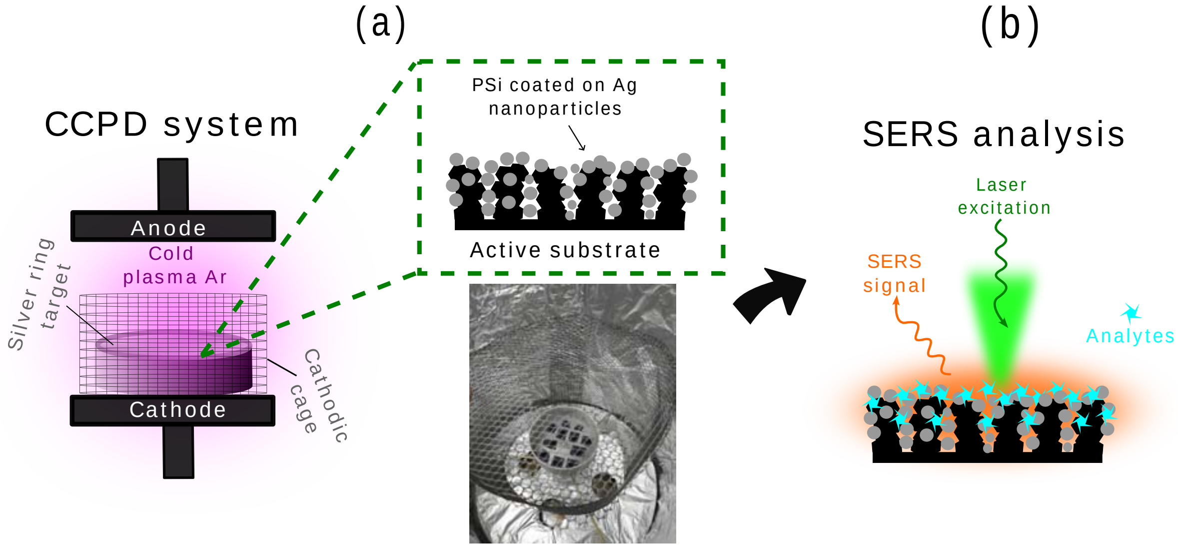

Source: The author.

4.4 Morphological and Chemical Characterization

Field Emission Gun Scanning Electron Microscopy (FEG-SEM) was used for morphology analysis, while SEM with energy-dispersive X-ray spectroscopy (SEM-EDS) was used for atomic composition analysis. The FEG-SEM analysis used the MIRA3 TESCAN field emission instrument, from the LABAS-INPE laboratory, with secondary electrons and an accelerating voltage of 15 kV and 5 kV. The SEM-EDS analysis was performed using the Carl ZEISS MA 10 + EDX INCA instrument, with an accelerating voltage of 20 kV.

4.5 Optical Measurements and quantitative analysis

To measure the Raman signal of each analyte solution on the PSi@AgNPs surface, a 5 μL drop of each solution was placed on the substrate. The Raman spectra were collected using a Raman HORIBA LabRam HR Evolution Spectrometer with a 514.15 nm excitation laser and CCD camera, from the LABAS-INPE laboratory. The laser power of 0.64 mW was focused using a 20× objective lens with a numerical aperture (NA) of 0.40, which is typical for SERS measurements. The Raman spectra were collected between 400 and 1,800 cm^{-1}, with a 180-second exposure time and two accumulation numbers.

LOD, LOQ, and the enhancement factor were calculated to evaluate the performance of the PSi@AgNPs substrate with all analytes, following the equations 3.1, 3.2, and 3.3.

4.6 Results and Discussion

This section will primarily focus on the results and discussions derived from the characterization of SEM-FEG imaging and Raman spectroscopy. Firstly, we will showcase the nanometric structure of PSi and the aggregated AgNPs. We will then describe the probe molecules' principal peak positions and SERS vibrational assignments. Lastly, we will present the quantitative analysis of the PSi@AgNPs substrate, including the detection of low concentrations of Crystal Violet (CV) and Roundup^{TM} Glyphosate (GLP-RU), as well as the calculation of the enhancement factor for solid SERS-active substrates.

4.6.1 SEM characterization

4.6.1.1 SEM analysis of Porous Silicon structure

Electrochemical anodization is a highly controlled process that allows for precise manipulation of pore morphology and size by adjusting current density, etching time, and electrolyte concentration. As a result of this optimization, various types of pores are formed, such as illustrated in Figure 28(a). All the silicon wafers are the same type and quantity of dopants and have $\langle 100 \rangle$ as crystalline orientation, these factors influence the structural characteristics of these pores formation.

Figure 28 – Morphology of porous silicon (PSi) template prepared with different etching current densities and times. SEM analysis was performed with an accelerating voltage of 20 kV. The scale bar corresponds to 1 μm.

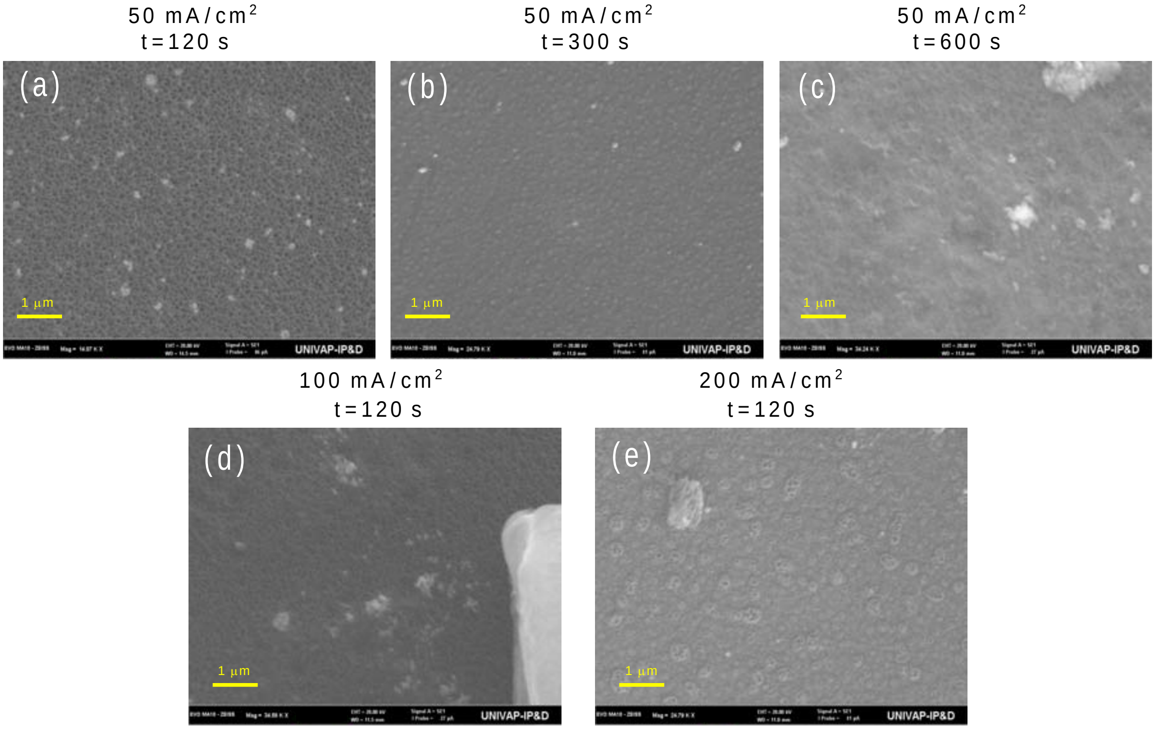

Source: The author.

When the current density increases for the same etching time, the diameter of the pores decreases, resulting in a decrease in porosity, as evident when comparing Figures 28(a) with 28(d) and 28(e). The porous layer in Figure 28(e) exhibits a random pore shape, making it challenging to identify, and unfortunately, the film delaminated itself under a vacuum after one day. In contrast, the pore shape in Figure 28(a) is more well-defined and clear compared to Figure 28(d).

Conversely, when the etching time is increased for the same current density, no pore formation occurs, as can be observed by comparing Figures 28(a), 28(b), and 28(c). Figures 28(b) and 28(c) display the rugosity on the silicon wafer rather than the porosity. Observing the changes in the etching current density during the process allows us to deduce that the porous structure serves as a unique fingerprint of the current density, as evidenced by the obtained results (ADAWYIA; ALWAN; ALLAA, 2016; SAILOR, 2012). Consequently, we use the porous silicon parameter from the first sample (Figure 28(a)) for SERS-active substrate manufacturing.

4.6.1.2 SEM analysis of Porous Silicon SERS-active substrate

Figure 29(a) displays SEM images of the porous silicon (PSi) structure following the electrochemical etching process. The surface exhibits a regular and homogeneously porous structure, with pores diameters ranging between 40 and 60 nm. Subsequently, in Figure 29(b), after four hours of the CCPD process, the AgNPs aggregated disperse across the etched area on the silicon wafer surface. The small black areas visible in the image correspond to the interior pore regions, which are separated by the pore distances. Both, in pore-regions and pore-distances, the aggregated AgNPs are found.

Figure 29 – SEM-FEG imaging of porous silicon's structure: (a) without and (b) with the AgNPs thin film. (c) Cross-section FEG images of PSi@AgNPs substrate.

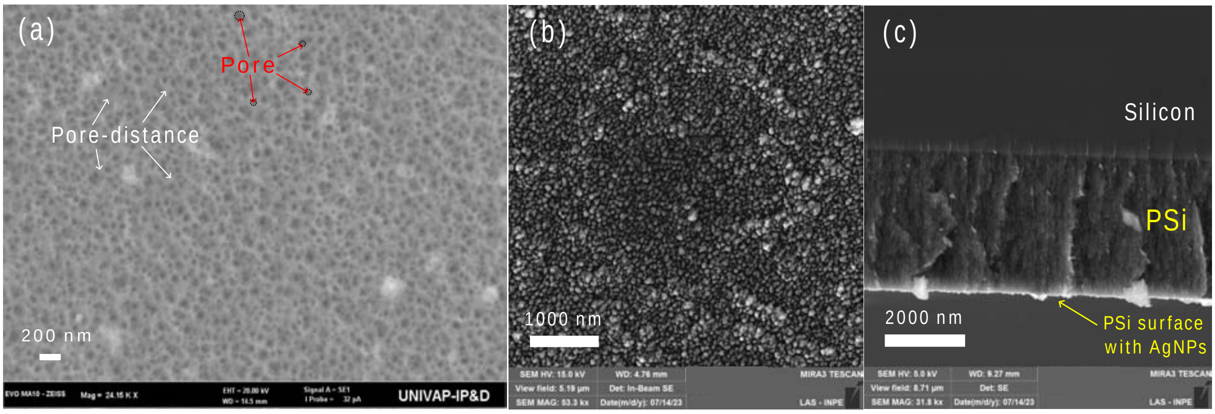

Source: The author.

Most AgNPs are situated within the pore distance, while others are distributed along a depth of 310 nm, as evident from the silver layer at the bottom of Figure 29(c).

The thickness of the porous silicon, achieved through electrochemical etching, measures 3.37 μm in diameter, as observed in the cross-section of the PSi@AgNPs substrate (refer to Figure 29(c)).

In Figure 30(a), the majority of the aggregated AgNPs have a diameter of 50 nm. Additionally, we can observe other aggregated AgNPs, sized at 25 and 30 nm, located within the pores. This outcome enhances the substrate's porosity.

Figure 30(b) presents the elemental EDS spectra of the PSi@AgNPs substrate. The EDS spectra display peaks at 0.27, 0.52, and 1.57 keV, corresponding to carbon, oxygen, and silicon, which are components of the substrate matrix. Additionally, there is a peak at 3.00 keV, indicating the presence of silver nanoparticles on the surface of the PSi@AgNPs substrate. Semi-quantitative EDS investigation confirms that silver accounts for approximately $\sim$15.8 $\pm$ 0.1 At% of the substrate's composition. The dispersive X-ray spectroscopy scanning employed an energy of 5 keV for this analysis. This superficial analysis and the relation between the pore size and aggregated AgNPs diameter, verify that most of the nanoparticles are confined to specific regions of the pore (top of the pore's distance) and it is not possible to determine if they permeate the entire structure.

Figure 30 – SEM-FEG imaging of porous silicon (PSi) coated by a silver thin film, i.e. PSi@AgNPs substrate: (a) 182 kx magnification. (b) Energy dispersive analysis of the Ag thin film on PSi surface region.

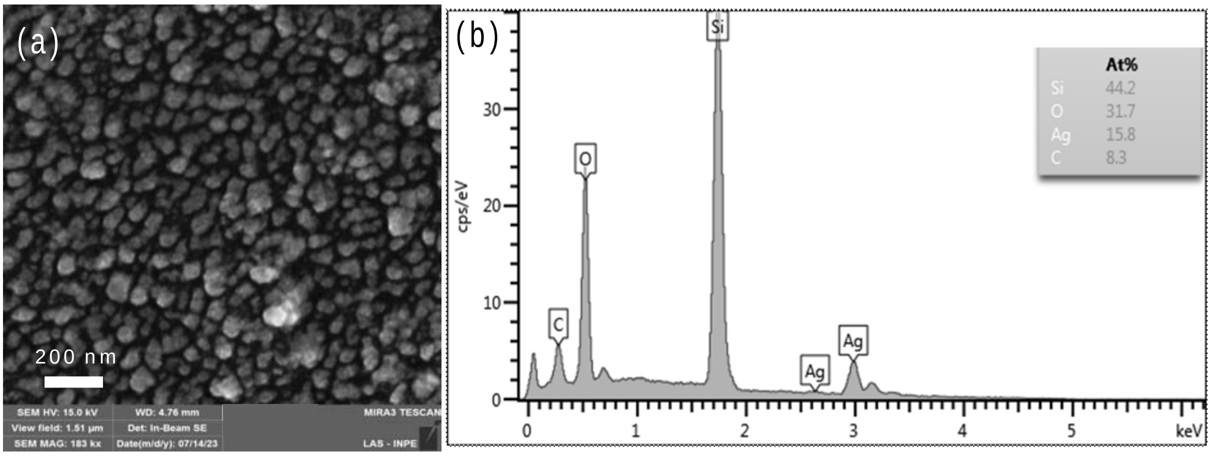

Source: The author.

The use of silver nanoparticles over a porous silicon template enables a significant increase of nucleation sites for these nanoparticles (see Figure 29(b)). Moreover, PSi provides an abundance of growth sites due to the nanopores (see Figure 29(a)). The controlled manipulation of PSi morphology allows for enhancing the density of hot spots, leading to the aggregation of metal nanoparticles (see Figure 30(a)). This renders PSi an invaluable template for AgNPs deposition, facilitated by the presence of Si-H terminated groups on the PSi surface, which serve as efficient reducing agents for silver ions without requiring any additional reducing agents (HARRAZ et al., 2015).

Consequently, AgNPs/PSi hybrids have emerged as promising sensing substrates for SERS, demonstrating remarkable Raman enhancement, surpassing ten orders of magnitude as reported in the literature (VIRGA et al., 2013; ALWAN; YOUSIF; WALI, 2017; ALWAN; YOUSIF; WALI, 2018; JABBAR; ALWAN; HAIDER, 2018).

4.6.2 Raman and SERS analysis

The Raman signal detection was employed to examine the SERS activity of the PSi@AgNPs substrate. Figure 31(a) displays the spectrum of the PSi@AgNPs substrate without any analytes. Three principal peaks at 520, 810, and 1,070 cm^{-1} can be identified for the PSi@AgNPs substrate matrix.

The typical SERS spectra of 0.035 mg/ml (35 ppm) GLP, 1.5 mg/ml (1,500 ppm) GLP-RU, and 0.001 mg/ml (1 ppm) CV, observed on the PSi@AgNP substrates, are presented in Figures 31(b), 31(c), and 31(d), respectively. All spectra have undergone the same background adjustment and smoothing.

Figure 31 – SERS spectra of active substrate PSi@AgNPs (a) blank without analyte, (b) with 0.035 mg/mL GLP, (c) with 1.5 mg/mL GLP-RU, and (d) with 0.001 mg/mL CV.

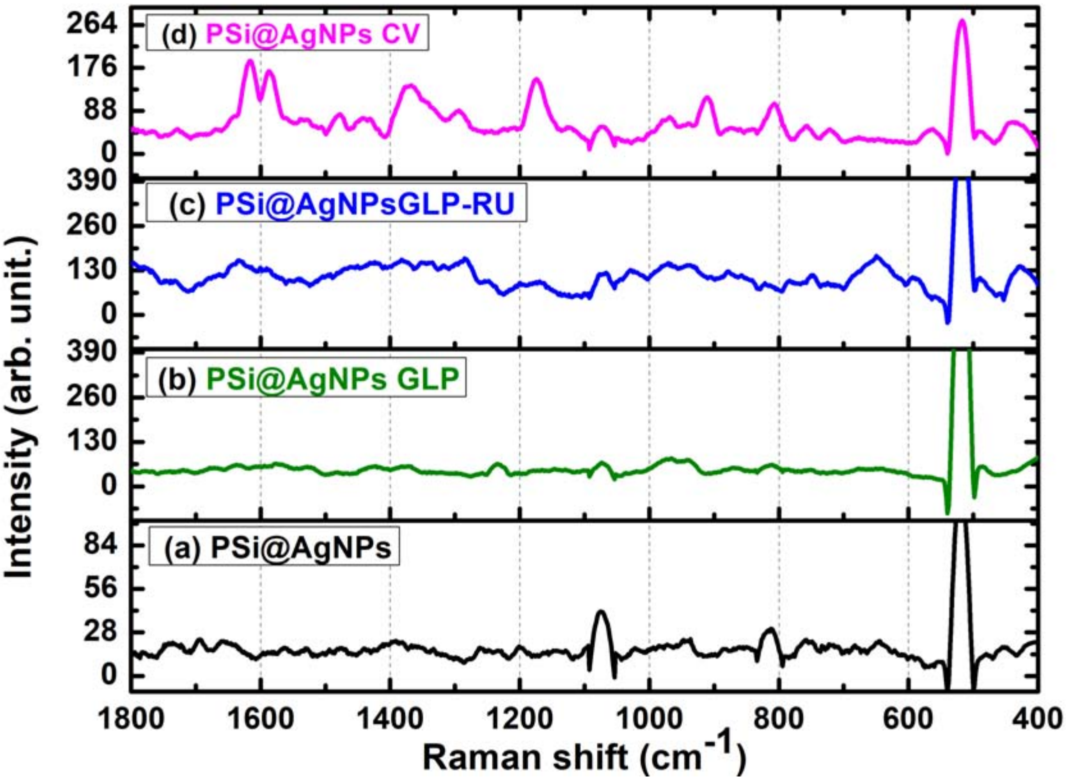

Source: The author.

The Raman signal enhancement using PSi@AgNPs is achieved through both charge transfer (CT) and resonance of the laser with surface plasmon resonance (SPR). The plasmonic resonance of Ag-coated PSi is influenced by the size, shape, and mutual electromagnetic interaction of their nanoparticles (NPs), as well as the dielectric property of the PSi substrate. Typically, this enhancement is limited to the visible spectrum (KELLY et al., 2003; STAROWICZ et al., 2018).

When an analyte is placed on a SERS substrate (PSi@AgNPs), a complex interaction occurs between the metal framework of the nanoparticles, the substrate's porosity, and the analyte. As a result, the Raman signals of specific modes undergo significant enhancement in SERS due to this intricate interplay. Furthermore, the SERS signal enhancement is present when the excitation wavelength is on-resonant with the electronic transitions of the analyte and resonance Raman effects. In the case of the 514 nm excitation wavelength, the CV dye molecules, which exhibit maximum absorption at ~590 nm (ŠKRABIĆ et al., 2019), are on plasmonic resonance, as evident in the SERS spectrum of Figure 31(d).

Using the PSi@AgNPs substrate it is possible to identify the peak positions of CV. The molecular structure and propeller-like configuration of CV-organic dye give rise to three distinct vibrational modes evident in its Raman spectrum. These modes encompass a core carbonium ion and three symmetric benzene rings. One of these vibrational modes is characterized by the C^+-phenyl vibrations of the central carbon atom, occurring at wavenumbers up to 450 cm^{-1}. Another group corresponds to the N-phenyl stretching vibrations of the nitrogen atoms, falling within the range of 1,350 to 1,400 cm^{-1}. Additionally, the Raman spectrum reveals skeletal ring/C-H deformations and ring stretching modes, observable at wavenumbers between 400 and 1,300 cm^{-1} and beyond 1,400 cm^{-1}. The assignments of Raman and SERS bands of CV dye are collected in Table 4. The vibrational bands for both SERS and normal Raman are well-agreed with previously reported studies (FATEIXA; NOGUEIRA; TRINDADE, 2018; COLNIȚĂ et al., 2022; MOROVVATI; MALEKFAR, 2019; LIU et al., 2009; ZEIRI et al., 2012; HARRAZ et al., 2015; AL-SYADI et al., 2022; JIANG et al., 2014).

SERS activity holds great promise for various applications, including the study of essential ecosystem components. This highly sensitive method proves effective in identifying and analyzing molecules or residues of herbicides with an organophosphorus structure, such as GLP—the widely used active component for crop protection worldwide (VALLE et al., 2019).

Figures 31(b) and 31(c) display the SERS spectra of GLP and GLP-RU, respectively. When excited with 514.15 nm and employing the PSi@AgNPs substrate, the GLP-RU exhibits its most intense bands at ~649, ~785, ~877, ~941, ~971, ~1,029, ~1,066, ~1,169, ~1,248, ~1,285, ~1,342, ~1,408, ~1,423, ~1,450, ~1,482 cm^{-1}. The bands at 810 and 1,074 cm^{-1} are also present in the GLP (see Figure 31(b)), then this band

Table 4 – Assignments of Raman bands of CV in SERS (PSi@AgNPs substrate) and normal Raman conditions.

Raman	**SERS CV**	**Assignment from** (AL-SYADI et al., 2022; HARRAZ et al., 2015; JIANG et al., 2014)
436	437	Phenyl-C-phenyl out-of-plane antisymmetric bending.
722	720	C-N-C symmetric stretching.
797	808	Phenyl-H out-of-plane antisymmetric bending.
908	908	Phenyl ring breathing mode.
1168	1173	C-phenyl, C-H in-plane antisymmetric stretching.
1376	1370	C-N, Phenyl-C-phenyl antisymmetric stretching.
1530	1537	Phenyl-N antisymmetric stretching.
1580	1587	C-phenyl in-plane antisymmetric stretching.
1612	1615	C-phenyl in-plane antisymmetric stretching.

Source: The author.

corresponds to PSi@AgNPs substrate spectra without analyte (blank). Although the exact composition of “other ingredients” in GLP-RU remains undisclosed in the commercial information, the Raman signal is still detected with the PSi@AgNP substrate.

Notably, not all Raman bands of GLP are observed in the SERS spectra (CORBERA et al., 2005). Table 5 presents the peak positions and their tentative assignments of the Raman and SERS bands from the GLP molecules (FEIS et al., 2020; MIKAC et al., 2022; COSTA et al., 2012; YAEL et al., 2014).

Table 5 – Experimental GLP peak positions (cm^{-1}) observed in Raman and SERS (**PSi@AgNPs** substrate) spectra.

Raman GLP[1]	**SERS GLP-RU**	**SERS GLP**	**Tentative Assignment**[2]
646	649	643	ν(PC)+δ(NCC)+δ(COO)
798	785	790	ν(PC)+ρ(CH$_2$)+ρ(NH$_2$)+ν(CCOO)
864	877	869	ν(C-C) or ρ(CH$_2$)+δ(NH)+ν(C-C)
933	941	941	ν_s(PO$_3$)+ν(PC)
979[3]	971	966	ρ(C$_2$H$_2$)
1036	1029		ν(C-N)/CNCC $skel.$+ν_a(HOPO$_2$)/ν_a(POO) or ν_s(PO$_2$)+δ(OH)
1081	1066		ν_a(PO$_3$)+ν(C-N) or ν(C-N)+ν(C-OH)
1136		1144	ν_a(POH)
1238	1248	1234	ν(POH)+τ(CH$_2$)+ν(COH)+δ(CNC) or τ(CH$_2$)
1281	1285		ω(CH$_2$)+$\omega\tau$(CH$_2$)+δ(COH)+ν(PC)
1340	1342		$\omega\tau$(CH$_2$)+δ(COH)+δ(CNC)/ν(POH) or ω(CH$_2$)+ν(C-C)
1400	1408		δ(CH$_2$)+ν(CCOH)
1427	1423	1423	δ[C(2)H$_2$]+δ(POH) or δ(CH$_2$)
1466	1450		ν(CC)+δ(CNH)/τ(NH$_2$)
1483	1482		ω(NH$_2$)+δ(POH)
		1579	

s: symmetric; as: asymmetric; ν: stretching; δ: bending; ρ: rocking; ω: wagging; τ for twisting; $skel$: skeleton vibration.

Source: The author.

---

[1] From (MIKAC et al., 2022).

[2] From (MIKAC et al., 2022; COSTA et al., 2012; YAEL et al., 2014).

[3] From (XU et al., 2020).

4.6.3 Quantitative analysis of SERS substrate

To evaluate the efficiency of the PSi@AgNPs substrate, we conducted Raman spectroscopy measurements at varying concentrations of two target analytes: CV and GLP-RU. Both analytes were diluted in ultrapure water to create CV solutions ranging from 0.06 to 1 ppm and GLP-RU solutions ranging from 300 to 2,500 ppm concentrations. Notably, all the SERS active substrates were fabricated under identical conditions, ensuring consistency and reliability in the experimental setup.

Figure 32(a) displays the Raman bands corresponding to each CV concentration measurement. As anticipated, the Raman intensity demonstrates a clear increase with rising CV concentration. In order to understand the relationship between Raman intensity and various CV concentrations, we focused on three key SERS characteristic peaks at 909 cm^{-1}, 1,589 cm^{-1}, and 1,614 cm^{-1}, as illustrated in Figure 32(b). Notably, the error bars in this plot represent the standard deviations from three independent measurements, while the correlation coefficients (R^2) serve as indicators of the fitting quality. The obtained R^2 values were 0.83 for the 909 cm^{-1} band, 0.82 for the 1,589 cm^{-1} band, and an impressive 0.99 for the 1,614 cm^{-1} band. These high R^2 values validate the optimum fitting results and demonstrate a strong linear relationship between Raman intensity and concentration. In conclusion, our findings affirm the linear correlation between Raman intensity and the concentration of CV, highlighting the potential of the PSi@AgNPs substrate for quantitative analyses and sensitive detection applications.

Figure 32 – (a) CV spectra for five different concentrations using PSi@AgNPs substrate. (b) The linear relationship establishes CV solutions.

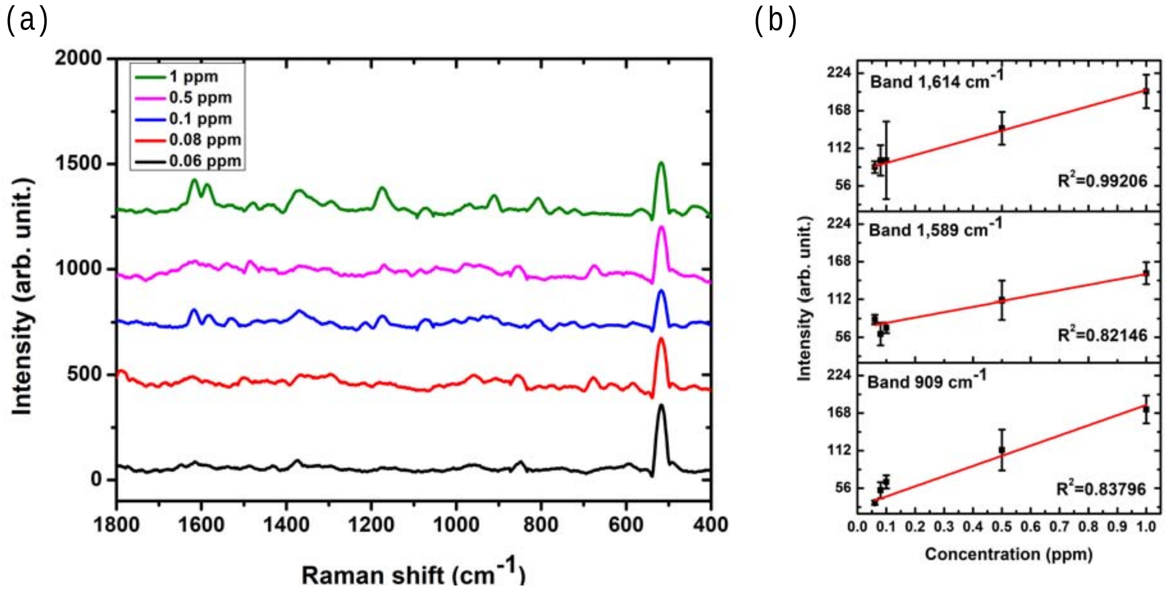

Source: The author.

In Figure 33(a), the Raman bands corresponding to the GLP-RU concentration measurements are presented. Initially, identifying the GLP-RU Raman bands and establishing whether the Raman intensity increased with concentration presented some challenges due to their formulation components. To enhance clarity, we focused on two of the most intense characteristic peaks at 790 cm^{-1} and 966 cm^{-1}, as illustrated in Figure 33(b).

Similar to the CV analysis, the error bars in this plot represent the standard deviations obtained from three independent measurements. For GLP-RU, the linear fitting correlation results yielded R^2 values of 0.92 for the 790 cm^{-1} band and an encouraging 0.95 for the 966 cm^{-1} band.

As expected, we observed a reasonable linear response between Raman intensity and GLP-RU concentration. However, it's worth noting that the standard deviations for the 790 cm^{-1} band appeared larger when compared to the 966 cm^{-1} band. This discrepancy might be attributed to variations in the sensitivity of the two bands or experimental factors affecting their measurements.

Figure 33 – (a) GLP-RU spectra for five different concentrations using PSi@AgNPs substrate. (b) The linear relationship establishes GLP-RU solutions.

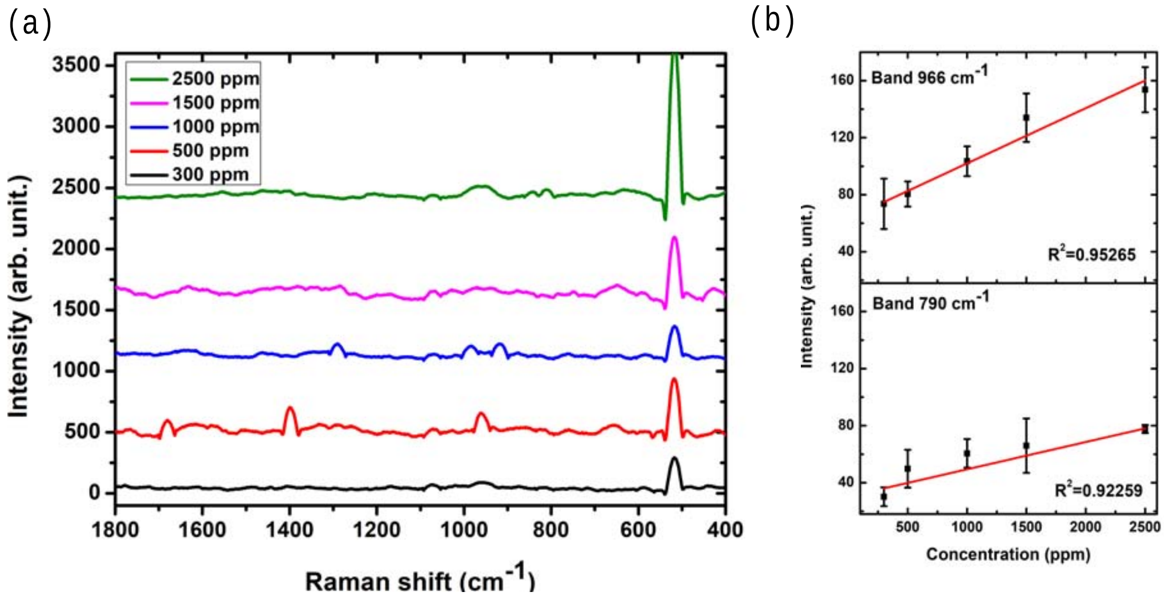

Source: The author.

As mentioned in Section 3.6.3, the uniformity of silver nanoparticles plays a crucial role in SERS, and its assessment typically involves the RSD parameter (LI et al., 2020). We calculated the RSD by determining the average between measurements and the standard deviation for all concentrations of CV and GLP-RU, as presented in Table 6. Notably, the RSD calculations for all analyte bands were below 20%, except for the 1,614 cm^{-1} band. This gap may be a result of band different sensitivities or experimental variables influenced that measurement. In general, RSD values indicate a good quality of the SERS-active substrate produced (NATAN, 2006; MIKAC et al., 2022).

By considering Equations 3.1 and 3.2 for LOD and LOQ calculations, we obtained the respective values presented in Table 6, where PSi@AgNPs without analyte is the blank sample. The orders of magnitude for LOD and LOQ values differ significantly between the CV and GLP-RU samples, which could be attributed to the high values of RSD, reflecting the standard deviation estimates.

Table 6 – LOD, LOQ, and RSD calculations for CV and GLP-RU using PSi@AgNPs substrate.

Analyte	Bands (cm^{-1})	LOD (mol/L)	LOQ (mol/L)	RSD (%)
CV	909	1.50×10^{-12}	9.94×10^{-14}	17.37
	1,589	2.85×10^{-12}	3.57×10^{-13}	16.23
	1,614	1.89×10^{-12}	1.57×10^{-13}	22.70
GLP-RU	790	2.78×10^{-2}	9.28×10^{-2}	18.18
	966	1.37×10^{-2}	4.58×10^{-2}	12.80

Source: The author.

For CV, the LOD was $\sim10^{-12}$ mol/L, and the LOQs were around 10^{-14} mol/L and 10^{-13} mol/L, respectively. These results demonstrate the remarkable linear detection capability of CV as a probe dye molecule for SERS measurements, allowing precise detection at exceptionally low concentrations.

To provide context, it is worth noting that when comparing the results for CV to those using Ag nanorods/AgNPs over mesoporous silicon, the reported LOD values were $\sim10^{-10}$ mol/L (HARRAZ et al., 2015). This comparison underscores the superior sensitivity achieved with the PSi@AgNPs substrate for CV detection. Previous research has reported a LOD of approximately 10^{-12} mol/L using macroscopic dendritic copper nanoleaves (XU et al., 2022), and a LOD of approximately 10^{-10} mol/L using AgNPs-coated filter paper for CV detection (WEI; HUANG, 2017).

In contrast, for GLP-RU, both the LOD and LOQ were approximately 10^{-2} mol/L ($\sim$4.70 mg/ml). The comparatively higher values for GLP-RU indicate that it may not be as suitable for ultrasensitive detection such as CV. Despite of this, our findings highlight the potential of the PSi@AgNPs substrate for semi-quantitative detection of GLP-RU traces. Further investigation and refinement could help address the variability in the Raman bands' intensity and sensing sensibility, promoting the way for more precise and reliable analyses in environmental and agricultural applications.

Recently, significant advancements have been made in using porous silicon (PSi) substrates for detecting various pesticide molecules. For instance, Thiram, a common pesticide, has been successfully detected with impressive LOD of 1 μM and 0.1 ppm, as reported by Vendamani et al. (VENDAMANI et al., 2021) and Moram et al. (MO-

RAM; BYRAM; SOMA, 2023), respectively. Another noteworthy study utilized PSi-plated palladium nanoparticles as surface-enhanced Raman scattering (SERS) substrates for detecting the insecticide imidacloprid. This study achieved a remarkable LOD of 10^{-9} M (∼0.17 ppb) (AL-SYADI et al., 2021). Similarly, PSi has proven effective in detecting the residue of Diphenylamine (DPA) with the same LOD of 10^{-9} M (mol/L) (NGUYEN et al., 2022). However, despite these promising findings, the use of PSi as a SERS substrate for detecting the widely used commercial non-selective herbicide, GLP Roundup$^{\text{TM}}$, has not been explored in the literature yet. This highlights a potential area of research where PSi-based SERS could find valuable applications for pesticide detection. Further studies in this direction would undoubtedly contribute to advancing the field and enhancing our understanding of PSi's potential as a versatile and sensitive substrate for environmental monitoring.

4.6.4 Enhancement factors calculations

A dye molecule, Crystal Violet (CV), at a concentration of 1 ppm in solution, was used as a probe to evaluate the sensing capabilities of the substrate using the SERS technique. The solid substrates used were PSi@AgNPs for SERS and a p-type, B-doped Si (100) wafer for conventional Raman. The enhancement factor (EF) estimated for the SERS substrate is shown in Table 7.

Table 7 – EF calculations for three CV Raman bands using PSi@AgNPs substrate.

	CV Raman Bands (cm^{-1})		
	909	**1,589**	**1,614**
EF	2.89×10^5	5.61×10^5	1.97×10^5

Source: The author.

Based on Table 7, the substrate's sensitivity remains consistently within a specific 10^5 order of magnitude, as observed. These results align with previous studies in the literature, which reported sensitivity ranging from 10^3 to 10^7 when using CV as a probe (AL-SYADI et al., 2022; BARBOSA et al., 2021; MOROVVATI; MALEKFAR, 2019; ŠKRABIĆ et al., 2019; HARRAZ et al., 2015; ZHANG et al., 2015; SENAPATI et al., 2014; ZEIRI et al., 2012). Moreover, the sensitivity of PSi as a template for AgNPs or PSi@AgNPs SERS-active substrates can increase due to many growth sites and the density of hot spots (WALI; HASAN; ALWAN, 2019; ALWAN; YOUSIF; WALI, 2017; JABBAR; ALWAN; HAIDER, 2018). This phenomenon enhances the substrate's sensing capabilities, making it a promising candidate for various applications.

5 Conclusions

In this study, we manufactured and investigated solid SERS-active substrates by growing AgNPs on DVD-R and porous silicon, creating hybrid platforms capable of detecting dye probe molecules and environmental pollutants. The morphology, composition, and SERS properties of these substrates were analyzed using FEG-SEM and Raman scattering with an excitation wavelength of 514.15 nm.

Our results demonstrated the excellent uniformity of silver nanoparticles on the substrates, achieved through the Cathodic Cage Plasma Deposition (CCPD) technique. This uniformity is crucial for ensuring reliable and reproducible SERS measurements. Consequently, both substrates show promising potential for precise and sensitive detection applications in environmental monitoring and chemical analysis.

The LOD, LOQ, and EF calculations provided valuable insights into the sensitivity and detection limits of the substrates for various analytes, further emphasizing their versatility for diverse applications.

The main contributions of this thesis are:

1. The DVD-R@AgNPs substrate was produced using the CCPD technique, enabling a thin film layer deposition of AgNPs on the PC grating structure from DVD-R. The advantages of DVD-R@AgNPs lie in their ease, practicality, and cost-effectiveness (around USD $0.22), resulting in significant Raman enhancement due to the size grating on its surface and the silver nanoparticles presence.

2. The CCPD technique enables simultaneous deposition and thermochemical diffusion, ensuring excellent adherence of the silver coating to both substrates (DVD-R@AgNPs and PSi@AgNPs). This process allows for the growth of silver nanoparticles with an average size of approximately 50 nm, and these nanoparticles exhibit a regular distribution with a spherical shape. Additionally, the thin-film growth and deposition achieved through this technique offer high efficiency and low processing costs.

3. The enhancement factor (EF) for DVD-R@AgNPs substrate was estimated at 10^5. These values are higher than those attained for silver-based substrates and in the same order of magnitude ($\sim 10^3$ to 10^7) as those reported in the literature using Crystal Violet (CV) as a probe (BARBOSA et al., 2021; BHARATI et al., 2019; ZHANG et al., 2015; HARRAZ et al., 2015).

4. The sensitivity of DVD-R@AgNPs substrate was verified by detecting CV, and GLP, showing values of LOD in the order of magnitude of 10^{-10}, 10^{-7} and 10^{-8} M, respectively. Although the difficulty of detecting commercial GLP-RU, the SERS substrate can recognize trace at 10^{-6} M.

5. The performance of the DVD-R@AgNPs substrate can also be evaluated through quantitative analysis, by studying the changes in Raman band intensity for various concentrations of each analyte. In the CV case, we observed an excellent linear dependence of these variables for three characteristic Raman modes. As for GLPs, we found a reasonable linear response for the same three typical Raman modes.

6. Electrochemical etching is considered one of the best methods for obtaining porous silicon with specific geometry and architecture. Among the factors influencing the formation of pores, the primary determinant is the value of the controlled anode current density, as illustrated in Figure 28. With this fabrication method, we could choose the etching time and current density for PSi@AgNPs substrate, enabling us to detect GLP-RU traces through Raman spectroscopy analysis.

7. The detection limit was measured to be 10^{-12} M for CV as a probe molecule, using PSi@AgNPs active substrate, which demonstrating the reliable SERS effect. This value is two more orders of magnitude of LOD reported in the literature (HARRAZ et al., 2015) using mesoporous silicon fabricated by electrochemical anodization. In addition to the linearity, the EF was used to evaluate the PSi@AgNPs sensing activity with CV as a probe molecule. Its value was estimated at 10^5, the same as the DVD-R@AgNPs substrate.

8. The LOD and LOQ for GLP-RU using the PSi@AgNPs substrate were estimated to be $\sim 10^{-2}$ M, which is four orders of magnitude higher than the LOD for the DVD-R@AgNPs substrate ($\sim 10^{-6}$ M). Therefore, there is a need to enhance the sensitivity of porous silicon, possibly by exploring other parameters for pore formation, to determine the optimal pore diameter range that enhances the Raman signal for GLP-RU. As a result, we can conclude that DVD-R@AgNPs stands out as the best, most versatile, and cost-effective hybrid platform for detecting GLP-RU traces. Considering that a DVD-R (about USD \$0.22) is 100 times cheaper than a silicon wafer (approximately USD \$249).

References

ABDELHAMEED, R. M.; EL-ZAWAHRY, M.; EMAM, H. E. Efficient removal of organophosphorus pesticides from wastewater using polyethylenimine-modified fabrics. *Polymer*, Elsevier, v. 155, p. 225–234, 2018.

ABREU, L. H. P. de et al. The effect of cathodic cage plasma tin deposition on surface properties of conventional plasma nitrided aisi-m2 steel. *Metals*, MDPI, v. 12, n. 6, p. 961, 2022.

ADAWYIA, J. H.; ALWAN, M. A.; ALLAA, A. J. Optimizing of porous silicon morphology for synthesis of silver nanoparticles. *Microporous and Mesoporous Materials*, Elsevier, v. 227, p. 152–160, 2016.

AHMED, R. et al. Tunable fano-resonant metasurfaces on a disposable plastic-template for multimodal and multiplex biosensing. *Advanced Materials*, Wiley Online Library, v. 32, n. 19, p. 1907160, 2020.

AL-RAJAB, A. J.; AMELLAL, S.; SCHIAVON, M. Sorption and leaching of 14c-glyphosate in agricultural soils. *Agronomy for Sustainable Development*, Springer, v. 28, n. 3, p. 419–428, 2008.

AL-SYADI, A. et al. Surface-enhanced raman scattering (sers) active substrate from gold nanoparticle-coated porous silicon for sensitive detection of horseradish peroxidase enzyme. *Materials Chemistry and Physics*, Elsevier, v. 281, p. 125931, 2022.

AL-SYADI, A.; FAISAL, M.; HARRAZ, F. A.; JALALAH, M.; ALSAIARI, M. Immersion-plated palladium nanoparticles onto meso-porous silicon layer as novel sers substrate for sensitive detection of imidacloprid pesticide. *Scientific Reports*, Nature Publishing Group UK London, v. 11, n. 1, p. 9174, 2021.

ALAK, A. M.; VO-DINH, T. Surface-enhanced raman spectrometry of organo phosphorus chemical agents. *Analytical chemistry*, ACS Publications, v. 59, n. 17, p. 2149–2153, 1987.

ALEXANDER, K. D. et al. A high-throughput method for controlled hot-spot fabrication in sers-active gold nanoparticle dimer arrays. *Journal of Raman Spectroscopy: An International Journal for Original Work in all Aspects of Raman Spectroscopy, Including Higher Order Processes, and also Brillouin and Rayleigh Scattering*, Wiley Online Library, v. 40, n. 12, p. 2171–2175, 2009.

ALVES, C. J. et al. Use of cathodic cage in plasma nitriding. *Surface and Coatings Technology*, Elsevier, v. 201, n. 6, p. 2450–2454, 2006.

ALWAN, A. M.; YOUSIF, A. A.; WALI, L. A. The growth of the silver nanoparticles on the mesoporous silicon and macroporous silicon: a comparative study. NISCAIR-CSIR, India, 2017.

ALWAN, A. M.; YOUSIF, A. A.; WALI, L. A. A study on the morphology of the silver nanoparticles deposited on the n-type porous silicon prepared under different illumination types. *Plasmonics*, Springer, v. 13, p. 1191–1199, 2018.

AMARANTE, O. P. d. J.; SANTOS, T. C. R. d.; BRITO, N. M.; RIBEIRO, M. L. Glifosato: propriedades, toxicidade, usos e legislação. *Quimica nova*, SciELO Brasil, v. 25, p. 589–593, 2002.

AMRHEIN, N.; HC, S. et al. The mode of action of the herbicide glyphosate. 1980.

ANSARI, M.; HATAMI, B.; KHAVIDAK, S. S. Toxicity, biodegradability and detection methods of glyphosate; the most used herbicide: a systematic review. *Journal of Environmental Health and Sustainable Development*, 2019.

AVELLA-OLIVER, M.; FERRANDO, V.; MONSORIU, J. A.; PUCHADES, R.; MAQUIEIRA, A. A label-free diffraction-based sensing displacement immunosensor to quantify low molecular weight organic compounds. *Analytica Chimica Acta*, Elsevier, v. 1033, p. 173–179, 2018.

BALAJI, R. et al. Periodic copper microbead array on silver layer for dual mode detection of glyphosate. *OpenNano*, Elsevier, v. 8, p. 100105, 2022.

BALCIUNAS, D.; PLAUSINAITIS, D.; RATAUTAITE, V.; RAMANAVICIENE, A.; RAMANAVICIUS, A. Towards electrochemical surface plasmon resonance sensor based on the molecularly imprinted polypyrrole for glyphosate sensing. *Talanta*, Elsevier, v. 241, p. 123252, 2022.

BARBOSA, I. B. et al. Polysaccharide-based substrate for surface-enhanced raman spectroscopy. *Spectrochimica Acta Part A: Molecular and Biomolecular Spectroscopy*, Elsevier, v. 249, p. 119255, 2021.

BARNES, W. L.; DEREUX, A.; EBBESEN, T. W. Surface plasmon subwavelength optics. *nature*, Nature Publishing Group UK London, v. 424, n. 6950, p. 824–830, 2003.

BARNOR, K.; CATON, J.; MILJKOVIC, D. The role of funding on research and science: The impact of glyphosate herbicides on health and the environment. *Journal of Policy Modeling*, Elsevier, 2023.

BATALLER, R. et al. Glyphosate detection by means of a voltammetric electronic tongue and discrimination of potential interferents. *Sensors*, Molecular Diversity Preservation International (MDPI), v. 12, n. 12, p. 17553–17568, 2012.

BAYLIS, A. D. Why glyphosate is a global herbicide: strengths, weaknesses and prospects. *Pest Management Science: Formerly Pesticide Science*, Wiley Online Library, v. 56, n. 4, p. 299–308, 2000.

BELL, T.; LI, C. Active screen plasma nitriding of materials. *International Heat Treatment and Surface Engineering*, Taylor & Francis, v. 1, n. 1, p. 34–38, 2007.

BENACHOUR, N.; SéRALINI, G.-E. Glyphosate formulations induce apoptosis and necrosis in human umbilical, embryonic, and placental cells. *Chemical research in toxicology*, ACS Publications, v. 22, n. 1, p. 97–105, 2009.

BENBROOK, C. M. Trends in glyphosate herbicide use in the united states and globally. *Environmental Sciences Europe*, SpringerOpen, v. 28, n. 1, p. 1–15, 2016.

BERRY, C. Glyphosate and cancer: the importance of the whole picture. *Pest management science*, Wiley Online Library, v. 76, n. 9, p. 2874–2877, 2020.

BHARATI, M. S. S.; LAKSHMI, P.; BYRAM, C.; RAO, S. V. Commercial dvds loaded with femtosecond laser prepared gold nanoparticles as sers substrates. In: IEEE. *2019 Workshop on Recent Advances in Photonics (WRAP)*. [S.l.], 2019. p. 1–3.

BHARATI, M. S. S.; SOMA, V. R. Flexible sers substrates for hazardous materials detection: recent advances. *Opto-Electronic Advances*, Opto-Electronic Advances, v. 4, n. 11, p. 210048, 2021.

BOHREN, C.; HUFFMAN, D.; KAM, Z. Book-review-absorption and scattering of light by small particles. *Nature*, v. 306, n. 5943, p. 625, 1983.

BOMBARDI, L. M. *Geografia do uso de agrotóxicos no Brasil e conexões com a União Europeia*. [S.l.]: São Paulo, 2017.

BOMCHIL, G.; HALIMAOUI, A.; HERINO, R. Porous silicon: The material and its applications in silicon-on-insulator technologies. *Applied Surface Science*, Elsevier, v. 41, p. 604–613, 1990.

BOUCHARD, D.; ENFIELD, C.; PIWONI, M. Transport processes involving organic chemicals. *Reactions and movement of organic chemicals in soils*, Wiley Online Library, v. 22, p. 349–371, 1989.

BRUGGEN, A. H. V. et al. Environmental and health effects of the herbicide glyphosate. *Science of the total environment*, Elsevier, v. 616, p. 255–268, 2018.

BUTMEE, P.; SAMPHAO, A.; TUMCHARERN, G. Reduced graphene oxide on silver nanoparticle layers-decorated titanium dioxide nanotube arrays as sers-based sensor for glyphosate direct detection in environmental water and soil. *Journal of Hazardous Materials*, Elsevier, v. 437, p. 129344, 2022.

CANAMARES, M. V.; CHENAL, C.; BIRKE, R. L.; LOMBARDI, J. R. Dft, sers, and single-molecule sers of crystal violet. *The Journal of Physical Chemistry C*, ACS Publications, v. 112, n. 51, p. 20295–20300, 2008.

CANARIA, C. A. et al. The effect of surfactants on the reactivity and photophysics of luminescent nanocrystalline porous silicon. *Advanced Functional Materials*, Wiley Online Library, v. 12, n. 8, p. 495–500, 2002.

CANHAM, L. T. Silicon quantum wire array fabrication by electrochemical and chemical dissolution of wafers. *Applied physics letters*, American Institute of Physics, v. 57, n. 10, p. 1046–1048, 1990.

CARRILLO-CARRIóN, C. et al. Aqueous stable gold nanostar/zif-8 nanocomposites for light-triggered release of active cargo inside living cells. *Angewandte Chemie*, Wiley Online Library, v. 131, n. 21, p. 7152–7156, 2019.

CARTIGNY, B. et al. Determination of glyphosate in biological fluids by 1h and 31p nmr spectroscopy. *Forensic science international*, Elsevier, v. 143, n. 2-3, p. 141–145, 2004.

CASTRO, A. S. Avaliação da degradação do herbicida glifosato e o metabólito ampa no solo da bacia do arroio donato–pejuçara (rs). *Endereço para permuta*, v. 12, p. 125, 2012.

CASTRO-GRIJALBA, A. et al. Sers-based molecularly imprinted plasmonic sensor for highly sensitive pah detection. *ACS sensors*, ACS Publications, v. 5, n. 3, p. 693–702, 2020.

CATTANI, D. et al. Mechanisms underlying the neurotoxicity induced by glyphosate-based herbicide in immature rat hippocampus: involvement of glutamate excitotoxicity. *Toxicology*, Elsevier, v. 320, p. 34–45, 2014.

CHANCE, R.; PROCK, A.; SILBEY, R. Lifetime of an emitting molecule near a partially reflecting surface. *The Journal of Chemical Physics*, American Institute of Physics, v. 60, n. 7, p. 2744–2748, 1974.

CHANG, Y.-C.; HUANG, B.-H.; LIN, T.-H. Surface-enhanced raman scattering and fluorescence on gold nanogratings. *Nanomaterials*, MDPI, v. 10, n. 4, p. 776, 2020.

CHEN, H. et al. Simultaneous and ultra-sensitive sers detection of slpi and il-18 for the assessment of donor kidney quality using black phosphorus/gold nanohybrids. *Optics Express*, Optical Society of America, v. 30, n. 2, p. 1452–1465, 2022.

CHEN, Y. et al. Breath analysis based on surface-enhanced raman scattering sensors distinguishes early and advanced gastric cancer patients from healthy persons. *ACS nano*, ACS Publications, v. 10, n. 9, p. 8169–8179, 2016.

CHOWDHURY, J. How the charge transfer (ct) contributions influence the sers spectra of molecules? a retrospective from the view of albrecht's "a" and herzberg-teller contributions. *Applied Spectroscopy Reviews*, Taylor & Francis, v. 50, n. 3, p. 240–260, 2015.

CIALLA, D. et al. Surface-enhanced raman spectroscopy (sers): progress and trends. *Analytical and bioanalytical chemistry*, Springer, v. 403, n. 1, p. 27–54, 2012.

CLEGG, B. S.; STEPHENSON, G. R.; HALL, J. C. Development of an enzyme-linked immunosorbent assay for the detection of dicamba. *Journal of agricultural and food chemistry*, ACS Publications, v. 49, n. 5, p. 2168–2174, 2001.

COLNIțĂ, A. et al. 3d silver metallized nanotrenches fabricated by nanoimprint lithography as flexible sers detection platform. *Spectrochimica Acta Part A: Molecular and Biomolecular Spectroscopy*, Elsevier, v. 276, p. 121232, 2022.

CORBERA, M.; HIDALGO, M.; SALVADO, V.; WIECZOREK, P. Determination of glyphosate and aminomethylphosphonic acid in natural water using the capillary electrophoresis combined with enrichment step. *Analytica chimica acta*, Elsevier, v. 540, n. 1, p. 3–7, 2005.

COSTA, J. C.; ANDO, R. A.; SANT'ANA, A. C.; CORIO, P. Surface-enhanced raman spectroscopy studies of organophosphorous model molecules and pesticides. *Physical chemistry chemical physics*, Royal Society of Chemistry, v. 14, n. 45, p. 15645–15651, 2012.

COUPE, R. H.; KALKHOFF, S. J.; CAPEL, P. D.; GREGOIRE, C. Fate and transport of glyphosate and aminomethylphosphonic acid in surface waters of agricultural basins. *Pest management science*, Wiley Online Library, v. 68, n. 1, p. 16–30, 2012.

CRAIG, A. P.; FRANCA, A. S.; IRUDAYARAJ, J. Surface-enhanced raman spectroscopy applied to food safety. *Annu. Rev. Food Sci. Technol*, v. 4, n. 1, p. 369–380, 2013.

DEY, T. Microplastic pollutant detection by surface enhanced raman spectroscopy (sers): a mini-review. *Nanotechnology for Environmental Engineering*, Springer, p. 1–8, 2022.

DICKSON, S.; MEINHOLD, R.; BEER, I.; KOELMEYER, T. Rapid determination of glyphosate in postmortem specimens using 31p nmr. *Journal of analytical toxicology*, Oxford University Press, v. 12, n. 5, p. 284–286, 1988.

DING, J.; GUO, H.; LIU, W.-w.; ZHANG, W.-w.; WANG, J.-w. Current progress on the detection of glyphosate in environmental samples. *J Sci Appl Biomed*, v. 3, n. 06, p. 88–95, 2015.

DING, S.-Y. et al. Nanostructure-based plasmon-enhanced raman spectroscopy for surface analysis of materials. *Nature Reviews Materials*, Nature Publishing Group, v. 1, n. 6, p. 1–16, 2016.

DING, S.-Y.; YOU, E.-M.; TIAN, Z.-Q.; MOSKOVITS, M. Electromagnetic theories of surface-enhanced raman spectroscopy. *Chemical Society Reviews*, Royal Society of Chemistry, v. 46, n. 13, p. 4042–4076, 2017.

DO, M. H. et al. Chitosan-based nanocomposites for glyphosate detection using surface plasmon resonance sensor. *Sensors*, MDPI, v. 20, n. 20, p. 5942, 2020.

DOMENICI, F. et al. Engineering microscale two-dimensional gold nanoparticle cluster arrays for advanced raman sensing: an afm study. *Colloids and surfaces A: Physicochemical and engineering aspects*, Elsevier, v. 498, p. 168–175, 2016.

DONG, J. et al. Nanoscale flexible ag grating/aunps self-assembly hybrid for ultra-sensitive sensors. *Nanotechnology*, IOP Publishing, v. 32, n. 15, p. 155603, 2021.

DONG, J.; ZHANG, Z.; ZHENG, H.; SUN, M. Recent progress on plasmon-enhanced fluorescence. *Nanophotonics*, De Gruyter, v. 4, n. 4, p. 472–490, 2015.

DUAN, J. et al. Inkjet printed silver nanoparticles on hydrophobic papers for efficient detection of thiram. *Spectrochimica Acta Part A: Molecular and Biomolecular Spectroscopy*, Elsevier, v. 243, p. 118811, 2020.

EBERBACH, P. Applying non-steady-state compartmental analysis to investigate the simultaneous degradation of soluble and sorbed glyphosate (n-(phosphonomethyl) glycine) in four soils. *Pesticide Science*, Wiley Online Library, v. 52, n. 3, p. 229–240, 1998.

EMONDS-ALT, G. et al. Development and validation of an integrated microfluidic device with an in-line surface enhanced raman spectroscopy (sers) detection of glyphosate in drinking water. *Talanta*, Elsevier, v. 249, p. 123640, 2022.

ENFIELD, C.; YATES, S. Organic chemical transport to groundwater. *Pesticides in the Soil Environment: Processes, Impacts and Modeling*, Wiley Online Library, v. 2, p. 271–302, 1990.

ERNST, F. et al. Occurrence of pesticide residues in fish from south american rainfed agroecosystems. *Science of the total environment*, Elsevier, v. 631, p. 169–179, 2018.

ETCHEGOIN, P. G.; RU, E. L. A perspective on single molecule sers: current status and future challenges. *Physical Chemistry Chemical Physics*, Royal Society of Chemistry, v. 10, n. 40, p. 6079–6089, 2008.

FANG, X. et al. Hierarchically ordered silicon metastructures from improved self-assembly-based nanosphere lithography. *ACS applied materials & interfaces*, ACS Publications, v. 12, n. 10, p. 12345–12352, 2020.

FASOLATO, C. *Surface enhanced Raman spectroscopy for biophysical applications: using plasmonic nanoparticle assemblies*. [S.l.]: Springer, 2018.

FASOLATO, C. et al. Dimensional scale effects on surface enhanced raman scattering efficiency of self-assembled silver nanoparticle clusters. *Applied Physics Letters*, AIP Publishing, v. 105, n. 7, 2014.

FATEIXA, S.; NOGUEIRA, H. I.; TRINDADE, T. Surface-enhanced raman scattering spectral imaging for the attomolar range detection of crystal violet in contaminated water. *ACS omega*, ACS Publications, v. 3, n. 4, p. 4331–4341, 2018.

FEIS, A. et al. Surface-enhanced raman scattering of glyphosate on dispersed silver nanoparticles: A reinterpretation based on model molecules. *Vibrational spectroscopy*, Elsevier, v. 108, p. 103061, 2020.

FERRARO, J. R. *Introductory raman spectroscopy*. [S.l.]: Elsevier, 2003.

FIERRO-MERCADO, P. M.; HERNÁNDEZ-RIVERA, S. P. Highly sensitive filter paper substrate for sers trace explosives detection. *International Journal of Spectroscopy*, Hindawi, v. 2012, 2012.

FREIRE, C. da S. et al. Application of a smartphone-based spr platform for glyphosate detection. In: IEEE. *2019 IEEE sensors applications symposium (SAS)*. [S.l.], 2019. p. 1–6.

GALLO, S. C.; DONG, H. On the fundamental mechanisms of active screen plasma nitriding. *Vacuum*, Elsevier, v. 84, n. 2, p. 321–325, 2009.

GANDHI, K. et al. Exposure risk and environmental impacts of glyphosate: highlights on the toxicity of herbicide co-formulants. *Environmental Challenges*, Elsevier, v. 4, p. 100149, 2021.

GASNIER, C. et al. Glyphosate-based herbicides are toxic and endocrine disruptors in human cell lines. *Toxicology*, Elsevier, v. 262, n. 3, p. 184–191, 2009.

GE, D.; ZHAO, C.; SHI, J.; QIAN, P.; ZHANG, L. Porous silicon composite silver dendrite irregular nanoparticles with high sers performance. *MRS Communications*, Springer, v. 12, n. 5, p. 856–863, 2022.

GE, K.; HU, Y.; LI, G. Recent progress on solid substrates for surface-enhanced raman spectroscopy analysis. *Biosensors*, MDPI, v. 12, n. 11, p. 941, 2022.

GE, K.; HU, Y.; ZHENG, Y.; JIANG, P.; LI, G. Aptamer/derivatization-based surface-enhanced raman scattering membrane assembly for selective analysis of melamine and formaldehyde in migration of melamine kitchenware. *Talanta*, Elsevier, v. 235, p. 122743, 2021.

GELLINI, C. et al. Nanopatterned ag substrates for sers spectroscopy. *Physical Chemistry Chemical Physics*, Royal Society of Chemistry, v. 10, n. 31, p. 4555–4558, 2008.

GEORGES, J. Tc plasma nitriding. *Heat Treat. Met.*, v. 28, p. 33, 2001.

GERECKE, A. C. et al. Sources of pesticides in surface waters in switzerland: pesticide load through waste water treatment plants—-current situation and reduction potential. *Chemosphere*, Elsevier, v. 48, n. 3, p. 307–315, 2002.

GIALLONGO, G. et al. Silver nanoparticle arrays on a dvd-derived template: an easy&cheap sers substrate. *Plasmonics*, Springer, v. 6, n. 4, p. 725–733, 2011.

GIL, P. M.; LAGUARDA-MIRO, N.; CAMINO, J. S.; PERIS, R. M. Glyphosate detection with ammonium nitrate and humic acids as potential interfering substances by pulsed voltammetry technique. *Talanta*, Elsevier, v. 115, p. 702–705, 2013.

GLOZIER, N. E. et al. Occurrence of glyphosate and acidic herbicides in select urban rivers and streams in canada, 2007. *Environmental Science and Pollution Research*, Springer, v. 19, n. 3, p. 821–834, 2012.

GOEL, P.; SINGH, K.; SINGH, J. Polarization dependent diffraction from anisotropic ag nanorods grown on dvd grating templates by oblique angle deposition. *RSC Advances*, The Royal Society of Chemistry, v. 4, n. 22, p. 11130–11135, 2014.

GONZáLEZ-MARTíNEZ, M. et al. Glyphosate immunosensor. application for water and soil analysis. *Analytical Chemistry*, ACS Publications, v. 77, n. 13, p. 4219–4227, 2005.

GREEN, F. J. The sigma-aldrich handbook of stains, dyes and indicators, aldrich chemical company. *Inc. Milwaukee, Wisconsin*, 1990.

GUI, Y.-x.; FAN, X.-n.; WANG, H.-m.; WANG, G. et al. Glyphosate induced cell death through apoptotic and autophagic mechanisms. *Neurotoxicology and teratology*, Elsevier, v. 34, n. 3, p. 344–349, 2012.

GUILHERME, S.; SANTOS, M.; BARROSO, C.; GAIVÃO, I.; PACHECO, M. Differential genotoxicity of roundup® formulation and its constituents in blood cells of fish (anguilla anguilla): considerations on chemical interactions and dna damaging mechanisms. *Ecotoxicology*, Springer, v. 21, n. 5, p. 1381–1390, 2012.

GUNNARSSON, L. et al. Interparticle coupling effects in nanofabricated substrates for surface-enhanced raman scattering. *Applied Physics Letters*, American Institute of Physics, v. 78, n. 6, p. 802–804, 2001.

GUO, P. et al. Plasmonic core–shell nanoparticles for sers detection of the pesticide thiram: size-and shape-dependent raman enhancement. *Nanoscale*, Royal Society of Chemistry, v. 7, n. 7, p. 2862–2868, 2015.

HABEKOST, A. Spectroscopic and electrochemical investigations of n-(phosphonomethyl) glycine (glyphosate) and (aminomethyl) phosphonic acid (ampa). *Journal of Chemical Education*, v. 3, p. 134–140, 2015.

HAKONEN, A.; ANDERSSON, P. O.; SCHMIDT, M. S.; RINDZEVICIUS, T.; KÄLL, M. Explosive and chemical threat detection by surface-enhanced raman scattering: A review. *Analytica chimica acta*, Elsevier, v. 893, p. 1–13, 2015.

HALAS, N. J.; LAL, S.; CHANG, W.-S.; LINK, S.; NORDLANDER, P. Plasmons in strongly coupled metallic nanostructures. *Chemical reviews*, ACS Publications, v. 111, n. 6, p. 3913–3961, 2011.

HAN, X. X.; JI, W.; ZHAO, B.; OZAKI, Y. Semiconductor-enhanced raman scattering: Active nanomaterials and applications. *Nanoscale*, Royal Society of Chemistry, v. 9, n. 15, p. 4847–4861, 2017.

HAN, X. X.; RODRIGUEZ, R. S.; HAYNES, C. L.; OZAKI, Y.; ZHAO, B. Surface-enhanced raman spectroscopy. *Nature Reviews Methods Primers*, Nature Publishing Group, v. 1, n. 1, p. 1–17, 2022.

HANSKE, C. et al. Solvent-assisted self-assembly of gold nanorods into hierarchically organized plasmonic mesostructures. *ACS applied materials & interfaces*, ACS Publications, v. 11, n. 12, p. 11763–11771, 2019.

HAO, E.; SCHATZ, G. C. Electromagnetic fields around silver nanoparticles and dimers. *The Journal of chemical physics*, American Institute of Physics, v. 120, n. 1, p. 357–366, 2004.

HARRAZ, F. A. Impregnation of porous silicon with conducting polymers. *physica status solidi c*, Wiley Online Library, v. 8, n. 6, p. 1883–1887, 2011.

HARRAZ, F. A. Synthesis and surface properties of magnetite (fe3o4) nanoparticles infiltrated into porous silicon template. *Applied surface science*, Elsevier, v. 287, p. 203–210, 2013.

HARRAZ, F. A. et al. A capacitive chemical sensor based on porous silicon for detection of polar and non-polar organic solvents. *Applied surface science*, Elsevier, v. 307, p. 704–711, 2014.

HARRAZ, F. A. et al. Surface-enhanced raman scattering (sers)-active substrates from silver plated-porous silicon for detection of crystal violet. *Applied Surface Science*, Elsevier, v. 331, p. 241–247, 2015.

HAYNES, C. L. et al. Nanoparticle optics: the importance of radiative dipole coupling in two-dimensional nanoparticle arrays. *The Journal of Physical Chemistry B*, ACS Publications, v. 107, n. 30, p. 7337–7342, 2003.

HERINO, R.; BOMCHIL, G.; BARLA, K.; BERTRAND, C.; GINOUX, J. L. Porosity and pore size distributions of porous silicon layers. *Journal of the electrochemical society*, IOP Publishing, v. 134, n. 8, p. 1994, 1987.

HERMANSEN, C. et al. Predicting glyphosate sorption across new zealand pastoral soils using basic soil properties or vis–nir spectroscopy. *Geoderma*, Elsevier, v. 360, p. 114009, 2020.

HOGENDOORN, E.; OSSENDRIJVER, F.; DIJKMAN, E.; BAUMANN, R. Rapid determination of glyphosate in cereal samples by means of pre-column derivatisation with 9-fluorenylmethyl chloroformate and coupled-column liquid chromatography with fluorescence detection. *Journal of Chromatography A*, Elsevier, v. 833, n. 1, p. 67–73, 1999.

HOLANDA, R. O.; SILVA, C. B. da; VASCONCELOS, D. L.; FREIRE, P. T. High pressure raman spectra and dft calculation of glyphosate. *Spectrochimica Acta Part A: Molecular and Biomolecular Spectroscopy*, Elsevier, v. 242, p. 118745, 2020.

HOU, R.; PANG, S.; HE, L. In situ sers detection of multi-class insecticides on plant surfaces. *Analytical Methods*, Royal Society of Chemistry, v. 7, n. 15, p. 6325–6330, 2015.

HU, J.-Y.; CHEN, C.-L.; LI, J.-Z. A simple method for the determination of glyphosate residues in soil by capillary gas chromatography with nitrogen phosphorus. *Journal of Analytical Chemistry*, Springer, v. 63, n. 4, p. 371–375, 2008.

HU, Y.; LIAO, J.; WANG, D.; LI, G. Fabrication of gold nanoparticle-embedded metal–organic framework for highly sensitive surface-enhanced raman scattering detection. *Analytical chemistry*, ACS Publications, v. 86, n. 8, p. 3955–3963, 2014.

IARC. International Agency for Research on Cancer. evaluation of five organophosphate insecticides and herbicides. IARC monographs. vol. 112. *World Health Organization, Lyon, France*, 2015.

INGARAMO, P.; ALARCÓN, R.; TORO, M. Muñoz-de; LUQUE, E. H. Are glyphosate and glyphosate-based herbicides endocrine disruptors that alter female fertility? *Molecular and Cellular Endocrinology*, Elsevier, v. 518, p. 110934, 2020.

ITOH, T.; YOSHIDA, K.-i.; TAMARU, H.; BIJU, V.; ISHIKAWA, M. Experimental demonstration of the electromagnetic mechanism underlying surface enhanced raman scattering using single nanoparticle spectroscopy. *Journal of Photochemistry and Photobiology A: Chemistry*, Elsevier, v. 219, n. 2-3, p. 167–179, 2011.

JABBAR, A. A.; ALWAN, A. M.; HAIDER, A. J. Modifying and fine controlling of silver nanoparticle nucleation sites and sers performance by double silicon etching process. *Plasmonics*, Springer, v. 13, n. 4, p. 1171–1182, 2018.

JACOB, G. et al. Metabolism of glyphosate in pseudomonas sp. strain lbr. *Applied and environmental microbiology*, Am Soc Microbiol, v. 54, n. 12, p. 2953–2958, 1988.

JENSEN, L.; AIKENS, C. M.; SCHATZ, G. C. Electronic structure methods for studying surface-enhanced raman scattering. *Chemical Society Reviews*, Royal Society of Chemistry, v. 37, n. 5, p. 1061–1073, 2008.

JI-YE, H.; DIAN-YING, Z.; JUN, N.; CHANG-LONG, C.; JIAN-ZHONG, L. Determination of glyphosate residues in soil and apple by capillary gas chromatography with nitrogen-phosphorus detection. *Chinese Journal of Pesticide Science*, Journal of Pesticide Science, v. 9, n. 3, p. 285–290, 2007.

JIANG, J.; OU-YANG, L.; ZHU, L.; ZOU, J.; TANG, H. Novel one-pot fabrication of lab-on-a-bubble@ ag substrate without coupling-agent for surface enhanced raman scattering. *Scientific Reports*, Nature Publishing Group UK London, v. 4, n. 1, p. 3942, 2014.

JIANG, Y. et al. Surface plasmon enhanced fluorescence of dye molecules on metal grating films. *The Journal of Physical Chemistry C*, ACS Publications, v. 115, n. 25, p. 12636–12642, 2011.

JONGE, H. D.; JONGE, L. D.; JACOBSEN, O.; YAMAGUCHI, T.; MOLDRUP, P. Glyphosate sorption in soils of different ph and phosphorus content. *Soil Science*, LWW, v. 166, n. 4, p. 230–238, 2001.

KAHL, M.; VOGES, E. Analysis of plasmon resonance and surface-enhanced raman scattering on periodic silver structures. *Physical Review B*, APS, v. 61, n. 20, p. 14078, 2000.

KAPLAN, B. et al. Tuning optical discs for plasmonic applications. *Plasmonics*, Springer, v. 4, n. 3, p. 237–243, 2009.

KEATING, M.; CHEN, Y.; LARMOUR, I.; FAULDS, K.; GRAHAM, D. Growth and surface-enhanced raman scattering of ag nanoparticle assembly in agarose gel. *Measurement Science and Technology*, IOP Publishing, v. 23, n. 8, p. 084006, 2012.

KELLY, K. L.; CORONADO, E.; ZHAO, L. L.; SCHATZ, G. C. The optical properties of metal nanoparticles: the influence of size, shape, and dielectric environment. *The Journal of Physical Chemistry B*, v. 107, n. 3, p. 668–677, 2003.

KERESZTURY, G. Raman spectroscopy: Theory. *Handbook of vibrational spectroscopy*, Wiley Online Library, 2006.

KHENIFI, A. et al. Glyphosate and glufosinate detection at electrogenerated nial-ldh thin films. *Analytica Chimica Acta*, Elsevier, v. 654, n. 2, p. 97–102, 2009.

KHINEVICH, N. et al. Porous silicon-a versatile platform for mass-production of ultrasensitive sers-active substrates. *Microporous and Mesoporous Materials*, Elsevier, v. 323, p. 111204, 2021.

KHROLENKO, M. V.; WIECZOREK, P. P. Determination of glyphosate and its metabolite aminomethylphosphonic acid in fruit juices using supported-liquid membrane preconcentration method with high-performance liquid chromatography and uv detection after derivatization with p-toluenesulphonyl chloride. *Journal of Chromatography A*, Elsevier, v. 1093, n. 1-2, p. 111–117, 2005.

KIM, A.; BARCELO, S. J.; LI, Z. Sers-based pesticide detection by using nanofinger sensors. *Nanotechnology*, IOP Publishing, v. 26, n. 1, p. 015502, 2014.

KIM, K.-H.; KABIR, E.; JAHAN, S. A. Exposure to pesticides and the associated human health effects. *Science of the total environment*, Elsevier, v. 575, p. 525–535, 2017.

KIM, S. et al. Label-free surface-enhanced raman spectroscopy biosensor for on-site breast cancer detection using human tears. *ACS applied materials & interfaces*, ACS Publications, v. 12, n. 7, p. 7897–7904, 2020.

KNEIPP, K. Chemical contribution to sers enhancement: an experimental study on a series of polymethine dyes on silver nanoaggregates. *The Journal of Physical Chemistry C*, ACS Publications, v. 120, n. 37, p. 21076–21081, 2016.

KNEIPP, K.; MOSKOVITS, M.; KNEIPP, H. *Surface-enhanced Raman scattering: physics and applications*. [S.l.]: Springer Science & Business Media, 2006.

KNEIPP, K.; OZAKI, Y.; TIAN, Z.-Q. Recent developments in plasmon-supported raman spectroscopy: 45 years of enhanced raman signals. World Scientific, 2017.

KNEIPP, K. et al. Single molecule detection using surface-enhanced raman scattering (sers). *Physical review letters*, APS, v. 78, n. 9, p. 1667, 1997.

KNISS, A. R. Long-term trends in the intensity and relative toxicity of herbicide use. *Nature communications*, Nature Publishing Group, v. 8, n. 1, p. 1–7, 2017.

KOCHYLAS, I. et al. Improved surface-enhanced-raman scattering sensitivity using si nanowires/silver nanostructures by a single step metal-assisted chemical etching. *Nanomaterials*, MDPI, v. 11, n. 7, p. 1760, 2021.

KOSOVIĆ, M. et al. Porous silicon covered with silver nanoparticles as surface-enhanced raman scattering (sers) substrate for ultra-low concentration detection. *Applied spectroscopy*, SAGE Publications Sage UK: London, England, v. 69, n. 12, p. 1417–1424, 2015.

KRISHNAN, R.; SHANKAR, R. Raman effect: History of the discovery. *Journal of Raman Spectroscopy*, Wiley Online Library, v. 10, n. 1, p. 1–8, 1981.

KUDZIN, Z. H.; GRALAK, D. K.; ANDRIJEWSKI, G.; DRABOWICZ, J.; ŁUCZAK, J. Simultaneous analysis of biologically active aminoalkanephosphonic acids. *Journal of Chromatography A*, Elsevier, v. 998, n. 1-2, p. 183–199, 2003.

KUDZIN, Z. H.; GRALAK, D. K.; DRABOWICZ, J.; ŁUCZAK, J. Novel approach for the simultaneous analysis of glyphosate and its metabolites. *Journal of Chromatography A*, Elsevier, v. 947, n. 1, p. 129–141, 2002.

KUMAR, A.; SANTHANAM, V. Paper swab based sers detection of non-permitted colourants from dals and vegetables using a portable spectrometer. *Analytica chimica acta*, Elsevier, v. 1090, p. 106–113, 2019.

KUMAR, S.; DOI, Y.; NAMURA, K.; SUZUKI, M. Plasmonic nanoslit arrays fabricated by serial bideposition: Optical and surface-enhanced raman scattering study. *ACS Applied Bio Materials*, ACS Publications, v. 3, n. 5, p. 3226–3235, 2020.

KUMAR, S.; GOEL, P.; SINGH, J. P. Flexible and robust sers active substrates for conformal rapid detection of pesticide residues from fruits. *Sensors and Actuators B: Chemical*, Elsevier, v. 241, p. 577–583, 2017.

LANDAU, L. D.; M, L. E. *Mechanics*. [S.l.]: Elsevier, 2004.

LEE, C. H.; TIAN, L.; SINGAMANENI, S. based sers swab for rapid trace detection on real-world surfaces. *ACS applied materials & interfaces*, ACS Publications, v. 2, n. 12, p. 3429–3435, 2010.

LEE, D. et al. Quantitative analysis of methyl parathion pesticides in a polydimethylsiloxane microfluidic channel using confocal surface-enhanced raman spectroscopy. *Applied spectroscopy*, Society for Applied Spectroscopy, v. 60, n. 4, p. 373–377, 2006.

LEE, S. et al. Fast and sensitive trace analysis of malachite green using a surface-enhanced raman microfluidic sensor. *Analytica chimica acta*, Elsevier, v. 590, n. 2, p. 139–144, 2007.

LEE, Y.-H.; DAI, S.; YOUNG, J. P. Silver-doped sol–gel films as the substrate for surface-enhanced raman scattering. *Journal of Raman Spectroscopy*, Wiley Online Library, v. 28, n. 8, p. 635–639, 1997.

LEHMANN, V.; GÖSELE, U. Porous silicon formation: A quantum wire effect. *Applied Physics Letters*, American Institute of Physics, v. 58, n. 8, p. 856–858, 1991.

LEORDEAN, C. et al. Fabrication of highly active and cost effective sers plasmonic substrates by electrophoretic deposition of gold nanoparticles on a dvd template. *Applied Surface Science*, Elsevier, v. 349, p. 190–195, 2015.

LI, C. Active screen plasma nitriding–an overview. *Surface Engineering*, Taylor & Francis, v. 26, n. 1-2, p. 135–141, 2010.

LI, C.; BELL, T.; DONG, H. A study of active screen plasma nitriding. *Surface Engineering*, Taylor & Francis, v. 18, n. 3, p. 174–181, 2002.

LI, C.; GEORGES, J.; LI, X.-Y. Active screen plasma nitriding of austenitic stainless steel. *Surface Engineering*, Taylor & Francis, v. 18, n. 6, p. 453–457, 2002.

LI, J. et al. Enhancement of the photoresponse of monolayer mos2 photodetectors induced by a nanoparticle grating. *ACS applied materials & interfaces*, ACS Publications, v. 12, n. 7, p. 8429–8436, 2020.

LI, J.; YAN, H.; TAN, X.; LU, Z.; HAN, H. Cauliflower-inspired 3d sers substrate for multiple mycotoxins detection. *Analytical chemistry*, ACS Publications, v. 91, n. 6, p. 3885–3892, 2019.

LI, J. F. et al. Shell-isolated nanoparticle-enhanced raman spectroscopy. *nature*, Nature Publishing Group, v. 464, n. 7287, p. 392–395, 2010.

LI, J. F. et al. Surface analysis using shell-isolated nanoparticle-enhanced raman spectroscopy. *Nature protocols*, Nature Publishing Group, v. 8, n. 1, p. 52–65, 2013.

LI, K.; STOCKMAN, M. I.; BERGMAN, D. J. Self-similar chain of metal nanospheres as an efficient nanolens. *Physical review letters*, APS, v. 91, n. 22, p. 227402, 2003.

LI, L.; YANG, S.; DUAN, J.; HUANG, L.; XIAO, G. Fabrication and sers performance of silver nanoarrays by inkjet printing silver nanoparticles ink on the gratings of compact disc recordable. *Spectrochimica Acta Part A: Molecular and Biomolecular Spectroscopy*, Elsevier, v. 225, p. 117598, 2020.

LIBÓRIO, M. et al. Surface modification of m2 steel by combination of cathodic cage plasma deposition and magnetron sputtered mos2-tin multilayer coatings. *Surface and coatings technology*, Elsevier, v. 384, p. 125327, 2020.

LIM, S.-H. et al. Individually silica-embedded gold nanorod superlattice for high thermal and solvent stability and recyclable sers application. *Advanced Materials Interfaces*, Wiley Online Library, v. 6, n. 21, p. 1900986, 2019.

LIMA, I. B.; BOËCHAT, I. G.; GÜCKER, B. Glifosato no brasil. *Caderno de Geografia*, v. 31, n. 1, p. 90–90, 2021.

LIN, X.-M.; CUI, Y.; XU, Y.-H.; REN, B.; TIAN, Z.-Q. Surface-enhanced raman spectroscopy: substrate-related issues. *Analytical and bioanalytical chemistry*, Springer, v. 394, p. 1729–1745, 2009.

LING, X. et al. Lighting up the raman signal of molecules in the vicinity of graphene related materials. *Accounts of chemical research*, ACS Publications, v. 48, n. 7, p. 1862–1870, 2015.

LIU, C. et al. A surface-enhanced raman scattering (sers)-active optical fiber sensor based on a three-dimensional sensing layer. *Sensing and Bio-Sensing Research*, Elsevier, v. 1, p. 8–14, 2014.

LIU, H. et al. Single molecule detection from a large-scale sers-active au79ag21 substrate. *Scientific reports*, Nature Publishing Group, v. 1, n. 1, p. 1–5, 2011.

LIU, R. M. et al. The ultratrace detection of crystal violet using surface enhanced raman scattering on colloidal ag nanoparticles prepared by electrolysis. *Chinese Chemical Letters*, Elsevier, v. 20, n. 6, p. 711–715, 2009.

LIU, Y.; MA, H.; HAN, X. X.; ZHAO, B. Metal–semiconductor heterostructures for surface-enhanced raman scattering: synergistic contribution of plasmons and charge transfer. *Materials Horizons*, Royal Society of Chemistry, v. 8, n. 2, p. 370–382, 2021.

LOMBARDI, J. R. The theory of surface-enhanced raman scattering on semiconductor nanoparticles; toward the optimization of sers sensors. *Faraday discussions*, Royal Society of Chemistry, v. 205, p. 105–120, 2017.

LOMBARDI, J. R.; BIRKE, R. L. Theory of surface-enhanced raman scattering in semiconductors. *The Journal of Physical Chemistry C*, ACS Publications, v. 118, n. 20, p. 11120–11130, 2014.

LOMBARDI, J. R.; BIRKE, R. L.; LU, T.; XU, J. Charge-transfer theory of surface enhanced raman spectroscopy: Herzberg–teller contributions. *The Journal of chemical physics*, American Institute of Physics, v. 84, n. 8, p. 4174–4180, 1986.

LONG, D. A.; LONG, D. *The Raman effect: a unified treatment of the theory of Raman scattering by molecules*. [S.l.]: Wiley Chichester, 2002.

LONG, L. et al. Localized surface plasmon resonance improved lasing performance of ag nanoparticles/organic dye random laser. *Journal of Alloys and Compounds*, Elsevier, v. 693, p. 876–881, 2017.

LOPES, R. F. et al. Tio2 anti-corrosive thin films on duplex stainless steel grown using cathodic cage plasma deposition. *Surface and Coatings Technology*, Elsevier, v. 347, p. 136–141, 2018.

LÓPEZ-CASTAÑOS, K. A. et al. Indirect quantification of glyphosate by sers using an incubation process with hemin as the reporter molecule: A contribution to signal amplification mechanism. *Frontiers in chemistry*, Frontiers Media SA, v. 8, p. 612076, 2020.

LOUWAARS, N.; MINDERHOUD, M. When a law is not enough: biotechnology patents in practice. 2001.

LU, H.; GAN, X.; MAO, D.; ZHAO, J. Graphene-supported manipulation of surface plasmon polaritons in metallic nanowaveguides. *Photonics Research*, Optica Publishing Group, v. 5, n. 3, p. 162–167, 2017.

MA, J. et al. Sensitive sers assay for glyphosate based on the prevention of l-cysteine inhibition of a au–pt nanozyme. *Analyst*, Royal Society of Chemistry, v. 146, n. 3, p. 956–963, 2021.

MAHMOUD, M. A.; EL-SAYED, M. A. Different plasmon sensing behavior of silver and gold nanorods. *The Journal of Physical Chemistry Letters*, ACS Publications, v. 4, n. 9, p. 1541–1545, 2013.

MAIER, S. A.; BRONGERSMA, M. L.; KIK, P. G.; ATWATER, H. A. Observation of near-field coupling in metal nanoparticle chains using far-field polarization spectroscopy. *Physical Review B*, APS, v. 65, n. 19, p. 193408, 2002.

MAIER, S. A. et al. *Plasmonics: fundamentals and applications*. [S.l.]: Springer, 2007.

MARC, J.; MULNER-LORILLON, O.; BELLé, R. Glyphosate-based pesticides affect cell cycle regulation. *Biology of the Cell*, Elsevier, v. 96, n. 3, p. 245–249, 2004.

MARTINS-GOMES, C.; SILVA, T. L.; ANDREANI, T.; SILVA, A. M. Glyphosate vs. glyphosate-based herbicides exposure: a review on their toxicity. *Journal of Xenobiotics*, MDPI, v. 12, n. 1, p. 21–40, 2022.

MARTINS, N. C.; FATEIXA, S.; FERNANDES, T.; NOGUEIRA, H. I.; TRINDADE, T. Inkjet printing of ag and polystyrene nanoparticle emulsions for the one-step fabrication of hydrophobic paper-based surface-enhanced raman scattering substrates. *ACS Applied Nano Materials*, ACS Publications, v. 4, n. 5, p. 4484–4495, 2021.

MCNAY, G.; EUSTACE, D.; SMITH, W. E.; FAULDS, K.; GRAHAM, D. Surface-enhanced raman scattering (sers) and surface-enhanced resonance raman scattering (serrs): a review of applications. *Applied spectroscopy*, SAGE Publications Sage UK: London, England, v. 65, n. 8, p. 825–837, 2011.

MERáS, I. D.; DíAZ, T. G.; FRANCO, M. A. Simultaneous fluorimetric determination of glyphosate and its metabolite, aminomethylphosphonic acid, in water, previous derivatization with nbd-cl and by partial least squares calibration (pls). *Talanta*, Elsevier, v. 65, n. 1, p. 7–14, 2005.

MHLANGA, N.; DOMFE, T.; SKEPU, A. Fabrication of surface enhanced raman spectroscopy substrates on solid supports. *Applied Surface Science*, Elsevier, v. 476, p. 1108–1117, 2019.

MICHAELS, A. M.; NIRMAL, M.; BRUS, L. Surface enhanced raman spectroscopy of individual rhodamine 6g molecules on large ag nanocrystals. *Journal of the American Chemical Society*, ACS Publications, v. 121, n. 43, p. 9932–9939, 1999.

MIKAC, L.; RIGÓ, I.; ŠKRABIĆ, M.; IVANDA, M.; VERES, M. Comparison of glyphosate detection by surface-enhanced raman spectroscopy using gold and silver nanoparticles at different laser excitations. *Molecules*, MDPI, v. 27, n. 18, p. 5767, 2022.

MORAES, R. F. de. *Agrotóxicos no Brasil: padrões de uso, política da regulação e prevenção da captura regulatória*. [S.l.], 2019.

MORAM, S. S. B.; BYRAM, C.; SOMA, V. R. Femtosecond laser patterned silicon embedded with gold nanostars as a hybrid sers substrate for pesticide detection. *RSC advances*, Royal Society of Chemistry, v. 13, n. 4, p. 2620–2630, 2023.

MOROVVATI, B.; MALEKFAR, R. Surface enhanced raman scattering of crystal violet with low concentrations using self-assembled silver and gold-silver core-shell nanoparticles. *International Journal of Optics and Photonics*, International Journal of Optics and Photonics, v. 13, n. 2, p. 89–96, 2019.

MOSKOVITS, M. Surface roughness and the enhanced intensity of raman scattering by molecules adsorbed on metals. *The Journal of Chemical Physics*, American Institute of Physics, v. 69, n. 9, p. 4159–4161, 1978.

MOSKOVITS, M. Persistent misconceptions regarding sers. *Physical Chemistry Chemical Physics*, Royal Society of Chemistry, v. 15, n. 15, p. 5301–5311, 2013.

MUJAWAR, S.; UTTURE, S. C.; FONSECA, E.; MATARRITA, J.; BANERJEE, K. Validation of a gc–ms method for the estimation of dithiocarbamate fungicide residues and safety evaluation of mancozeb in fruits and vegetables. *Food chemistry*, Elsevier, v. 150, p. 175–181, 2014.

MUNIRA, S.; FARENHORST, A.; FLATEN, D.; GRANT, C. Phosphate fertilizer impacts on glyphosate sorption by soil. *Chemosphere*, Elsevier, v. 153, p. 471–477, 2016.

MUÑOZ, J. P.; BLEAK, T. C.; CALAF, G. M. Glyphosate and the key characteristics of an endocrine disruptor: A review. *Chemosphere*, Elsevier, v. 270, p. 128619, 2021.

NAEEM, M. et al. Improved nitriding capability of nonalloyed steels assisted with active screen plasma treatment. *Surface Review and Letters*, World Scientific, v. 27, n. 03, p. 1950118, 2020.

NAEEM, M. et al. Novel duplex cathodic cage plasma nitriding of non-alloyed steel using aluminum and austenite steel cathodic cages. *Journal of Alloys and Compounds*, Elsevier, v. 721, p. 307–311, 2017.

NAFISAH, S. et al. Improved sensitivity and selectivity of direct localized surface plasmon resonance sensor using gold nanobipyramids for glyphosate detection. *IEEE Sensors Journal*, IEEE, v. 20, n. 5, p. 2378–2389, 2019.

NAFISAH, S. et al. Gold nanobipyramids as lpsr sensing materials for glyphosate detection: Surface density and aspect ratio effect. *IEEE Sensors Journal*, IEEE, v. 22, n. 19, p. 18479–18485, 2022.

NAPOLI, M.; CECCHI, S.; ZANCHI, C. A.; ORLANDINI, S. Leaching of glyphosate and aminomethylphosphonic acid through silty clay soil columns under outdoor conditions. *Journal of environmental quality*, Wiley Online Library, v. 44, n. 5, p. 1667–1673, 2015.

NATAN, M. J. Concluding remarks surface enhanced raman scattering. *Faraday Discussions*, Royal Society of Chemistry, v. 132, p. 321–328, 2006.

NCBI. National Center for Biotechnology Information. PubChem Compound Summary for CID 3496, Glyphosate. 2020.

N'GOM, M. et al. Single particle plasmon spectroscopy of silver nanowires and gold nanorods. *Nano letters*, ACS Publications, v. 8, n. 10, p. 3200–3204, 2008.

NGUYEN, N. A.; NGO, G. L. et al. A simple and rapid method to produce sers substrates using au nanoparticles prepared by laser ablation and dvd template. *Journal of Electronic Materials*, Springer, v. 49, n. 1, p. 311–317, 2020.

NGUYEN, T. H.; ZHANG, Z.; MUSTAPHA, A.; LI, H.; LIN, M. Use of graphene and gold nanorods as substrates for the detection of pesticides by surface enhanced raman spectroscopy. *Journal of Agricultural and Food Chemistry*, ACS Publications, v. 62, n. 43, p. 10445–10451, 2014.

NGUYEN, T. V. et al. Quasi-three-dimension structured surface-enhanced raman scattering substrates based on silver nanoparticles/porous silicon hybrid. 2022.

NOORI, J. S.; MORTENSEN, J.; GETO, A. Recent development on the electrochemical detection of selected pesticides: A focused review. *Sensors*, MDPI, v. 20, n. 8, p. 2221, 2020.

NOVOTNY, E. Glyphosate, roundup and the failures of regulatory assessment. *Toxics*, MDPI, v. 10, n. 6, p. 321, 2022.

NOVOTNY, L.; HECHT, B. *Principles of nano-optics*. [S.l.]: Cambridge university press, 2012.

OTTO, A. Surface-enhanced raman scattering:"classical" and "chemical" origins. *Light Scattering in Solids IV: Electronics Scattering, Spin Effects, SERS, and Morphic Effects*, Springer, p. 289–418, 2005.

PAES, T. F. et al. Silício poroso: estudo de estruturas e fotoluminescência para possíveis aplicações em sensores. *São José dos Campos: Instituto Nacional de Pesquisas Espaciais*, 2016.

PAGANELLI, A.; GNAZZO, V.; ACOSTA, H.; LóPEZ, S. L.; CARRASCO, A. E. Glyphosate-based herbicides produce teratogenic effects on vertebrates by impairing retinoic acid signaling. *Chemical research in toxicology*, ACS Publications, v. 23, n. 10, p. 1586–1595, 2010.

PAN, Y. et al. Gold-nanoparticle, functionalized-porous-polymer monolith enclosed in capillary for on-column sers detection. *Analytical Methods*, Royal Society of Chemistry, v. 7, n. 4, p. 1349–1357, 2015.

PANG, S.; LABUZA, T. P.; HE, L. Development of a single aptamer-based surface enhanced raman scattering method for rapid detection of multiple pesticides. *Analyst*, Royal Society of Chemistry, v. 139, n. 8, p. 1895–1901, 2014.

PANG, S.; YANG, T.; HE, L. Review of surface enhanced raman spectroscopic (sers) detection of synthetic chemical pesticides. *TrAC Trends in Analytical Chemistry*, Elsevier, v. 85, p. 73–82, 2016.

PANIKAR, S. S. et al. Ultrasensitive sers substrate for label-free therapeutic-drug monitoring of paclitaxel and cyclophosphamide in blood serum. *Analytical chemistry*, ACS Publications, v. 91, n. 3, p. 2100–2111, 2018.

PATSIAS, J.; PAPADOPOULOU, A.; PAPADOPOULOU-MOURKIDOU, E. Automated trace level determination of glyphosate and aminomethyl phosphonic acid in water by on-line anion-exchange solid-phase extraction followed by cation-exchange liquid chromatography and post-column derivatization. *Journal of Chromatography A*, Elsevier, v. 932, n. 1-2, p. 83–90, 2001.

PEI, M.; LAI, J. Qualitative and quantitative analysis of glyphosate. *Chinese Journal Guangdong Police Science Technology*, v. 1, p. 14–15, 2004.

PEREIRA, H. A. et al. Adsorbents for glyphosate removal in contaminated waters: a review. *Environmental Chemistry Letters*, Springer, v. 19, n. 2, p. 1525–1543, 2021.

PÉREZ-JIMÉNEZ, A. I.; LYU, D.; LU, Z.; LIU, G.; REN, B. Surface-enhanced raman spectroscopy: benefits, trade-offs and future developments. *Chemical science*, Royal Society of Chemistry, v. 11, n. 18, p. 4563–4577, 2020.

PETTINGER, B. Light scattering by adsorbates at ag particles: Quantum-mechanical approach for energy transfer induced interfacial optical processes involving surface plasmons, multipoles, and electron-hole pairs. *The Journal of chemical physics*, American Institute of Physics, v. 85, n. 12, p. 7442–7451, 1986.

PHAN-QUANG, G. C. et al. Tracking airborne molecules from afar: Three-dimensional metal–organic framework-surface-enhanced raman scattering platform for stand-off and real-time atmospheric monitoring. *ACS nano*, ACS Publications, v. 13, n. 10, p. 12090–12099, 2019.

PINCHUK, A. O.; SCHATZ, G. C. Nanoparticle optical properties: Far-and near-field electrodynamic coupling in a chain of silver spherical nanoparticles. *Materials Science and Engineering: B*, Elsevier, v. 149, n. 3, p. 251–258, 2008.

PINTADO, S.; AMARO, R. R.; MAYéN, M.; MELLADO, J. M. R. Electrochemical determination of the glyphosate metabolite aminomethylphosphonic acid (ampa) in drinking waters with an electrodeposited copper electrode. *Int. J. Electrochem. Sci*, v. 7, p. 305–312, 2012.

PIRES, N. L. et al. Determination of glyphosate, ampa and glufosinate by high performance liquid chromatography with fluorescence detection in waters of the santarém plateau, brazilian amazon. *Journal of Environmental Science and Health, Part B*, Taylor & Francis, v. 55, n. 9, p. 794–802, 2020.

POLETTA, G.; LARRIERA, A.; KLEINSORGE, E.; MUDRY, M. Genotoxicity of the herbicide formulation roundup®(glyphosate) in broad-snouted caiman (caiman latirostris) evidenced by the comet assay and the micronucleus test. *Mutation Research/Genetic Toxicology and Environmental Mutagenesis*, Elsevier, v. 672, n. 2, p. 95–102, 2009.

POULSEN, M. E.; CHRISTENSEN, H. B.; HERRMANN, S. S. Proficiency test on incurred and spiked pesticide residues in cereals. *Accreditation and quality assurance*, Springer, v. 14, n. 8, p. 477–485, 2009.

PRASAD, B. B.; JAUHARI, D.; TIWARI, M. P. Doubly imprinted polymer nanofilm-modified electrochemical sensor for ultra-trace simultaneous analysis of glyphosate and glufosinate. *Biosensors and Bioelectronics*, Elsevier, v. 59, p. 81–88, 2014.

PROCHÁZKA, M. Surface-enhanced raman spectroscopy. *Biological and medical physics, biomedical engineering*, Springer, p. 1–221, 2016.

QIANGTING, Z. et al. From old digital video disk to sers strips with controllable electrochemical method. *Journal of Shanghai Normal UniversityNatural Sciences*, v. 51, n. 4, 2022.

QU, L.-L. et al. Batch fabrication of disposable screen printed sers arrays. *Lab on a Chip*, Royal Society of Chemistry, v. 12, n. 5, p. 876–881, 2012.

QUAN, J. et al. Three-dimensional agnps-graphene-agnps sandwiched hybrid nanostructures with sub-nanometer gaps for ultrasensitive surface-enhanced raman spectroscopy. *Carbon*, Elsevier, v. 147, p. 105–111, 2019.

QUINN, J. P.; PEDEN, J. M.; DICK, R. E. Carbon-phosphorus bond cleavage by gram-positive and gram-negative soil bacteria. *Applied Microbiology and Biotechnology*, Springer, v. 31, n. 3, p. 283–287, 1989.

RADU, A. et al. Hd dvd substrates for surface enhanced raman spectroscopy analysis: fabrication, theoretical predictions and practical performance. *RSC advances*, Royal Society of Chemistry, v. 6, n. 50, p. 44163–44169, 2016.

RADZIUK, D.; MOEHWALD, H. Prospects for plasmonic hot spots in single molecule sers towards the chemical imaging of live cells. *Physical Chemistry Chemical Physics*, Royal Society of Chemistry, v. 17, n. 33, p. 21072–21093, 2015.

RAMAN, C.; KRISHNAN, K. A new class of spectra due to secondary radiation. part i. Indian Association for the Cultivation of Science, 1928.

RAMAN, C. V.; KRISHNAN, K. S. A new type of secondary radiation. *Nature*, Nature Publishing Group, v. 121, n. 3048, p. 501–502, 1928.

RASMUSSEN, J. J. et al. The legacy of pesticide pollution: an overlooked factor in current risk assessments of freshwater systems. *Water Research*, Elsevier, v. 84, p. 25–32, 2015.

RENARD, D. et al. Polydopamine-stabilized aluminum nanocrystals: aqueous stability and benzo [a] pyrene detection. *Acs Nano*, ACS Publications, v. 13, n. 3, p. 3117–3124, 2019.

REYNOSO, E. C.; TORRES, E.; BETTAZZI, F.; PALCHETTI, I. Trends and perspectives in immunosensors for determination of currently-used pesticides: the case of glyphosate, organophosphates, and neonicotinoids. *Biosensors*, MDPI, v. 9, n. 1, p. 20, 2019.

RICHMOND, M. E. Glyphosate: a review of its global use, environmental impact, and potential health effects on humans and other species. *Journal of Environmental Studies and Sciences*, Springer, v. 8, n. 4, p. 416–434, 2018.

RIVAS-GARCIA, T.; ESPINOSA-CALDERÓN, A.; HERNÁNDEZ-VÁZQUEZ, B.; SCHWENTESIUS-RINDERMANN, R. Overview of environmental and health effects related to glyphosate usage. *Sustainability*, MDPI, v. 14, n. 11, p. 6868, 2022.

ROUQUEROL, J. et al. Recommendations for the characterization of porous solids (technical report). *Pure and applied chemistry*, De Gruyter, v. 66, n. 8, p. 1739–1758, 1994.

RU, E. C. L.; BLACKIE, E.; MEYER, M.; ETCHEGOIN, P. G. Surface enhanced raman scattering enhancement factors: a comprehensive study. *The Journal of Physical Chemistry C*, ACS Publications, v. 111, n. 37, p. 13794–13803, 2007.

RU, E. C. L.; ETCHEGOIN, P. G. Single-molecule surface-enhanced raman spectroscopy. *Annu. Rev. Phys. Chem*, v. 63, n. 1, p. 65–87, 2012.

RU, E. C. L.; ETCHEGOIN, P. G. Quantifying sers enhancements. *MRS bulletin*, Cambridge University Press, v. 38, n. 8, p. 631–640, 2013.

RU, E. C. L.; SCHROETER, L. C.; ETCHEGOIN, P. G. Direct measurement of resonance raman spectra and cross sections by a polarization difference technique. *Analytical chemistry*, ACS Publications, v. 84, n. 11, p. 5074–5079, 2012.

RU, E. L.; ETCHEGOIN, P. *Principles of Surface-Enhanced Raman Spectroscopy: and related plasmonic effects*. [S.l.]: Elsevier, 2008.

RUBIO, F.; VELDHUIS, L. J.; CLEGG, B. S.; FLEEKER, J. R.; HALL, J. C. Comparison of a direct elisa and an hplc method for glyphosate determinations in water. *Journal of Agricultural and Food chemistry*, ACS Publications, v. 51, n. 3, p. 691–696, 2003.

RUIZ-SUÁREZ, N. et al. The assessment of daily dietary intake reveals the existence of a different pattern of bioaccumulation of chlorinated pollutants between domestic dogs and cats. *Science of the Total Environment*, Elsevier, v. 530, p. 45–52, 2015.

SAILOR, M. Sensor applications of porous silicon. *Properties of porous silicon*, Short Run Press Ltd.: London, v. 18, p. 364–370, 1997.

SAILOR, M. J. *Porous silicon in practice: preparation, characterization and applications*. [S.l.]: John Wiley & Sons, 2012.

SAMSEL, A.; SENEFF, S. Glyphosate's suppression of cytochrome p450 enzymes and amino acid biosynthesis by the gut microbiome: pathways to modern diseases. *Entropy*, Multidisciplinary Digital Publishing Institute, v. 15, n. 4, p. 1416–1463, 2013.

SANCHíS, J. et al. Determination of glyphosate in groundwater samples using an ultrasensitive immunoassay and confirmation by on-line solid-phase extraction followed by liquid chromatography coupled to tandem mass spectrometry. *Analytical and Bioanalytical Chemistry*, Springer, v. 402, n. 7, p. 2335–2345, 2012.

SANCI, R.; VOLKAN, M. Surface-enhanced raman scattering (sers) studies on silver nanorod substrates. *Sensors and Actuators B: Chemical*, Elsevier, v. 139, n. 1, p. 150–155, 2009.

SANKARAN, R. M.; GIAPIS, K. P. Hollow cathode sustained plasma microjets: Characterization and application to diamond deposition. *Journal of Applied Physics*, American Institute of Physics, v. 92, n. 5, p. 2406–2411, 2002.

SANTANA, H. d.; ZAIA, D. A.; CORIO, P.; HABER, F. E.; LOUARN, G. Preparação e caracterização de substratos sers ativos: um estudo da adsorção do cristal violeta sobre nanopartículas de prata. *Química Nova*, SciELO Brasil, v. 29, p. 194–199, 2006.

SARFO, D. K.; IZAKE, E. L.; O'MULLANE, A. P.; AYOKO, G. A. Fabrication of nanostructured sers substrates on conductive solid platforms for environmental application. *Critical Reviews in Environmental Science and Technology*, Taylor & Francis, v. 49, n. 14, p. 1294–1329, 2019.

SARKAR, B. et al. Sorption and desorption of agro-pesticides in soils. In: *Agrochemicals Detection, Treatment and Remediation*. [S.l.]: Elsevier, 2020. p. 189–205.

SCHRÖTTER, H.; KLÖCKNER, H. Raman scattering cross sections in gases and liquids. *Raman spectroscopy of gases and liquids*, Springer, p. 123–166, 1979.

SENAPATI, S.; SRIVASTAVA, S. K.; SINGH, S. B.; KULKARNI, A. R. Sers active ag encapsulated fe@ sio2 nanorods in electromagnetic wave absorption and crystal violet detection. *Environmental research*, Elsevier, v. 135, p. 95–104, 2014.

SHARMA, H. S.; CARMICHAEL, E.; MCCALL, D. Fabrication of sers substrate for the detection of rhodamine 6g, glyphosate, melamine and salicylic acid. *Vibrational spectroscopy*, Elsevier, v. 83, p. 159–169, 2016.

SHEHATA, A. A. et al. The effect of glyphosate on potential pathogens and beneficial members of poultry microbiota in vitro. *Current microbiology*, Springer, v. 66, n. 4, p. 350–358, 2013.

SHI, G.; WANG, M.; ZHU, Y.; WANG, Y.; XU, H. A novel natural sers system for crystal violet detection based on graphene oxide wrapped ag micro-islands substrate fabricated from lotus leaf as a template. *Applied Surface Science*, Elsevier, v. 459, p. 802–811, 2018.

SIEBERT, F.; HILDEBRANDT, P. Theory of infrared absorption and raman spectroscopy. *Vibrational Spectroscopy in Life Science*, Wiley-VCH Verlag GmbH & Co. KGaA, p. 11–61, 2008.

SILVA, A. C. F. da; BERNI, L. Â. Multilayer porous silicon as visible radiation absorber. *Optical Materials*, Elsevier, v. 112, p. 110795, 2021.

SINGH, R. Celebrating the 90th anniversary of the raman effect. *Indian Journal of History of Science*, v. 53, p. 50–58, 2018.

SINHA, S. S.; JONES, S.; PRAMANIK, A.; RAY, P. C. Nanoarchitecture based sers for biomolecular fingerprinting and label-free disease markers diagnosis. *Accounts of chemical research*, ACS Publications, v. 49, n. 12, p. 2725–2735, 2016.

ŠKRABIĆ, M. et al. Near-infrared surface-enhanced raman scattering on silver-coated porous silicon photonic crystals. *Nanomaterials*, MDPI, v. 9, n. 3, p. 421, 2019.

SLAGER, R. E. et al. Rhinitis associated with pesticide use among private pesticide applicators in the agricultural health study. *Journal of Toxicology and Environmental Health, Part A*, Taylor & Francis, v. 73, n. 20, p. 1382–1393, 2010.

SMITH, E.; DENT, G. *Modern Raman spectroscopy: a practical approach*. [S.l.]: John Wiley & Sons, 2019.

SONG, H.-Y. et al. Cellular toxicity of surfactants used as herbicide additives. *Journal of Korean Medical Science*, The Korean Academy of Medical Sciences, v. 27, n. 1, p. 3–9, 2012.

SOUSA, E. M. de et al. Surface modification of aisi 316 steel by α-moo3 thin films grown using cathodic cage plasma deposition. *Physica B: Condensed Matter*, Elsevier, v. 648, p. 414410, 2023.

SOUSA, R. D. et al. Cathodic cage nitriding of samples with different dimensions. *Materials Science and Engineering: A*, Elsevier, v. 465, n. 1-2, p. 223–227, 2007.

SOUSA, R. D. et al. Ionic nitriding in cathodic cage of aisi 420 martensitic stainless steel. *Surface Engineering*, Taylor & Francis, v. 24, n. 1, p. 52–56, 2008.

SOUSA, R. R. de et al. Cathodic cage plasma deposition of tin and tio2 thin films on silicon substrates. *Journal of Vacuum Science & Technology A: Vacuum, Surfaces, and Films*, American Vacuum Society, v. 33, n. 4, p. 041502, 2015.

SOUSA, R. R. M. d. et al. Thin tin and tio 2 film deposition in glass samples by cathodic cage. *Materials Research*, SciELO Brasil, v. 18, p. 347–352, 2015.

STAROWICZ, Z.; WOJNAROWSKA-NOWAK, R.; OZGA, P.; SHEREGII, E. The tuning of the plasmon resonance of the metal nanoparticles in terms of the sers effect. *Colloid and polymer science*, Springer, v. 296, n. 6, p. 1029–1037, 2018.

STEINGRÍMSDÓTTIR, M. M.; PETERSEN, A.; FANTKE, P. A screening framework for pesticide substitution in agriculture. *Journal of Cleaner Production*, Elsevier, v. 192, p. 306–315, 2018.

STODDART, P.; WHITE, D. Optical fibre sers sensors. *Analytical and bioanalytical chemistry*, Springer, v. 394, n. 7, p. 1761–1774, 2009.

STORCK, V.; KARPOUZAS, D. G.; MARTIN-LAURENT, F. Towards a better pesticide policy for the european union. *Science of the Total Environment*, Elsevier, v. 575, p. 1027–1033, 2017.

SU, W.; LUO, Y.; DING, Y.; WU, J. Low-cost surface plasmon resonance refractive index sensor based on the metal grating in dvd-rom disc. *Sensors and Actuators A: Physical*, Elsevier, v. 330, p. 112858, 2021.

SUN, Z.; ZHAO, B.; LOMBARDI, J. R. Zno nanoparticle size-dependent excitation of surface raman signal from adsorbed molecules: Observation of a charge-transfer resonance. *Applied Physics Letters*, AIP Publishing, v. 91, n. 22, 2007.

TANG, W.; AN, Y.; ROW, K. H. Fabrication of au nanoparticles embedded holey g-c3n4 as sers substrates for sensitive and reliable detection. *Chemical Engineering Journal*, Elsevier, v. 402, p. 126194, 2020.

TANG, X. et al. Electromagnetic mechanisms or chemical mechanisms? role of interfacial charge transfer in the plasmonic metal/semiconductor heterojunction. *The Journal of Physical Chemistry Letters*, ACS Publications, v. 13, n. 33, p. 7816–7823, 2022.

THONGPRAKAISANG, S.; THIANTANAWAT, A.; RANGKADILOK, N.; SURIYO, T.; SATAYAVIVAD, J. Glyphosate induces human breast cancer cells growth via estrogen receptors. *Food and chemical toxicology*, Elsevier, v. 59, p. 129–136, 2013.

TORRETTA, V.; KATSOYIANNIS, I. A.; VIOTTI, P.; RADA, E. C. Critical review of the effects of glyphosate exposure to the environment and humans through the food supply chain. *Sustainability*, MDPI, v. 10, n. 4, p. 950, 2018.

TORUL, H.; BOYACI, İ. H.; TAMER, U. Attomole detection of glyphosate by surface-enhanced raman spectroscopy using gold nanorods. *FABAD J. Pharm. Sci*, v. 35, p. 179–184, 2010.

TSENG, S.-H.; LO, Y.-W.; CHANG, P.-C.; CHOU, S.-S.; CHANG, H.-M. Simultaneous quantification of glyphosate, glufosinate, and their major metabolites in rice and soybean sprouts by gas chromatography with pulsed flame photometric detector. *Journal of Agricultural and Food Chemistry*, ACS Publications, v. 52, n. 13, p. 4057–4063, 2004.

TSUI, M. T.; CHU, L. Aquatic toxicity of glyphosate-based formulations: comparison between different organisms and the effects of environmental factors. *Chemosphere*, Elsevier, v. 52, n. 7, p. 1189–1197, 2003.

UHLIR, A. J. Electrolytic shaping of germanium and silicon. *Bell System Technical Journal*, Wiley Online Library, v. 35, n. 2, p. 333–347, 1956.

UNAGAMI, T. Formation mechanism of porous silicon layer by anodization in hf solution. *Journal of the electrochemical society*, IOP Publishing, v. 127, n. 2, p. 476, 1980.

VALLE, A.; MELLO, F.; ALVES-BALVEDI, R.; RODRIGUES, L.; GOULART, L. Glyphosate detection: methods, needs and challenges. *Environmental chemistry letters*, Springer, v. 17, n. 1, p. 291–317, 2019.

VALLEY, N.; GREENELTCH, N.; DUYNE, R. P. V.; SCHATZ, G. C. A look at the origin and magnitude of the chemical contribution to the enhancement mechanism of surface-enhanced raman spectroscopy (sers): Theory and experiment. *The Journal of Physical Chemistry Letters*, ACS Publications, v. 4, n. 16, p. 2599–2604, 2013.

VENDAMANI, V.; BEERAM, R.; RAO, S. N.; PATHAK, A.; SOMA, V. R. Trace level detection of explosives and pesticides using robust, low-cost, free-standing silver nanoparticles decorated porous silicon. *Optics Express*, Optica Publishing Group, v. 29, n. 19, p. 30045–30061, 2021.

VIRGA, A. et al. Silver nanoparticles on porous silicon: approaching single molecule detection in resonant sers regime. *The Journal of Physical Chemistry C*, ACS Publications, v. 117, n. 39, p. 20139–20145, 2013.

VRÁBLOVÁ, M.; SMUTNÁ, K.; KOUTNÍK, I.; PROSTĚJOVSKỲ, T.; ŽEBRÁK, R. Surface plasmon resonance imaging sensor for detection of photolytically and photocatalytically degraded glyphosate. *Sensors*, MDPI, v. 22, n. 23, p. 9217, 2022.

WAIMAN, C. V.; AVENA, M. J.; GARRIDO, M.; BAND, B. F.; ZANINI, G. P. A simple and rapid spectrophotometric method to quantify the herbicide glyphosate in aqueous media. application to adsorption isotherms on soils and goethite. *Geoderma*, Elsevier, v. 170, p. 154–158, 2012.

WALI, L. A.; HASAN, K. K.; ALWAN, A. M. Rapid and highly efficient detection of ultra-low concentration of penicillin g by gold nanoparticles/porous silicon sers active substrate. *Spectrochimica Acta Part A: Molecular and Biomolecular Spectroscopy*, Elsevier, v. 206, p. 31–36, 2019.

WALLACE, J.; LINGENFELTER, D. Glyphosate (roundup): Understanding risks to human health. *PennState Extension: College of Agricultural Sciences*, p. 1–3, 2019.

WANG, C.; XU, M.; XU, T.; JIN, Y. Fabrication of ag/pdms substrate of high-density hot spots and its application in in situ detection. *Nano*, World Scientific, v. 16, n. 06, p. 2150064, 2021.

WANG, K.; SUN, D.-W.; PU, H.; WEI, Q. Two-dimensional au@ ag nanodot array for sensing dual-fungicides in fruit juices with surface-enhanced raman spectroscopy technique. *Food chemistry*, Elsevier, v. 310, p. 125923, 2020.

WANG, M. et al. Enhance fluorescence study of grating structure based on three kinds of optical disks. *Optics Communications*, Elsevier, v. 481, p. 126522, 2021.

WANG, X.; SHI, W.; SHE, G.; MU, L. Surface-enhanced raman scattering (sers) on transition metal and semiconductor nanostructures. *Physical Chemistry Chemical Physics*, Royal Society of Chemistry, v. 14, n. 17, p. 5891–5901, 2012.

WEI, W.; HUANG, Q. Rapid fabrication of silver nanoparticle-coated filter paper as sers substrate for low-abundance molecules detection. *Spectrochimica Acta Part A: Molecular and Biomolecular Spectroscopy*, Elsevier, v. 179, p. 211–215, 2017.

WEI, W.; HUANG, Q. Preparation of cellophane-based substrate and its sers performance on the detection of cv and acetamiprid. *Spectrochimica Acta Part A: Molecular and Biomolecular Spectroscopy*, Elsevier, v. 193, p. 8–13, 2018.

WEI, W. Y.; WHITE, I. M. Inkjet-printed paper-based sers dipsticks and swabs for trace chemical detection. *Analyst*, Royal Society of Chemistry, v. 138, n. 4, p. 1020–1025, 2013.

WHO. *World Health Organization et al. Glyphosate environmental health criteria no. 159*. [S.l.]: World Health Organization, 1994.

WHO. *World Health Organization et al. The WHO recommended classification of pesticides by hazard and guidelines to classification 2019*. [S.l.]: World Health Organization, 2020.

WINFIELD, T. Wj bashe (technology applications inc.) tv baker (technology applications inc.). *Methods for the Determination of Organic Compounds in Drinking Water: Supplement I*, Environmental Monitoring Systems Laboratory, Office of Research and . . . , v. 91, n. 146027, p. 63, 1990.

XIA, L. et al. Visualized method of chemical enhancement mechanism on sers and ters. *Journal of Raman Spectroscopy*, Wiley Online Library, v. 45, n. 7, p. 533–540, 2014.

XING, C. et al. Convective self-assembly of 2d nonclose-packed binary au nanoparticle arrays with tunable optical properties. *Chemistry of Materials*, ACS Publications, v. 33, n. 1, p. 310–319, 2020.

XU, D. et al. Copper nanoleaves sers substrates with high surface roughness for sensitive detection crystal violet and rhodamine 6g. *Optics & Laser Technology*, Elsevier, v. 145, p. 107502, 2022.

XU, H.; KÄLL, M. Estimating sers properties of silver-particle aggregates through generalized mie theory. In: *Surface-Enhanced Raman Scattering*. [S.l.]: Springer, 2006. p. 87–103.

XU, K. et al. Hedgehog inspired cuo nanowires/cu2o composites for broadband visible-light-driven recyclable surface enhanced raman scattering. *Advanced Optical Materials*, Wiley Online Library, v. 6, n. 7, p. 1701167, 2018.

XU, M.-L.; GAO, Y.; HAN, X. X.; ZHAO, B. Detection of pesticide residues in food using surface-enhanced raman spectroscopy: a review. *Journal of agricultural and food chemistry*, ACS Publications, v. 65, n. 32, p. 6719–6726, 2017.

XU, M.-L. et al. Role of 2–13c isotopic glyphosate adsorption on silver nanoparticles based on ninhydrin reaction: A study based on surface—enhanced raman spectroscopy. *Nanomaterials*, MDPI, v. 10, n. 12, p. 2539, 2020.

XU, M.-L. et al. Indirect glyphosate detection based on ninhydrin reaction and surface-enhanced raman scattering spectroscopy. *Spectrochimica Acta Part A: molecular and biomolecular spectroscopy*, Elsevier, v. 197, p. 78–82, 2018.

YAEL, J. A. et al. Abiotic degradation of glyphosate into aminomethylphosphonic acid in the presence of metals. *Journal of agricultural and food chemistry*, ACS Publications, v. 62, n. 40, p. 9651–9656, 2014.

YAN, B. et al. Engineered sers substrates with multiscale signal enhancement: nanoparticle cluster arrays. *Acs Nano*, ACS Publications, v. 3, n. 5, p. 1190–1202, 2009.

YAO, C. et al. Separation, identification and fast determination of organophosphate pesticide methidathion in tea leaves by thin layer chromatography–surface-enhanced raman scattering. *Analytical Methods*, Royal Society of Chemistry, v. 5, n. 20, p. 5560–5564, 2013.

YAP, F. L.; THONIYOT, P.; KRISHNAN, S.; KRISHNAMOORTHY, S. Nanoparticle cluster arrays for high-performance sers through directed self-assembly on flat substrates and on optical fibers. *Acs Nano*, ACS Publications, v. 6, n. 3, p. 2056–2070, 2012.

YILMAZ, H. et al. Gold-nanorod-based plasmonic nose for analysis of chemical mixtures. *ACS Applied Nano Materials*, ACS Publications, v. 2, n. 6, p. 3897–3905, 2019.

ZAYATS, A. V.; SMOLYANINOV, I. I.; MARADUDIN, A. A. Nano-optics of surface plasmon polaritons. *Physics reports*, Elsevier, v. 408, n. 3-4, p. 131–314, 2005.

ZEIRI, L.; RECHAV, K.; PORAT, Z.; ZEIRI, Y. Silver nanoparticles deposited on porous silicon as a surface-enhanced raman scattering (sers) active substrate. *Applied Spectroscopy*, SAGE Publications Sage UK: London, England, v. 66, n. 3, p. 294–299, 2012.

ZELENKOVA, N.; VINOKUROVA, N. Determination of glyphosate and its biodegradation products by chromatographic methods. *Journal of Analytical Chemistry*, Springer, v. 63, n. 9, p. 871–874, 2008.

ZHAN, H.; FENG, Y.; FAN, X.; CHEN, S. Recent advances in glyphosate biodegradation. *Applied microbiology and biotechnology*, Springer, v. 102, n. 12, p. 5033–5043, 2018.

ZHANG, C. et al. Degradation dynamics of glyphosate in different types of citrus orchard soils in china. *Molecules*, MDPI, v. 20, n. 1, p. 1161–1175, 2015.

ZHANG, H.; DUAN, S.; RADJENOVIC, P. M.; TIAN, Z.-Q.; LI, J.-F. Core–shell nanostructure-enhanced raman spectroscopy for surface catalysis. *Accounts of Chemical Research*, ACS Publications, v. 53, n. 4, p. 729–739, 2020.

ZHANG, K. et al. A facile surface-enhanced raman scattering (sers) detection of rhodamine 6g and crystal violet using au nanoparticle substrates. *Applied Surface Science*, Elsevier, v. 347, p. 569–573, 2015.

ZHANG, M. et al. Highly efficient photoinduced enhanced raman spectroscopy (piers) from plasmonic nanoparticles decorated 3d semiconductor arrays for ultrasensitive, portable, and recyclable detection of organic pollutants. *ACS sensors*, ACS Publications, v. 4, n. 6, p. 1670–1681, 2019.

ZHANG, X. Morphology and formation mechanisms of porous silicon. *Journal of the Electrochemical Society*, IOP Publishing, v. 151, n. 1, p. C69, 2003.

ZHAO, B. et al. Green synthesis of multi-dimensional plasmonic coupling structures: Graphene oxide gapped gold nanostars for highly intensified surface enhanced raman scattering. *Chemical Engineering Journal*, Elsevier, v. 349, p. 581–587, 2018.

ZHAO, J. et al. Methods for describing the electromagnetic properties of silver and gold nanoparticles. *Accounts of chemical research*, ACS Publications, v. 41, n. 12, p. 1710–1720, 2008.

ZHEN, M.; SONG, B.; LIU, X.; CHANDANKERE, R.; TANG, J. Biochar-mediated regulation of greenhouse gas emission and toxicity reduction in bioremediation of organophosphorus pesticide-contaminated soils. *Chinese journal of chemical engineering*, Elsevier, v. 26, n. 12, p. 2592–2600, 2018.

ZHENG, J.; PANG, S.; LABUZA, T. P.; HE, L. Semi-quantification of surface-enhanced raman scattering using a handheld raman spectrometer: a feasibility study. *Analyst*, Royal Society of Chemistry, v. 138, n. 23, p. 7075–7078, 2013.

ZHU, Y.; ZHANG, F.; TONG, C.; LIU, W. Determination of glyphosate by ion chromatography. *Journal of chromatography A*, Elsevier, v. 850, n. 1-2, p. 297–301, 1999.

ZHU, Z.; ZHU, T.; LIU, Z. Raman scattering enhancement contributed from individual gold nanoparticles and interparticle coupling. *Nanotechnology*, IOP Publishing, v. 15, n. 3, p. 357, 2004.

ZOU, S.; SCHATZ, G. C. Silver nanoparticle array structures that produce giant enhancements in electromagnetic fields. *Chemical Physics Letters*, Elsevier, v. 403, n. 1-3, p. 62–67, 2005.

ZRIMSEK, A. B.; WONG, N. L.; DUYNE, R. P. V. Single molecule surface-enhanced raman spectroscopy: a critical analysis of the bianalyte versus isotopologue proof. *The Journal of Physical Chemistry C*, ACS Publications, v. 120, n. 9, p. 5133–5142, 2016.

APPENDIX A – List of Scientific Results

LIST OF PUBLICATIONS

- L.S. Murcia-Correa, O.C. Usuriaga, Lucia Vieira, L. Raniero, *SERS-active substrates using DVD-R coated in silver thin films: A preliminary study for detection of commercial glyphosate*, **Spectrochimica Acta Part A: Molecular and Biomolecular Spectroscopy, Volume 302, 2023, 123017**, ISSN 1386-1425.
  DOI: 10.1016/j.saa.2023.123017
  Link: <https://www.sciencedirect.com/science/article/pii/S1386142523007023>

LIST OF ACADEMIC EVENTS

- IV CONGRESSO DIGITAL DE NANOBIOTECNOLOGIA E BIOENGENHARIA
  July 2023
  Embrapa Genetic Resources and Biotechnology, Brasil.
  E-poster presentation: "Overview of porous silicon with nanoparticles coating as a solid SERS for detecting low concentrations of crystal violet".

- III CONGRESSO DIGITAL DE NANOBIOTECNOLOGIA E BIOENGENHARIA
  June 2022
  Embrapa Genetic Resources and Biotechnology, Brasil.
  E-poster presentation: "SERS-Active substrates using Silver Thin Films-coated in DVD-R: an introductory for detection of environmental pollution".

- IX SIMFAST
  May 2022
  Universidade do Vale do Paraíba (Univap) - São Paulo, Brasil.
  Oral Presentation: "Preliminary study of solid SERS-Active Substrates using Silver Thin Films-Coated Polymer Materials for detection of environmental pollution".

- VIII SBGEA & VIII SIMFAST
  March 2021
  Universidade do Vale do Paraíba (Univap) - São Paulo, Brasil.
  Assistant.

- XIII Encontro de Física do ITA-EFITA
  July 2019
  Instituto Tecnológico de Aeronáutica (ITA) - São Paulo, Brasil.
  Assistant.